A MOTIONLESS GAS MICROPUMP USING THERMAL TRANSPIRATION IN BULK NANOPOROUS MATERIALS

by

Naveen Kumar Gupta

A dissertation submitted in partial fulfillment
of the requirements for the degree of
Doctor of Philosophy
(Mechanical Engineering)
in The University of Michigan
2010

Doctoral Committee:

Professor Yogesh B. Gianchandani, Chair
Professor Khalil Najafi
Associate Professor Katsuo Kurabayashi
Assistant Professor Anastasios John Hart

To my parents and my brother,
who have always supported me and
encouraged me in all my efforts

ACKNOWLEDGEMENTS

First of all, I would like to thank Professor Gianchandani for giving me such a wonderful opportunity to work in his group on some of the most exciting projects. During the period of past four and a half years, while working with him, I have learnt how the toughest problems can be broken down into relatively easy and achievable sub-tasks with the help of methodical thinking and focused approach. I enjoy interacting with him, because, apart from getting things done right, he makes sure that I understand the thought process that goes behind it. I still remember his first words to me when I joined the group, "PhD is a long and tough journey, you will have several ups and downs, getting demotivated is not an option; you need to have persistence to work your way through the toughest times in PhD". These words have motivated me and propelled my efforts for the past four and half years.

I would also like to thank my committee members, Prof. Najafi, Prof. Kurabayashi, and Prof. Hart, for devoting their precious time discussing my project and providing me with their invaluable feedbacks. Their feedbacks have helped me add new dimensions to the project. Without their support it would have been impossible for me to achieve the desired performance targets on time.

I would like to thank all the present and past members of Gianchandani group – Tao, Mark, Amar, Jong, Scott Green, Scott Wright, Allan, Christine, Weibin, Angelo,

Bhaskar, Karthik, Fatih, Heidi, and Erwin. They are very friendly and talking to them makes me feel at home. In particular, I would like to thank Tao and Mark for mentoring me during the initial phases of my PhD. They had been really patient in discussing my problems and helping me resolve those. Tao continues to mentor me even now with several academic and non-academic issues.

Apart from the Gianchandani group, I have found a rich pool of very good friends in the form of WIMS group – Hanseup, Erkan, Tzeno, Razi, Seow Yuen, Angelique, Tushar, Meng-Ping, Gayatri, Niloufar, Andrew, Sang-Hyun, Sang Woo, Ali, Jae Yoong, Gustavo, Amir, Jeffrey, Sister Mary, Chun Lee, Shahrzad, Ruba, Jay, Hirotaka Sato, Rebecca, Neil, Sang Won, Daniel. We are like a big family and there is always somebody to help no matter what time of the day it is. I would also like to acknowledge the soothing and stress relieving (past midnight) discussion session with Tao, Vikram, Vikrant, Siddharth, Razi, Allan, Christine, Seow Yuen, Zeeshan, Kapil and many other late night workers.

I would like to thank all the WIMS and SSEL staff members for their support. I would like to thank Trasa for being patient and help me with several day-to-day stuff. Thank you to Deb for making sure that all the formalities related to my appointment were completed on time. Thanks to Fran and Laura for placing the purchase orders promptly.

I would like to thank the machinists Kent, John and Steve, who have helped me in getting my parts machined on time. Without their cooperation and suggestions, it would not have been possible for me to get my devices working. They were kind and patient enough to suggest improvements on my designs so that the machining time and the machining complexity were as low as possible. Kent and John have been really helpful

in getting the most complicated parts machined on time. Where as, Steve was patient enough to teach me machining using computer numeric controlled (CNC) machines, which allowed me to do simple machining jobs myself. The glass blower, Harold, helped me with cutting/machining ceramics into desired shapes. His vast experience with ceramics helped me in getting the ceramics machined in no time.

Not to mention, I am thankful to my current and previous roommates: Ashwini, Anurag, Shantanu, Jayesh, Razaik, Utsav, who were loving and caring enough that I never felt that I am away from my home. I really enjoy their company. Just a minute into talking to them, I forget all my stresses. Further, I would like to express my special thanks to one of my best friends Trushal and to one of my roommates Ashwini, who have understood me and supported me for the past four and a half years. I have learnt a lot from them as a person. I appreciate their extraordinary ability to maintain their calm even at the most difficult moments.

Finally, I would like to thank my parents Shive Nath Gupta, Kusum Lata Gupta and brother Ashish for being so understanding and supportive. They have always stood by me and have had faith in my decisions. I am sorry for not being able to spend more time with them at home. Although they would like me to stay longer in India with them, they never complain about my short trips to India. I really appreciate their patience. They are the most wonderful parents. Whatever I am, I am because of the values I got from them.

TABLE OF CONTENTS

LIST OF FIGURES

LIST OF TABLES

LIST OF APPENDICES

LIST OF ABBREVIATIONS

05PC: 5 bar nanoporous ceramic

15PC: 15 bar nanoporous ceramic

9SKP: 9 Stage Knudsen Pump

μGC: Micro Gas Chromatograph

μTAS: Micro Total Analysis System

BE: Boltzmann Equation

BGK: Bhatnagar-Gross-Krook (model)

CNC: Computer Numeric Control

CPC: Controlled Pressure Chamber

DARPA: The Defense Advanced Research Project Agency

DSMC: Direct Simulations Monte Carlo

DSMC-IP: DSMC – information preserving technique

ERC: Engineering Research Center

FE: Finite Element (model)

HI-VAC: DARPA High Vacuum Program

HI-MEMS: Hybrid Insect MEMS

IC: Integrated Circuits

KP: Knudsen Pump

LOC: Lab-On-Chip

MB-DSMC: The Molecular Block Model for DSMC

MCE: Mixed Cellulose Ester

MEMS: Microelectromechanical Systems

MSKP: Multi Stage Knudsen Pump

NSF: The National Science Foundation

NSE: Navier Stokes Equation

PEI: Poly-Ether-Imide

Ph.D.: Doctor in Philosophy

PM: (nanoporous) Polymer Membrane

PVC: Poly-Vinyl-Chloride

RMS: Root Mean Square

SS: Stainless Steel

SSEL: Solid States Electronics Laboratory

SSKP: Single Stage Knudsen Pump

VYPG: VYCOR Porous Glass

WIMS: Wireless Integrated Microsystems

ZEO: Naturally occurring zeolite, clinoptilolite.

LIST OF SYMBOLS

β: Contact angle of water with tygon tubing

δ_{avg} : Rarefaction parameter

ε: Tolerance limit on the error e_{RMS}

ε_1: Tolerance limit on the error e_{PHss}

ε_2: Tolerance limit on the error e_{PHin}

ε_3: Tolerance limit on the error e_{PHmx}

ζ: Velocity distribution function of the gas molecules

κ: Rate of parasitic heating of the bottom facet of the ceramic

λ: Mean free path of the gas molecules

μ: Viscosity of gas

ρ: Density of gas

σ: Surface tension of water

τ_a: Thermal time constant of the gas in hot chamber

τ_{htr}: Thermal time constant of the heater

Δt: Time step

ΔP: ($=P_H-P_C$) Pressure differential across the transpiration element

ΔP_{int}: Pressure required to push a water plug in a tygon tube

ΔT: ($=T_H-T_C$) Experimentally measured temperature bias across the transpiration element

a: Hydraulic radius of the nanochannels used for thermal transpiration

a_R: Height of a rectangular channel

b_R: Width of a rectangular channel

d (=2a): Hydraulic diameter of the nanochannel

d_L: Leak aperture diameter present per unit cm^2 area of a nanoporous disc

e_{PHin}: RMS error between the fitted and the experimental pressure profiles immediately after the heater is turned on or off

e_{PHmx}: Difference between the maximum pressure values for the fitted and the experimental pressure profiles

e_{PHss}: Difference between the steady state values of the fitted and the experimental pressure profiles

e_{RMS}: RMS error between the fitted and the experimental pressure profiles

f: Fraction of experimentally measured temperature gradient that actually appears across the nanoporous ceramic

f_{air}: Ratio of the thermal time constant for air τ_a to the thermal time constant of the heater τ_{htr}

f_N: Lumped parameter that accounts for the effect of various non-idealities on the performance of a Knudsen pump

f_p: Percent porosity of a bulk nanoporous material

f_r: Measure of molecular reflectivity of the surface of a narrow channel

f_v: Velocity density function

k_1: Empirically determined factor; k_1=1 if Kn>>1, else 2<k_1<3

k_B: Boltzmann constant

l: Length of the nanochannels; or thickness of the nanoporous ceramic

m: Mass of a gas molecule

n: Number of moles of the gas

r: Radius of tygon tubing with water plugs

t: Time

$\bar{u}$: Mean velocity of the gas molecules

$\bar{\upsilon}$: Velocity vector

x: Direction along the length of the nanochannel; or direction along the thickness of the transpiration element

$\bar{x}$: Position vector along the x-direction

$\bar{y}$: Position vector along the y-direction

D: Collision diameter of gas molecule

D_L: Diameter of the leak aperture present in a bulk nanoporous material used for thermal transpiration

D_{TE}: Diameter of the transpiration element

D_{NP} (=2a): Hydraulic diameter of the nanochannels

$\bar{F}$: Imposed body forces on the gas molecules

G: Coefficient of slipping

K_H: Hydraulic conductance

Kn: Knudsen number

M: Molecular mass of gas

$\dot{M}_{avg-C}$: Thermal transpiration driven mass flow rate in a circular channel

$\dot{M}_{avg-R}$: Thermal transpiration driven mass flow rate in a rectangular channel

$\dot{M}_{TT}$: Thermal transpiration driven mass flow rate

N: Number density of gas molecules

$N_{POS}(t)$: Number of moles of gas molecules leaked out of the hot chamber during the time interval t-Δt to t

$N_{TT}(t)$: Number of moles of gas molecules pumped into the hot chamber due to thermal transpiration during the time interval t-Δt to t

P: Pressure of the gas

P_{amb}: Ambient pressure

P_{avg} (=0.5(P_H+P_C)): Average pressure across the transpiration element

P_C: Pressure in the cold chamber

$P_{Ce}(t)$: Experimentally measured pressure in the cold chamber at time t

$P_{Cm}(t)$: Modeled pressure in the cold chamber of the Knudsen pump at time t

P_H: Pressure in the hot chamber

$P_{He}(t)$: Experimentally measured pressure in the hot chamber at time t

P_{Hm}(t): Modeled pressure in the hot chamber at time t

P_{mxE}: Experimentally measured maximum pressure head generated by a single stage Knudsen pump

P_{mxM}: Modeled maximum pressure head that a single stage Knudsen pump can generate

for a given set of structural parameters a, f_P, and D_L

Q_C: Gas outflux from the cold chamber to the hot chamber

Q_{eff}: Effective gas flow in/out of the cold chamber

Q_H: Gas outflux from hot chamber to the cold chamber

Q_{iso}: Isothermal pressure driven gas flow across a transpiration element

Q_{mxE}: Extrapolated gas flow rate generated by a single stage Knudsen pump against zero pressure head based on the experimentally measured load-flow characteristics of the pump

Q_{mxM}: Modeled maximum gas flow rate generated by a single stage Knudsen pump against zero pressure head for a given set of structural parameters a, f_P, and D_L

Q_P: Pressure gas flow coefficients

Q_{POS}: (volumetric) Poiseuille flow

Q_{PR}: Nonisothermal pressure driven gas flow across the transpiration element. Nonisothermal means the membrane has a nonzero temperature gradient across its thickness

Q_T: Temperature gas flow coefficients

Q_{TT}: Thermal transpiration driven volumetric gas flow

R: Universal gas constant

R_g: Specific gas constant

T: Temperature of the gas molecules

T_{amb}: Ambient temperature

T_{avg} (=0.5(T_H+T_C)): Average temperature across the transpiration element

T_C: Temperature of the gas molecules enclosed in the cold chamber

T_{Ccrr}: Corrected temperature at the cold end of the transpiration element

$T_{Ce}(t)$: Experimentally measured temperature at the cold side of the ceramic at time t

$T_{Cm}(t)$: Modeled temperature at the cold facet of the ceramic at time t

T_{fin} : Steady state temperature of the heater measured experimentally

T_H: Temperature of the gas molecules enclosed in the hot chamber

$T_{Ha}(t)$: Modeled temperature of the air enclosed in the hot chamber at time t

T_{Hcrr}: Corrected temperature at the hot end of the transpiration element

$T_{He}(t)$: Experimentally measured temperature on the hot side of the ceramic at time t

$T_{Hm}(t)$: Modeled temperature at the hot facet of the ceramic at time t

T_{in}: Initial temperature of the heater measured experimentally

V_C: Volume of the cold chamber

V_{crr}: Corrected volume for the hot chamber

ABSTRACT

Thermal transpiration-driven Knudsen pumps have the ability to pump gas molecules without the use of any moving parts. This promises high structural reliability and low frictional losses. However, the dearth of suitable transpiration materials with appropriate properties has limited their performance, especially for atmospheric pressure operation. This thesis describes the use of bulk nanoporous materials for thermal transpiration-driven gas pumping at atmospheric pressure.

A naturally-occurring zeolite, clinoptilolite, is used to demonstrate the feasibility of thermal transpiration-driven Knudsen pumps using bulk nanoporous ceramics. For an input power of 5.35W, the initial prototype has a temperature bias of 38K across the thickness of the zeolite disc. This results in a gas flow of ≈0.12sccm with a nominal pressure load of ≈50Pa at the output, or a maximum pressure head of ≈1kPa. Transient pressure response at the sealed outlet of a Knudsen pump is analyzed using a fitted model, which allows us to quantify various non-idealities.

Several other synthetic nanoporous ceramics are also evaluated for their thermal transpiration-driven gas flow characteristics. A clay-based ceramic 15PC is identified as suitable for multistage Knudsen pumps that may accommodate higher pressure heads. While operating at 55K above room temperature, a 9-stage Knudsen pump is demonstrated to generate a maximum pressure head ≈12kPa, or a gas flow of ≈3.8μL/min. against a pressure head of 160Pa. The pump has a footprint of ≈8x8mm^2/stage. To date, a multistage Knudsen pump has operated continuously for

more than 7000 hours without any deterioration in its performance.

Higher gas flow generation capabilities are demonstrated using thermal transpiration through nanoporous cellulose ester polymer membranes. For an input power of 1.4W, a single stage Knudsen pump with 11.5mm diameter and 105μm thick polymer membrane has a temperature bias of 30K across the membrane, which provides 0.4sccm flow against a 330Pa pressure head. Experiments suggest that the polymer Knudsen pump results in a thermal transpiration-driven gas flow of ≈1 sccm in absence of any external load. It has a final packaged volume of 14x14x4.5mm^3. To date, a polymer pump has operated continuously for more than 600 hours without deterioration.

CHAPTER 1

INTRODUCTION

1.1 Motivation

Gas micropumps are required in a wide range of sensing and analysis related microsystems, such as electronic noses, mass spectrometers, gas chromatographs, [Nag98, Ter79, Wis04, Zel04] etc. Gas pumps are also useful for pneumatic actuation of microvalves or for pneumatic movement of fluid samples within various micro-total-analysis (μTAS) and lab-on-chip (LOC) systems [Abq07, Mar99, Tsa07, Wu08, Wan05, Lea03, Cho09, Wan06].

In particular, miniaturized on-chip gas pumps are required in autonomous handheld microsystems for collecting and maneuvering samples within the microsystem [Kim08, Wan05, Ung00]. One such microsystem, micro gas chromatograph (μGC), is under development at The Center of Wireless Integrated Microsystems (WIMS) of The University of Michigan [Kim06]. The μGC has two modes of operations – *gas sampling* and *gas analysis*; both of these modes have different pumping requirements that should be met using a single micropump. While operating in the gas-sampling mode, the μGC requires the gas to be pumped into a pre-concentrator at ≈25 sccm with a differential pressure of ≈ 20 kPa. While operating in the gas analysis mode, the gas molecules are to be pushed across micro columns at the rate of ≈2 sccm with a differential pressure of

about 50 kPa.

The gas pumping mechanisms based on actuation techniques, such as piezoelectric, electrostatic, peristaltic, etc., can be useful for some of the applications discussed above [Yun06, Las04, Ngu02, Ive08, Smi90]. These pumps can generate gas flow rates on the order of 10 sccm, with an input power of ≈100 mW. In addition, microfabrication techniques allow them to have small footprint (≈4 cm^2). Although these pumping mechanisms are promising, they continue to evolve in terms of requirement for drive voltages, reliability, fabrication complexity, cost etc. Most of these pumps require undesirably high operating voltages (100-400 V). Further, the cost, reliability and yield of these pumps are adversely affected by their complex fabrication processes.

In effect, the lack of available micropumps with the necessary combination of cost and performance has inhibited extensive use of micropumps [Las04]. Most of the existing microsystems use miniaturized versions of commercially available macro scale gas pumps. Unfortunately, most of these pumps are either disproportionately large or they do not meet the optimal pumping speed required by the system. A miniaturized and reliable

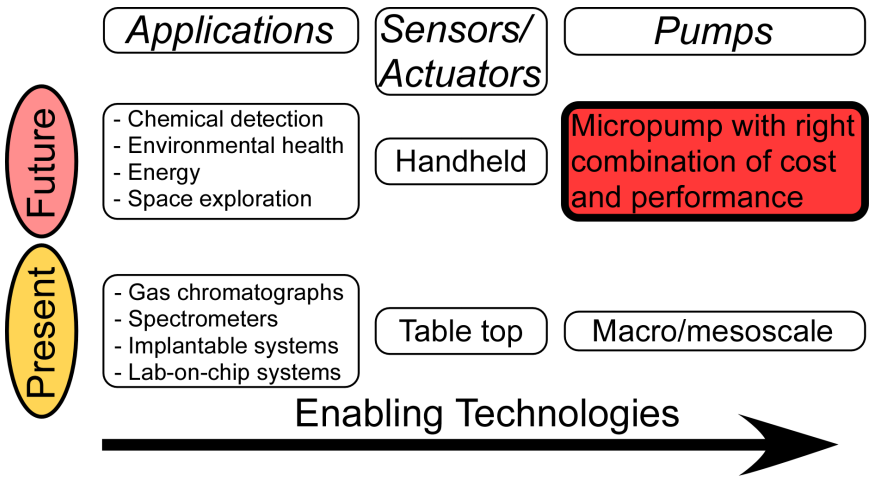

Fig. 1.1: Success of various handheld gas sensing and analysis microsystems under development today depends largely on the availability of gas micropumps with necessary combination of performance and cost.

gas micropump that can efficiently meet the gas pumping requirements of these microsystems remains an important research goal (Fig. 1.1).

The piezoelectrically driven pumps by *thinXXS Microtechnologies AG*, the electrostatically driven dual diaphragm pump by Honeywell, and the peristaltic pumping array by Kim *et al.* at The University of Michigan are some of the promising micropumps that satisfy some of the pumping requirements of microsystems [thinXXS08, Cab01, Kim06]. These are described below:

The dual diaphragm pump reported by Cabuz *et al.* at Honeywell Inc. uses two membranes, with offset perforations, driven electrostatically to pump gas from one side of the membranes to the other (Fig. 1.2). It has high gas pumping capacity (≈30 sccm), but it can generate a maximum differential of only 2 kPa for an input power of 8 mW. The architecture of the pump limits its capabilities for generating higher pressures. This mechanism has a total packaged volume of 15x15x1 mm^3. The pumping pressure requirements can be solved by connecting multiple pumps in series, but that increases the total power requirement and the size of the final device drastically. Further, the utility of

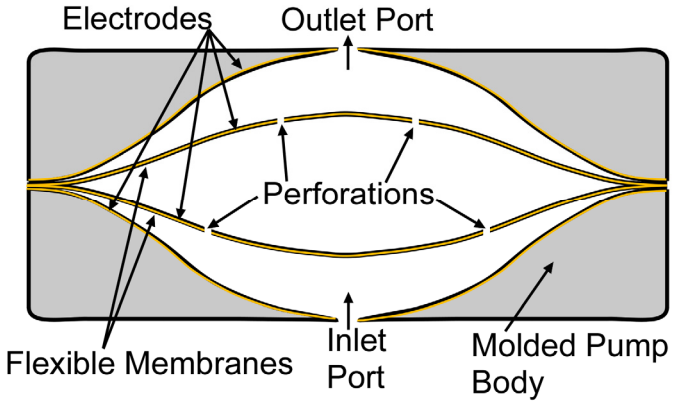

Fig. 1.2: A dual diaphragm pump, by Honeywell Inc., with two perforated membranes driven electrostatically to pump gas from top to bottom or vice-versa. The sequence of motion of the membranes determines the direction of the pumping [Cab01].

the pump is limited by the fatigue life of the two diaphragms. These diaphragms make physical contact with each other, which can potentially lead to stiction problems.

The *thinXXS* pump (model MDP1304), uses a piezoelectrically driven diaphragm to pump the gas. It can generate relatively high gas flow rates (≈22 sccm) with a maximum differential pressure of 10 kPa (Fig. 1.3) [thinXXS08]. Although the pumping pressure specifications for the μGC can be met by connecting more than one *thinXXS* pump in series, the total power consumption and the final size will become undesirably high. The power consumption of a single *thinXXS* pump, diameter 23 mm and thickness 3 mm, is ≈230 mW.

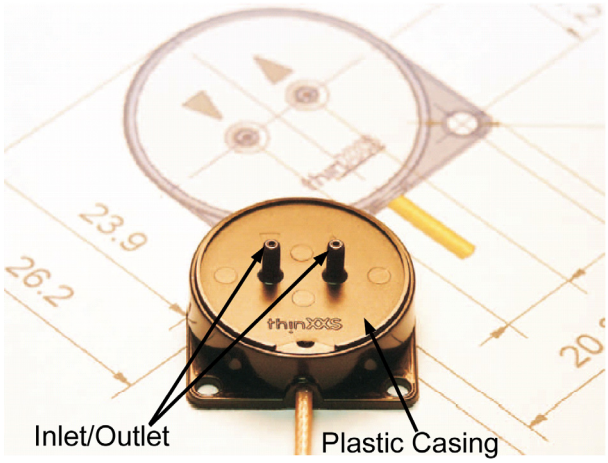

Fig. 1.3: A piezo-driven micropump by *thinXXS Microtechnologies AG*. This is a piezoactuated micro diaphragm pump with passive check valves. The pump is made of injection molded plastic and is light weight [thinXXS08].

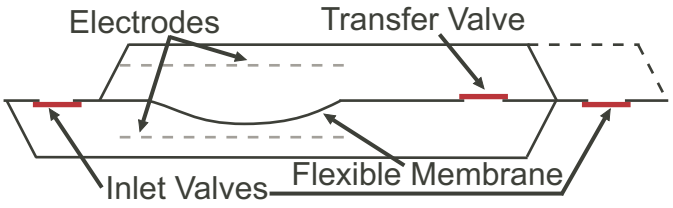

Fig. 1.4: An electrostatically driven, peristaltic array based gas pump, which uses a series of control valves to regulate the flow rate and pumping pressures for different cases. This is lithographically fabricated micropump and it is easy to be multistaged [Kim06].

Based on the various gas micropumping options available, the peristaltic pumping array proposed by Kim at The University of Michigan has emerged as a promising candidate for some microsystems application [Kim06, Kim07]. It uses a peristaltic array which includes a series of polymer membranes driven electrostatically by a dual electrode configuration and a series of microvalves that are optimized to generate the desired gas flow rates at specified pumping pressures (Fig. 1.4). For an input power of 57 mW and operating voltage 100 V, the pump results in a best case flow rates of about 4 sccm at differential pressures upto 12.8 kPa. It has a footprint of about 25.1x19.1 mm^2. Although designs based on the peristaltic arrays are extremely energy efficient, these continue to evolve with respect to drive voltage requirements, reliability and complexity.

The micropumps described above and most of the gas micropumps reported in literature are the miniaturized derivatives of their macroscale counterparts, which typically have several moving parts. With miniaturization, the surface area to volume ratio of these moving parts increases, resulting in increased frictional losses, which may adversely affect their performance and life expectancy.

Challenges that are inherent to miniaturized moving parts in a micropump motivate a consideration for micropumps based on thermal molecular pumping, such pumps can generate gas flows without the need of any moving parts. Thermal molecular pumping can potentially overcome some of these challenges because it does not require any moving parts. Unlike conventional micropumps, the thermal molecular pumps are driven by interaction of the gas molecules with the surface of the substrate [Hob00]. These pumps have the advantage of better effectiveness with miniaturization.

1.2 Thermal Molecular Pumps

1.2.1 Gas Flow Regimes

While analyzing various microsystems involving gas flow through miniaturized features, various types of gas flow regimes may need to be considered because the gas flow may not always follow continuum physics. One of the most commonly used parameters to characterize the gas flow regimes is the Knudsen number (*Kn*). The Knudsen number is defined as the ratio of the mean free path (i.e., the average distance travelled between two successive collisions) of gas molecules (λ) to the hydraulic diameter d of the channel (i.e., diameter of equivalent circular ducts):

$$Kn = \frac{\lambda}{d} \tag{1.1}$$

Knudsen number is representative of the flow regime of the gas molecules. In general, there are four different types of gas flow regimes – free molecular, transitional, slip and viscous (Fig. 1.5) [Kar05].

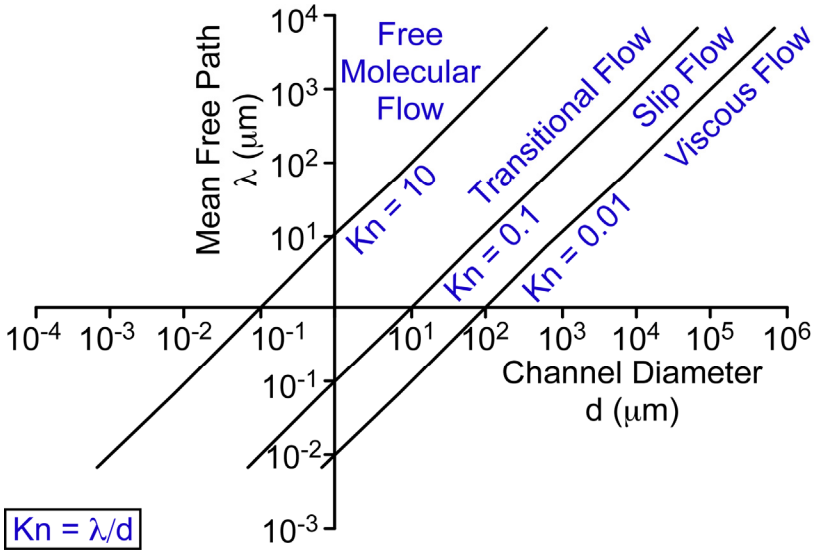

Fig. 1.5: The plot shows the ranges of Knudsen numbers for different gas flow regimes. It suggests that the rarefied gas flow can be generated either by reducing the characteristic length of a systems or by increasing the channel diameter [Kar05].

Viscous flow (Kn<0.01) corresponds to the gas flow regime for which all the continuum laws hold well. The Navier-Stokes equation (NSE) can be used for the analysis of viscous flow.

Slip flow (0.01<Kn<0.1) obeys all the laws of continuum physics and the NSE can be used for the analysis of slip flow. However, the flow velocity and the temperature of gas need to be corrected for discontinuity in their respective values at the channel walls.

Transitional flow (0.1<Kn<10) is the flow regime for which the equation based on the continuum physics, such as the NSE, cannot be used; however, the intermolecular collisions still dominate over the collisions of gas molecules with the surrounding walls.

Free molecular flow (Kn>10) regime is the condition when the mutual interaction amongst the molecules is negligible and the number of collisions of molecules with the sidewalls is much more than the intermolecular collisions.

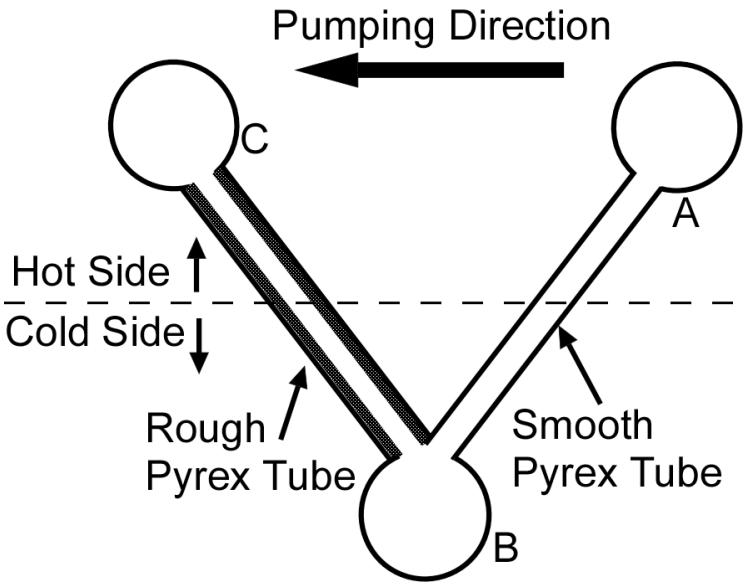

Fig. 1.6: An accommodation pump that uses the difference in physics of interaction of the gas molecules with the smooth and with the roughened pyrex walls. For chambers A and B connected with smooth pyrex tubes and chambers B and C through rough pyrex tubes – if chamber B is held at lower temperature than A and C, the effective gas flow is from chamber A to chamber C [Hob00].

Knudsen pump operation generally requires $Kn > 1$, that is the gas flow is in free molecular or transitional gas flow regime. Under these operating conditions, collisions between the molecules and channel wall are much more frequent than the intermolecular collisions. Hence, surface forces dominate for cases with $Kn > 1$.

1.2.2 Thermal Molecular Pumps

Thermal molecular pumps have no moving parts and, as the name suggests, they use thermal energy to regulate the molecular movement of the gas molecules [Hob00]. There are three types of thermal molecular pumps: accommodation pump [Hob70], thermomolecular pump [Tra74] and Knudsen pump [Knu09]. All these pumps share the advantage of no moving parts, which acts in favor of their structural reliability. They do not need any operating fluid, which makes them a promising option for pumping

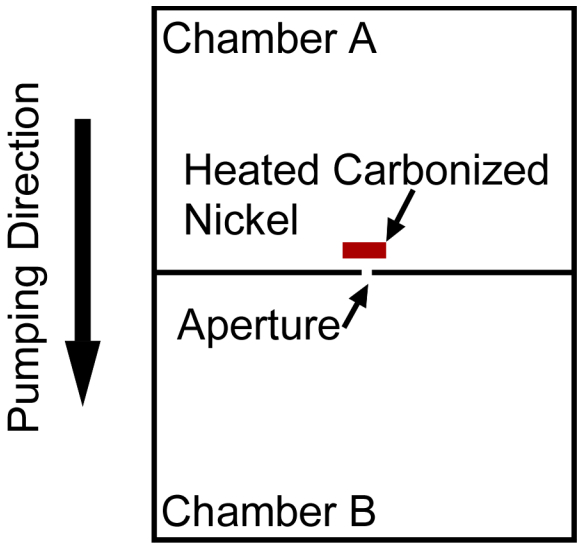

Fig. 1.7: A thermomolecular pump exploits the anisotropy in the molecular fluxes resulting from violation of the cosine reflection law. For two chambers A and B separated with a small aperture, if a reflector is located close to the aperture in chamber A and is at higher temperature, the cold gas molecules from chamber A hitting the reflector tend to bounce back closer to the normal. This results in an effective flow from chamber A to B.

applications in hostile environments, such as space exploration.

The accommodation pump exploits the difference in the scattering of gas molecules at different types of boundary surfaces to generate the pumping action [Hob70]. Figure 1.6 shows three chambers (A, B, and C) connected in series via. tubes. Chambers A and B are connected through a smooth pyrex tube and chambers B and C are connected through a roughened pyrex tube. Hobson, in his experiments, demonstrated that if A and C are maintained at room temperature and B is held at liquid nitrogen temperature (that is, temperature lower than that of A and C), an effective movement of gas molecules from A to C occurs. The difference in the gas-wall collision dynamics of the gas molecules moving through the smooth pyrex tube and through the roughened pyrex tube results in this pumping effect from chamber A to C. At equilibrium the ratio of the pressure in chamber A to the pressure in chamber B, P_A/P_B, is expected to be lower than the ratio of the pressure in chamber C to the pressure in chamber B, P_C/P_B.

Thermomolecular pumps, unlike accommodation pumps, exploit the anisotropy in the molecular fluxes resulting from violation of the cosine reflection law [Tra74]. The gas molecules incident on certain kind of surfaces, maintained at different temperature than the gas molecules themselves, tend to violate the laws of reflection. For example, a gas molecule reflected from a relatively hot surface of carbonized nickel has a greater probability of being closer to the normal, that is, the angle of reflection is less than the angle of incidence. Similarly, for a hot gas molecule being reflected from a relatively cold carbonized nickel surface, the gas molecule has a high probability to be reflected away from the normal. This anisotropy in gas reflections from a material, such as heated carbonized nickel, can be used to pump the gas molecules from the hot side to the cold

side of the device with Kn~1. Figure 1.7 shows a schematic layout of the pumping mechanism based on thermomolecular pumping. It has two chambers A and B, connected through an aperture. Chamber A has a carbonized nickel reflector placed close to the aperture such that the dimension of the reflector is on the order of distance of the reflector from the aperture. If Chambers A and B are maintained at room temperature, while the reflector is maintained at a higher temperature, the gas molecules from chamber A incident on the reflector will be reflected closer to the normal and hence they will have a greater probability of being directed into the chamber B. Thus, at equilibrium, chamber B will have higher pressure than chamber A.

The third type of thermal molecular pump, the Knudsen pump, exploits the difference in the fluxes of hot and cold gas molecules flowing across a narrow channel. It has at least two isolated chambers, at different temperatures (T_H and T_C), connected through a narrow channel (Fig. 1.8). The gas flow from one chamber to the other chamber is directly proportional to the pressure in the first chamber and inversely proportional to the square-root of its temperature. Hence, if the initial pressures in the two chambers are same, a longitudinal temperature gradient along the narrow channel results in an effective movement of gas molecules from the cold chamber to the hot chamber. At equilibrium, the hot chamber has a higher equilibrium pressure than the cold chamber. This

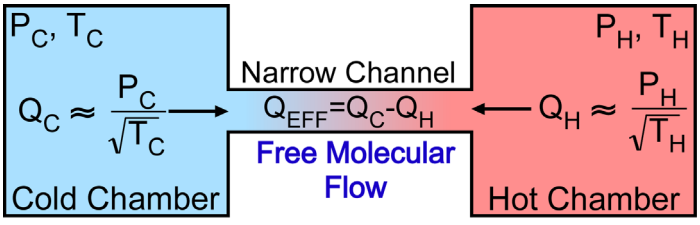

Fig. 1.8: The gas flux along a narrow channel, which can sustain only free molecular gas flow, is ideally approximated by P/√T. At equilibrium the molecular flux from the two chambers nullify each other.

phenomenon is known as *thermal transpiration*. The ratio of the equilibrium pressure in the hot chamber (P_H) to the pressure in the cold chamber (P_C) is:

$$\frac{P_H}{P_C} = \left(\frac{T_H}{T_C}\right)^{1/2} \tag{1.1}$$

A narrow channel is defined to have hydraulic diameter, d, smaller than the mean free path, λ, of the gas molecules flowing through it. In other words, gas flowing through a narrow channel is essentially in the transitional or the free molecular regime, that is $Kn>1$.

Figure 1.9 shows a schematic layout of a typical single stage Knudsen pump. It has three chambers A, B and C, such that, chamber B is maintained at higher temperature and chamber A and C are maintained at a relatively lower temperature. Chambers A and B are connected through a set of narrow channels. The gas molecules move from cold

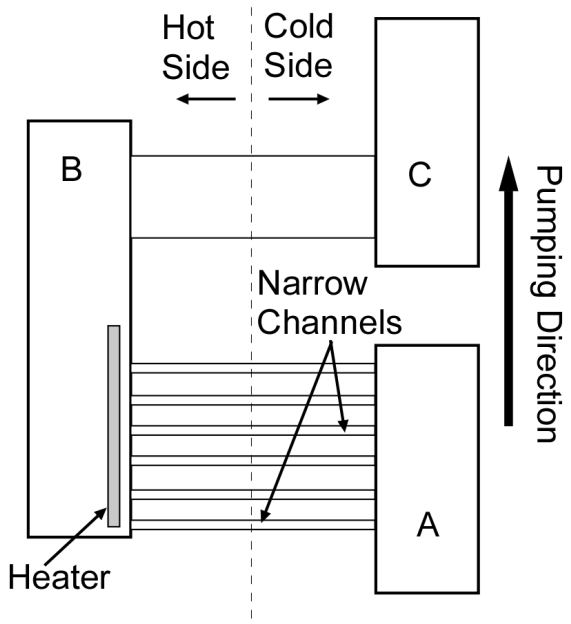

Fig. 1.9: A Knudsen pump exploits the difference in molecular fluxes of hot and cold gas molecules flowing along a narrow channel subjected to a temperature gradient. The gas molecules moving along the narrow channel have a preferential movement from the cold side of the channel to the hot side of the channel [McN05].

chamber A to hot chamber B by the virtue of thermal transpiration. This results in an equilibrium low pressure in chamber A and a relatively higher pressure in chamber B, which subsequently is connected to chamber C through a wide channel. Unlike the narrow channels, the wide channel allows continuum flow; hence, the two chambers, B and C, have same equilibrium pressure irrespective of their temperatures. Thus, the device demonstrates an effective movement of gas molecules from chamber A to chamber C, both at same temperature. This preferential movement of gas in free molecular regime from cold to hot can be potentially used for gas pumping along the narrow channels [Knu09, McN05].

In this effort, the Knudsen pump is chosen because its performance is independent of the material used and its surface conditions.

1.3 Benchmarking of Gas Micropumps

1.3.1 Present Work

The thermal transpiration driven gas pumping at atmospheric pressure require very small channels (hydraulic diameter ≈100 nm). In order to obtain gas flow rates on the order of 1 sccm under typical operating conditions, more than 10^{10} channels are needed.

This work explores the possibility of using bulk nanoporous materials for improving the gas flow generation capabilities of Knudsen pumps. Unlike lithographically fabricated surface micromachined nanochannels, bulk nanoporous materials have a high density of interconnected nanochannels (≈10^{14} channels/cm^2), which can transpire gas in parallel.

Figure 1.10 shows the gas flow rate generated by various micropumps, reported in literature, plotted against the degree of motion of the respective pumps. The '*degree of motion*', in this case, is defined as the number of dimensions in which the actuation mechanism moves. For example, the piezoelectric pumps move only in thickness direction, and the electrostatic pumps have two electrodes that attract each other; hence they have been assigned degree of motion '1'. Similarly, the pneumatic mechanisms have pressurized fluids that tend to move in all the 3 directions, hence, these mechanism have been assigned degree of motion '3'. Attractive features of pumps with fewer degrees of motion include lower structural and operational complexity, which may also result in higher reliability in the long term.

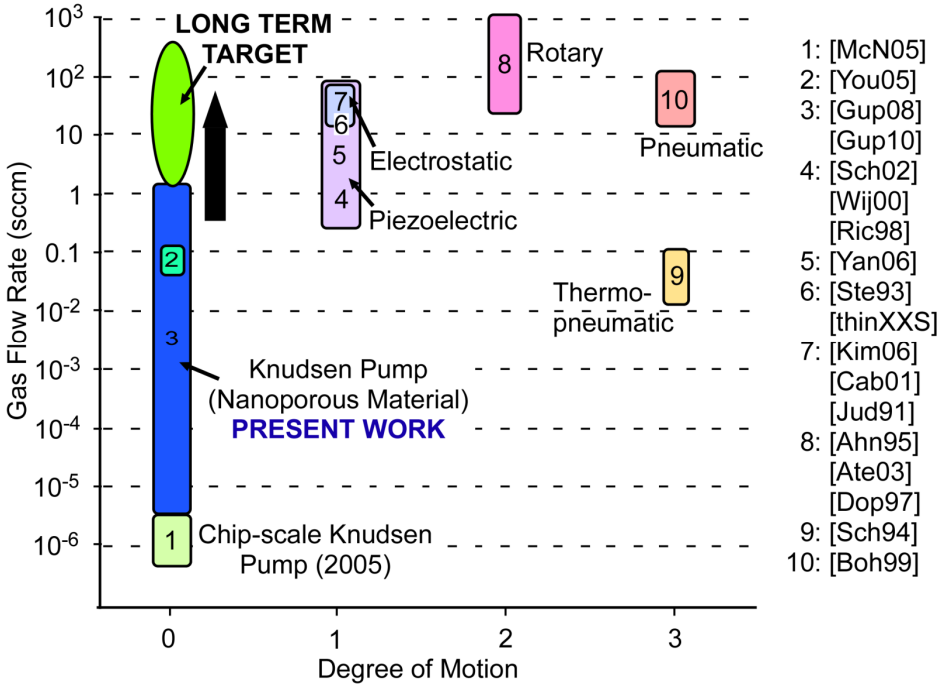

Fig. 1.10: The gas flow rate generated by various micropumps plotted against the degree of motion of each of these pumps. The degree of motion is one of the measures of the reliability of a pump. Gas pumps with higher degree of motion are expected to have lower reliability.

1.3.2 Past Work on Knudsen Pumps

First functional Knudsen pump was reported by Knudsen himself in 1909 [Knu09]. He demonstrated a compression ratio of ten across a set of ten capillaries connected in series – each containing a small constriction. Alternate joints of these capillaries were maintained at a higher temperature. The operating pressure for this set-up was significantly below atmospheric pressure to ensure that the gas flow across the constriction is in the transitional flow regime ($Kn > 0.1$). Since 1909, various researchers have contributed towards the development of the Knudsen pump; however, unavailability of sufficiently small narrow channels limited the Knudsen pump operation to sub-atmospheric pressures until recently.

With the recent advances in the microfabrication techniques and with the introduction of materials having sub-micron sized capillaries, Knudsen pump operation at atmospheric pressure had been made possible. Moreover, the development of microfabrication technology had favorable impact on the development of the Knudsen pump because with miniaturization the surface area to the volume ratio increases, which improves the effectiveness of a Knudsen pump.

The recent developments in the Knudsen pumping technology and the associated benefits have motivated various numerical studies [Mun02, Guo09, Kos08]. Researchers have used various analytical and numerical methods to establish the theoretical limits for the optimization of various performance parameters of a Knudsen pump. These performance parameters include the maximum gas flow rate and the maximum pressure generation capabilities of a Knudsen pump for a given thermal budget. These optimization studies promise a very favorable performance metrics for Knudsen pumps

under idealized conditions [Ale06, Ale05, Mun02]. However, due to various non-idealities present in the system the experimental results fail to match the theoretical estimated performance.

Amongst various experimental studies on the thermal transpiration driven flows, only very few have looked at gas pumping at atmospheric pressure. One of the leading efforts has been in Prof. Muntz's group at University of Southern California. The feasibility of cascading a single stage configuration to achieve a Knudsen compressor with desired performance was reported in [Pha95]. This was followed by an initial experimental investigation by Vargo [Var96], where he proposed the use of a membrane with several microchannel instead of using individual capillaries. Later, he introduced the feasibility of nanoporous aerogel materials, with pore size on the order of 20 nm, for Knudsen pumping at atmospheric pressure [Var01]. (Aerogel is a supercritically dried silica gel.) The hot side of the nanoporous aerogel disc was resistively heated by a lithographically patterned gold heater on a silicon chip while the cold end was maintained at a lower temperature. Their experiments suggested that the Knudsen compressor using helium as the operating medium yields better performance results than while using nitrogen. This is so because the helium gas molecules have higher Knudsen number than nitrogen gas molecules at a given temperature and pressure. For an input power of 1.7 W their compressor could generate a best case pressure drop of about 11.5 Torr with helium as the working medium. More recently, it has been reported in [You05] that a 15-stage aerogel based Knudsen pump, with an input radiant power of 20.9 mW/cm^2, can sustain a best case pressure drop of about 120 Torr (≈16 kPa); the same device could generate a best case flow rate of about 5×10^{16} molecules/sec (0.112 sccm). Researchers have also

demonstrated the use of stacked microspheres, to emulate nanopores, for the thermal transpiration driven flow [You03]. Han *et al*. studied the gas flow across aerogel discs, at low pressures (<200 Pa), through holes and through rectangular channels micromachined across the thickness of bulk aerogel [Han07]. These experimental results, when compared to the results from the optimization studies, suggested the presence of various undesired flow patterns and other non-idealities that adversely affected the performance of the pump. This highlights the fact that, if the non-idelities can be controlled, the pumping performance of Knudsen pumps can be improved significantly.

McNamara *et al.* reported the first lithographically fabricated microchip scale Knudsen pump [McN05]. Their device had the potential to be fully integrated with IC fabrication process. This chip scale pump, with small foot print of 1.5x2 mm^2, could achieve a better gas compression ratio than previously reported Knudsen pumps. This work established the feasibility of a lithographically patterned nanochannels in a chip scale fully micromachined Knudsen pump that achieved a pressure drop of about 54.7 kPa with 80 mW of input power. Use of microfabrication processes enabled this device to achieve very high thermal isolation ($\approx 10^4$ K/m), which resulted in high pressure gradients, while requiring power as low as 80 mW. The small size and high gas compression capabilities make it a suitable candidate for chip scale cavity pressure modulation. However, due to the limited number of lithographically patterned nanochannels that were fabricated, the flow rates were on the order of 10^{-6} sccm, which are inadequate for conventional applications such as gas chromatography.

This thesis describes the use of bulk nanoporous materials for thermal transpiration-driven gas pumping at atmospheric pressure. Several bulk nanoporous materials have

been studied for their thermal transpiration driven gas flow characteristics, pressure characteristics, and associated non-idealities. A fitted model has been developed to quantify various non-idealities associated with these pumps.

1.3.3 Structure of This Work

Chapter 2 presents a detailed analysis of the principle of operation of Knudsen pumps. Various analytical and semi-analytical models for thermal transpiration have been benchmarked against the direct simulations Monte Carlo (DSMC) technique – one of the most precise tools for analysis of thermal transpiration gas flows. Of particular importance, a semianalytical model is identified that is most representative of the DSMC technique and is computationally less intense.

Chapter 3 presents the design, analysis, fabrication and testing of a naturally occurring nanoporous zeolite, clinoptilolite, based single stage Knudsen pump. This chapter details a fitted model that is used to analyze the system level transient response of Knudsen pumps. The model allows us to identify and quantify various non-idealities that affect the performance of a Knudsen pump. This work demonstrates the feasibility of using a bulk nanoporous ceramic as a transpiration material in a Knudsen pump.

A multistage Knudsen pumping architecture is proposed in Chapter 4. This chapter compares thermal transpiration driven gas flow characteristics of several bulk nanoporous ceramics. The most favorable ceramic is chosen for the multistage stage Knudsen pump, which is subsequently characterized for its thermal transpiration driven gas flow characteristics.

Chapter 5 introduces the use of a thermally insulating nanoporous polymer membranes for thermal transpiration-driven Knudsen pumping. On an average, these membranes have larger pore size than the nanoporous ceramics, which is favorable for increasing the transpiration driven gas flow rates. Several types of polymer membranes have been studied and the most favorable polymer membrane has been identified for Knudsen pumps targeted at various gas sensing and analysis related applications.

Finally, Chapter 6 presents a summary of the performance of various devices fabricated in this effort. Various important observations and their role in determining the direction of further research have been highlighted.

CHAPTER 2

THEORY OF KNUDSEN PUMPS

One of the primary challenges in the design and development of a Knudsen pump is the lack of a widely accepted technique to model the phenomenon of thermal transpiration with reasonable accuracy, while keeping the computational complexity low. This chapter identifies the direct simulations Monte Carlo[1] (DSMC) technique as the most accurate modeling technique for the phenomenon of thermal transpiration. However, this approach cannot be used as a practical design tool because of its huge computational complexity. Consequently, various analytical and semi-analytical models have been benchmarked against the DSMC results with an intention to identify a thermal transpiration model that is most representative of the DSMC techniques, while being minimally computationally intensive.

2.1 The Phenomenon of Thermal Transpiration

The phenomenon of thermal transpiration refers to the ability of a narrow channel to sustain a non-zero longitudinal pressure gradient when subjected to a temperature bias. As stated in Chapter 1, in the context of this work a narrow channel refers to a channel with hydraulic diameter smaller than the mean free path of the gas molecules [Rey79,

[1] The DSMC modeling was performed in collaboration with Prof. Wenjing Ye of Georgia Institute of Technology and Hong Kong Institute of Science and Technology.

Max79]. In other words, the gas flowing through a narrow channel is essentially in transitional or free molecular regime, which corresponds to rarefied gas flow conditions. Although there is no widely accepted physical mechanism that can explain the phenomenon of thermal transpiration, there is one plausible explanation for the phenomenon, which is based on the momentum transfer between the gas molecules and the channel walls [Son00]. The asymmetry in the momentum flux from the hot and the cold sides of the narrow channel is primarily responsible for the thermal transpiration driven flow. Figure 2.1 shows a small section (δS) of the wall of a narrow channel. It has various gas molecules impinging on it from different directions. Since the mean free paths of the gas molecules are significantly larger than the hydraulic diameter of the channel, the gas molecules impinging on δS have the properties corresponding to their previous locations. Hence, the gas molecules from the hot side have a higher average velocity compared to the molecules from the cold side. This asymmetry results in an effective momentum transfer to the channel walls in the direction opposite to the temperature gradient. Consequently, the channel walls exert an effective force on the gas molecules from the cold to the hot end of the channel.

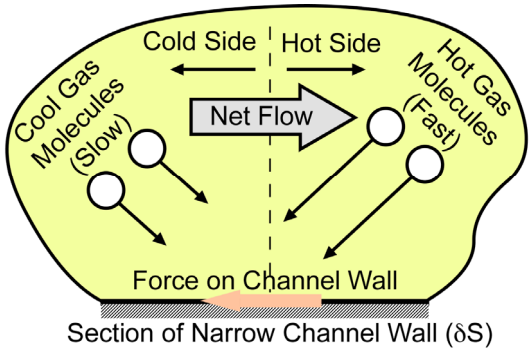

Fig. 2.1: Mechanism for the thermal transpiration driven gas flow from the cold end of the channel to the hot end. Asymmetry in the momentum being imparted to the channel walls due to the difference in velocities of gas molecules from the hot and the cold end of the channels results in an effective force on the gas molecules from the cold end of the channel to the hot end.

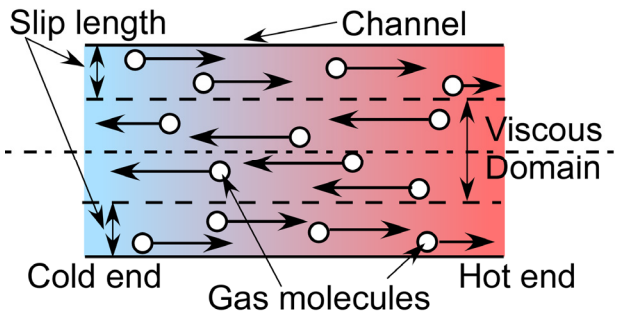

Fig. 2.2: Longitudinal temperature gradient along a channel induces the movement of gas molecules close to the wall, from the cold to the hot end, due to the thermal transpiration. This causes a backflow in the central region, which remains in viscous regime for wide channels. For channels with hydraulic diameter smaller than the mean free path of the molecules, viscous flow is greatly reduced.

Thermal transpiration in a channel can be explained as an equilibrium state attained by two opposing flow fields: thermal creep flow and Poiseuille flow (Fig. 2.2). The thermal creep flow is the movement of molecules near the walls from the cold end to the hot. The counter-flow, known as the Poiseuille flow, is induced by the pressure gradient generated by the thermal creep flow and acts to nullify the same [Loe34]. However, with the reduction in the hydraulic diameter of the channel, the central region, where the Poiseuille flow occurs, reduces in area. Hence, with the smaller number of gas molecules being pumped back through the central region, the effect of thermal transpiration becomes more noticeable. It has been shown that for Kn>1, thermal creep flow starts overcoming Poiseuille flow and, hence, may be used for gas pumping or gas compression applications [McN05, You01, Var01].

2.2 Background of Thermal Transpiration

The phenomenon of thermal transpiration was first analyzed (independently) by Reynolds and Maxwell in the year 1879. In the same year, they proposed rigorous

mathematical analyses for the phenomenon [Max79, Rey79]. Since then various researchers have proposed analytical and semi-analytical models for thermal transpiration [Col05]. Most of the models for thermal transpiration are derived from the Boltzmann equation (BE), which is a generalized expression for the gas flow. The BE will be addressed in some detail in Section 2.3, but it is worth noting that the most complicated term in the BE is the collision term. It is impossible to integrate the BE analytically because the expression for the collision term takes very complex forms. Hence, the collision term needs to be simplified for specific cases to simplify the BE and then integrate it analytically. Binary collisions (in which only two molecules collide at a time) form the central assumption for simplification of the collision term.

The first step towards analytical modeling of the phenomenon of thermal transpiration involves use of the first order simplified BE, that is, the Navier-Stokes Equation (NSE) [Kar05]. These initial first order simplified models, along with the first order corrected boundary conditions, are applicable to the near continuum rarefied gas flow analysis [Ark01]. These models have allowed researchers to investigate rarefied gas flows through various cross-sections, such as circular [Ken38], annular [Ebe65], and rectangular [Ebe65; Mor98]; however they deviate significantly from the experimental results for $Kn > 0.1$ [Sre69, Pei96].

Since the first order simplified model for the thermal transpiration has limited applicability to gas flow with $Kn > 0.1$, higher order approximations and approaches based on molecular gas dynamics have been proposed to model the phenomenon of thermal transpiration [Cha52, Bes99, Dei64, Col04, Ark01, Mau03]. Beskok *et al.* (1999) proposed a higher order approximation for boundary conditions that could fit

better with the first order approximated form of the BE, that is the NSE [Bes99]. Xue *et al.* (2000) proposed a model that could match DSMC [Xue00], one of the most reliable techniques to study rarefied gas flows, upto $Kn \approx 3$. This was followed by a more mathematically stable model by Jie *et al.* in 2000 [Jie00]. Other efforts that have looked at developing higher order analytical models for the analysis of thermal transpiration have been presented in [Eli01, Kar05].

Unlike analytical models, approximate methods based on the numerical solution of the BE yield relatively accurate results [Sha98]. For these (approximate) methods to be suitable for any Knudsen number, simplifications to the collision integral should retain its fundamental properties. The fundamental properties are a set of equations that need to be satisfied to realize a physically meaningful solution [Sha98]. These fundamental properties include conservation of particles, momentum, and energy in each collision [Lif81, Cer75, Fer72]. The simplified equation is then integrated exactly, which results in the model kinetic equations that are applicable for all values of the Knudsen number. Two main model equations that have been discussed in literature are the BGK model [Bha54] and the S-model [Sha74]. The BGK model assumes collison frequency to be independent of the molecular velocity. The collision frequency can be chosen by various methods as described in [Sha98]. The BGK model is applicable only to the isothermal gas flows. Based on the method used to choose the collision frequency, the analytical expression obtained for either viscosity or thermal conductivity (but not both) agrees with the experimentally measured values [Sha98]. Moreover, the BGK model gives a wrong estimate for the Prandtl number. Subsequently, Shakov proposed S-model, which is a modification of the BGK model giving the correct Prandtl number. Like the BGK model,

the S-model is also applicable to the isothermal gas flows. However, the S-model has also been identified to be ideal for linear non-isothermal gas flows [Sha98, Sha97]. Literature provides extensive results on the thermal creep flow for the BGK model and for the S-model; it suggests that S-model is a more appropriate model for the thermal transpiration flows [Sha98]. However, for the non-linear, non-isothermal gas flow, the fundamental properties of collisions can neither be proved nor disproved when using S-model.

2.3 Modeling of Thermal Transpiration

This section describes some of the modeling techniques used for this work. These models take forms ranging from a simple mathematical correlation, to a complex algorithm for tracking individual particles in the system.

An approach based on molecular dynamics is appealing because under the rarefied gas flow conditions some parameters, which are independent otherwise, show cross coupling. For example, under the rarefied gas flow conditions, the temperature gradient along the channel is not only responsible for the heat flux, but it also results in the motion of the gas molecules. Similarly, the pressure gradient along the channel, not only moves the gas molecules, but also contributes to the heat flux. The direct simulation Monte Carlo (DSMC) technique is one of the most accurate molecular dynamics based techniques used for studying the phenomenon of thermal transpiration. It tracks a representative set of molecules used to study the dynamics of a system. The Boltzmann equation, in contrast, assumes a velocity distribution function to avoid tracking of the individual particles. Simplified forms of the Boltzmann equation are used to derive

analytical and semi-analytical models, such as those proposed by Maxwell [Max79], Williams [Wil70], Kennard [Ken38], Knudsen [Loe34] and Sharipov [Sha99]. Following sub-section give a brief overview of the DSMC techniques, Boltzmann equation and various analytical and semi-analytical models derived from the Boltzmann equation.

2.3.1 DSMC Technique

The DSMC technique is one of the most precise tools for analyzing the thermal transpiration gas flows: it tracks a statistically representative set of particles by calculating positions and velocities of these particles at every time step [Bir94, Ora98]. The particle motions are modeled deterministically, whereas the collisions are treated statistically. This method is useful only for dilute gas flows for which the average distance between the gas molecules is large in comparison to the molecular diameter. The method was first introduced by Bird [Bir63]. Since then it has been applied to various gas flow problems, such as the multidimensional flows, gas mixtures, flows with internal degrees of freedom, and chemically reacting gas flows [Bir63, Bir78].

Figure 2.3 shows a typical computational flow for the DSMC technique. The computational flow can be understood as a sequence of four basic steps: *particle movement*, *particle indexing and cross referencing, collision simulation,* and *sampling*. The information available for particles at microscopic level is used to evaluate the macroscopic attributes of the system.

The four step process can be summarized as [Ora98]:

1. *Particle Movement* – This step includes implementing the boundary condition on the particles leaving the container during a particular time step.

2. *Indexing and Cross-Referencing* – This involves division of space into cells and indexing various cells. An effective indexing and referencing is a key to the computational efficiency.
3. *Collision Simulation* – This step introduces the probabilistic aspect of the DSMC technique. An appropriate number of representative collisions between randomly chosen pairs of particles are simulated. The results are better if the collision of a chosen molecule is limited to the nearby particles

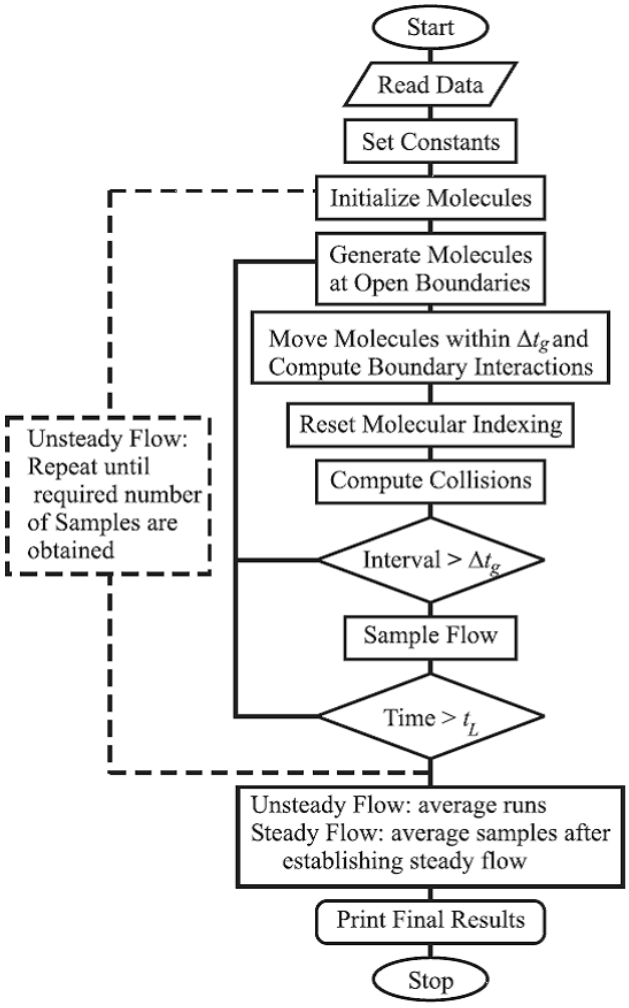

Fig. 2.3: DSMC flow chart – the computational flow can be understood as a sequence of four basic steps: *particle movement*, *particle indexing and cross referencing, collision simulation,* and *sampling*. This figure has been adapted from [Mas06].

only.

4. *Sampling* – In this step, the macroscopic properties of the system are calculated based on its microscopic attributes. The macroscopic properties may be sampled less frequently to increase the computational efficiency.

Although the DSMC technique is one of the most accurate techniques that can theoretically analyze all kinds of flows, its computational complexity restricts its usefulness as a design tool. Moreover, the computational cost makes it impractical and unnecessary to seek DSMC solutions for problems in slip flow and viscous flow regimes ($Kn < 0.1$), which can be modeled analytically with reasonable accuracy.

Attempts have been made to reduce the computational complexity of this molecular tracking technique without sacrificing its performance. Some of the recent versions of the DSMC technique that reduce the computational time of the molecular tracking technique include the DSMC – information preserving technique (DSMC-IP) [Fan99], the molecular block model for DSMC (MB-DSMC) [Pan01], and the Hybrid DSMC/Navier-Stokes methods [Has97, Rov98]. Although these improved techniques have been able to reduce the computational requirement of the DSMC technique to a certain extent, the computational cost of the technique is still high. Hence, an alternative modeling technique that can model the rarefied gas flow more optimally is required.

2.3.2 Boltzmann Equation

Unlike DSMC, the Boltzmann equation (BE) is based on a velocity distribution function, which can be used to evaluate various macroscopic characteristics of a system with rarefied gas flow. The concept of using velocity distribution was introduced

contemporarily by Maxwell and Boltzmann in their respective works. The velocity distribution function eliminates the need for tracking individual particles, which is computationally expensive. The resulting BE is [Col04, Col05, Cer06]:

$$\frac{\partial f_v}{\partial t} + \bar{v}.\frac{\partial f_v}{\partial \bar{x}} + \bar{F}.\frac{\partial f_v}{\partial \bar{v}} = Q(f_v, f_{v*}) \tag{2.1}$$

where, $\bar{F}$ represents imposed body forces, $\bar{v}$ is the velocity vector, $\bar{x}$ is the position vector, and f_v is the velocity density function. The rate of change in the density function ($\partial f_v/\partial t$) is caused by the change in f_v due to the molecular motion ($\bar{v}.(\partial f_v/\partial \bar{x})$), external body force ($\bar{F}.(\partial f_v/\partial \bar{v})$) and collision between molecules ($Q(f_v, f_{v*})$). The first term in the Eqn. 2.1 is the rate of change of number of particles with velocity $\bar{v}$. The second term represents convection of molecules, with velocity $\bar{v}$, across a volume element. The third term represents convection of molecules across the velocity space as a result of the external force $\bar{F}$. The fourth term is a generalized expression for the collision of two molecules.

The expression for the collision term is typically very complex, which makes it impossible to solve the BE analytically. Hence, in order to solve the BE analytically, the collision term must be simplified. Most of the analytical models for the phenomenon of thermal transpiration use the linearized BE with a simplified collision model. Each of these analytical models have a different sets of assumptions for simplifying the collision term in the BE. The set of assumptions used to simplify the BE for the derivation of a thermal transpiration model determines the limitations for the applicability of the model to various rarefied gas flow problems. Some of the most common assumptions for solving the BE include [Sha98]:

- The gas in the chambers, located at both ends of a narrow channel, is assumed to be in equilibrium far away from the channel ends.
- The flow regime in the capillary is assumed to be stable and not turbulent.
- The gas flowing through the channel is assumed to be dilute. Thus, the collision term can be simplified for the existence of only binary collisions.
- The equation is derived for monoatomic gas molecules, which makes simplification of the kinetic equation easier since the internal degrees of freedom can be neglected.
- The gas flow is assumed to comprise of single gas species, which helps in simplification of the kinetic equations.

2.3.3 Thermal Transpiration – Models

Different analytical models for the analysis of thermal transpiration driven gas flows, discussed in literature, are different variations of the BE obtained by simplification of the collision term under different assumptions. Amongst these various models, the following are some of the models that have been benchmarked against the DSMC: Maxwell [Max79], Knudsen [Loe34], Kennard [Ken38], Williams [Wil70] and Sharipov [Sha99]. The analytical expressions for each of these models and the corresponding limitations are discussed below. Some of these analytical models are applicable only to the circular channels. For such models, while analyzing thermal transpiration non-circular channels, the radius of the capillary is approximated by the hydraulic radius of the non-circular channel.

A. The Maxwell Model

Maxwell proposed one of the earliest mathematical correlations to study the isothermal, and near continuum gas flow rate, Q_{TT}, through narrow circular capillary with radius a. The mathematical expression for gas flow rate through a capillary subjected to a temperature gradient dT/dx and a pressure gradient dP/dx is given by [Max79]:

$$\frac{Q_{TT}}{\pi\rho a^2} + \frac{1}{8\mu}\left(a^2 + 4Ga\right)\frac{dP}{dx} - \frac{3}{4}\frac{\mu}{\rho T}\frac{dT}{dx} = 0 \tag{2.2}$$

where, the dynamic viscosity,

$$\mu = \left(\frac{1}{2}\right) N m \bar{u} \lambda \tag{2.3}$$

average velocity,

$$\bar{u} = \left(\frac{8R_g T}{\pi}\right)^{\frac{1}{2}} \tag{2.4}$$

mean free path,

$$\lambda = \frac{k_B T}{\sqrt{2}\pi D^2 P} \tag{2.5}$$

molecular density,

$$N = \frac{P}{k_B T} \tag{2.6}$$

density,

$$\rho = mN \tag{2.7}$$

coefficient of slipping,

$$G = \frac{2}{3}\left(\frac{2}{f_r} - 1\right)\lambda \tag{2.8}$$

where m is the mass of a gas molecule, R_g is the specific gas constant, D is the collision diameter of the gas molecues, k_B is the Boltz mann constant, T is the temperature along the narrow channel, P is the pressure along the narrow channel and f_r is a measure of molecular reflectivity of the surface of the narrow channel (f_r = 0.5 for half perfect reflecting surface and f_r = 1 for a perfectly reflecting surface).

In the absence of a pressure gradient, the gas flow is from the cold end to the hot end of the narrow channel. However, in the absence of any flow, the pressure is higher at the hot end of the tube; the resulting pressure gradient is:

$$\frac{dP}{dx} = 6\frac{\mu^2}{\rho T}\frac{1}{a^2 + 4Ga}\frac{dT}{dx} \tag{2.9}$$

This model assumes isothermal gas flow, which physically means that the motion of the gas molecules is slow and the temperature along the capillary walls varies so gradually that the temperature distribution across any section of the tube can be assumed to be uniform.

B. The Kennard Model

The Kennard model is same as the Maxwell model except for the fact that the coefficient of slipping in the Maxwell model is replaced by the slip length, which depends on the thermal accommodation coefficient of the surface. The Kennard model also assumes a near continuum (Kn<0.1) flow with moderate pressures. It assumes that the gas is dense enough to extend the Poiseuille's flow equation to accommodate temperature gradient. Kennard's model for thermal transpiration driven gas flow rate across a narrow channel with circular cross-section (radius a), under the assumption of isothermal gas flow is [Ken38]:

$$Q_{TT} = -\frac{\pi}{8}\frac{a^4 P}{\mu R_g T}\left(1+4\frac{\zeta}{a}\right)\frac{dP}{dx} + \frac{3\pi}{4}\frac{\mu a^2}{T}\frac{dT}{dx} \tag{2.10}$$

However, if the two ends of the tube are sealed, the creeping flow induced along the walls of the tube results in an equilibrium pressure gradient along the tube. The resulting pressure gradient pumps the gas against the thermal creep flow through the central region of the tube, such that the effective gas flow across any section of the narrow channel is zero. The expression for the pressure gradient is:

$$\frac{dP}{dx} = \frac{6\mu^2 R_g}{a^2 P\left(1+\frac{4\zeta}{a}\right)}\frac{dT}{dx} \tag{2.11}$$

C. The Williams Model

The Williams model is identical to Kennard's model except the slip length, ζ, which is expressed more precisely in terms of the coefficient of accommodation of the gas molecules to the channel walls. The slip length is:

$$\zeta = \frac{\mu}{\rho}\left(\frac{2-\sigma}{\sigma}\right)\sqrt{\frac{\pi R_g T}{2}} = \lambda\left(\frac{2-\sigma}{\sigma}\right) \tag{2.12}$$

For accommodation coefficient unity (σ = 1), the slip length becomes equal to the mean free path of the gas molecules (Eqn. 2.12), which is true for the Kennard model also. Hence, the Williams model can be seen as a more precise representation of the Kennard model, where Williams model represents the slip length in a rarefied gas flow in terms of the accommodation coefficient. The mathematical expression for the dependence of pressure gradient on the temperature gradient is [Wil70]:

$$\frac{dP}{dx}=\frac{6\mu^2 R_g}{a^2}\left[P+\frac{4\mu}{a}\left(\frac{2-\sigma}{\sigma}\right)\left(\frac{\pi R_g T}{2}\right)^{\frac{1}{2}}\right]^{-1}\frac{dT}{dx} \tag{2.13}$$

The Williams model operates on the following assumptions: constant fluid properties along the channel, gas flowing along a thin capillary with circular cross-section, isothermal gas flow, and near continuum gas flow.

D. The Knudsen Model

Unlike the Maxwell, Williams, Kennard models, the Knudsen model is an empirically corrected model that is applicable to either very small *Kn* or very large *Kn* gas flow though narrow circular capillaries. Like all the other models discussed above, this model also assumes isothermal gas flow along a capillary with circular cross-section. In the absence of any effective flow along the channel, the equilibrium pressure gradient resulting from an applied temperature gradient is [Loe34]:

$$\frac{dP}{dx}=\frac{1}{\frac{8}{3}\frac{1}{k_1}\frac{a}{\lambda}+\frac{\pi}{16}\left(\frac{0.81}{0.49}\right)\frac{a^2}{\lambda^2}\frac{1}{k_1}}\frac{P}{2T}\frac{dT}{dx} \tag{2.14}$$

where, k_1 is an empirically determined factor. $k_1=1$ if $Kn>>1$, else $2<k_1<3$

E. The Sharipov Model

Unlike the models discussed above, the Sharipov model is based on a more precise model, the S-model, to simplify the collision term in the BE. Hence, the Sharipov model is applicable to all the flow regimes ($Kn>0$). The average mass flow rate of gas through a capillary from the cold end to the hot end is:

(for circular capillary) [Sha97]

$$\dot{M}_{avg-C} = \left(\frac{Q_T \Delta T}{T_{avg}} - \frac{Q_P \Delta P}{P_{avg}} \right) \frac{\pi a^3 P_{avg}}{l} \left(\frac{m}{2k_B T_{avg}} \right)^{1/2} \tag{2.15}$$

(for rectangular channel) [Sha99]

$$\dot{M}_{avg-R} = \left(\frac{Q_T \Delta T}{T_{avg}} - \frac{Q_P \Delta P}{P_{avg}} \right) \frac{a_R^2 b_R P_{avg}}{l} \left(\frac{m}{2k_B T_{avg}} \right)^{1/2} \tag{2.16}$$

where, l is the length of the capillary, a is the radius of the capillary, a_R is the height of the (rectangular) channel, and b_R is the width of the (rectangular) channel. In the absence of the flow rate the equilibrium temperature gradient that exists to nullify the thermal transpiration driven flow is:

$$\frac{dP}{dx} = \frac{Q_T}{Q_P} \frac{P}{T} \frac{dT}{dx} \tag{2.17}$$

and Q_P and Q_T are the pressure and temperature coefficients that depend on rarefaction parameter δ_{avg}:

$$\delta_{avg} = \left(\frac{\pi^3}{2} \right)^{1/2} \frac{aD^2 P_{avg}}{k_B T_{avg}} = \frac{\sqrt{\pi}}{2Kn} \tag{2.18}$$

The viscous flow in the center of the channel follows Poiseuille's equation and the pressure gradient driven volumetric gas flow rate is:

$$Q_{POS} = \frac{\pi D_L^4}{128 \mu l} \Delta P \tag{2.19}$$

where, D_L is the diameter of the channel, which allows gas flow in viscous flow regime. ΔP is the pressure head across the channel.

2.4 Benchmarking of Models

As part of this thesis research, a test case was developed to benchmark the performance of the thermal transpiration models, discussed above, against the DSMC technique. The intent was to identify the limitations of these different analytical and semi-analytical models to determine their utility in designing practical Knudsen pumps. The test case presented here is based on a finite element (FE) model of the fully micromachined Knudsen pump which was fabricated on a pyrex glass substrate and had a footprint of 1.5x2 mm^2 [McN05]. The FE model is used to estimate the temperature profile along the narrow channel. Amongst the various models benchmarked against DSMC, the Sharipov model is the most promising alternative to the DSMC technique. Moreover, amongst the analytical models discussed above, only the Sharipov model is applicable over the full spectrum of the Knudsen numbers ($Kn > 0$).

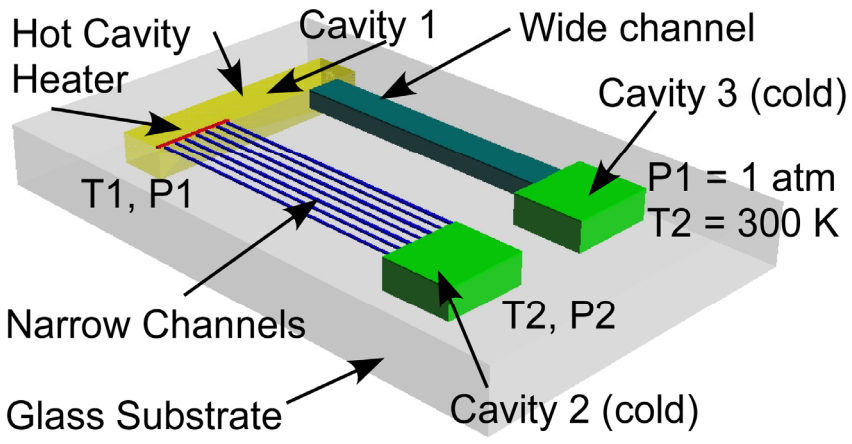

Fig. 2.4: 3D schematic of the fully micromachined Knudsen pump [Gup07]. The device has one heated cavity (#1) and two cold cavities (#2 and #3) passively maintained at room temperature. Cavities 1 and 2 are connected through narrow channels. Cavities 1 and 3 are connected via a wide channel.

2.4.1 Test Case – FEM Model

The test model has two cavities, one hot and one cold, which are connected by a set of nanochannels. The hot and the cold cavities in this case are analogous to the hot and cold chambers in Fig. 1.10. They are called cavities in this case because they are formed by etched out void spaces on a bulk SiO_2 wafer.

Figure 2.4 shows a 3D schematic of the model, which has multiple nanochannels connecting two cavities (cavity 1 and cavity 2). The two cavities are maintained at different temperatures – cavity 1 is heated and cavity 2 is passively held at room temperature. The heated cavity (cavity 1) is further connected through a wide channel to cavity 3, which remains at ambient pressure and temperature. These cavities (cavity 1, 2 and 3) and the wide channel connecting cavity 1 and cavity 3 are countersunk in a glass substrate. Each of the cavities is 10 μm deep and has a foot print of 160x50 μm^2,

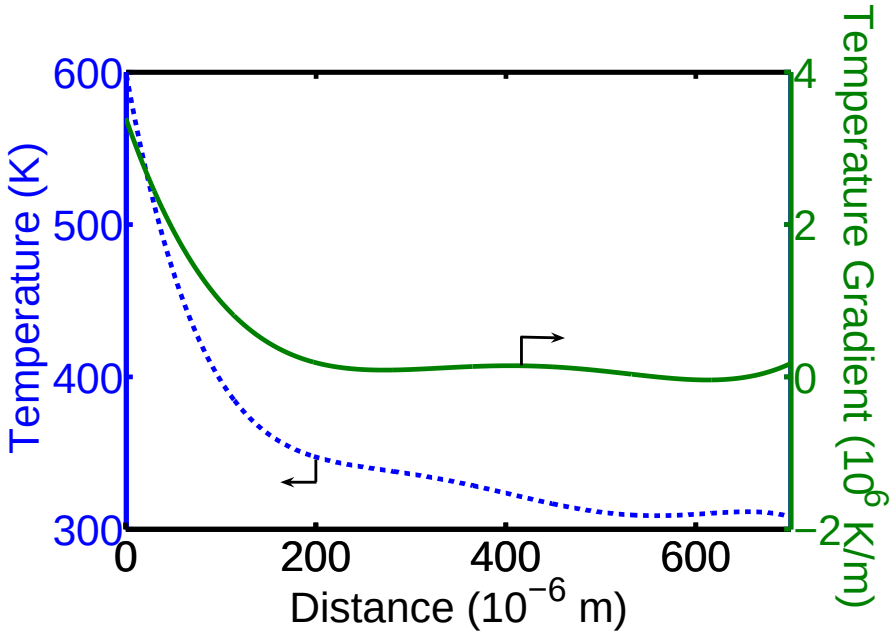

Fig. 2.5: Temperature distribution along the narrow channel (700 μm long). An ANSYS model is developed for the experimental device, shown in Fig. 2.4, to estimate the temperature distribution along the narrow channels based on the experimentally measured temperatures in the two end cavities [McN05, Gup06].

whereas the wide channel has a depth of 10 μm and width of 30 μm. The cavities are capped by a three layer $SiO_2/Si_3N_4/SiO_2$ dielectric stack; each of these layers is 300 nm thick. The narrow channels are patterned on polysilicon layer, which is sandwiched between the dielectric stack and the glass substrate. The poly layer is 1 μm thick except for the places where a sub-layer of 100 nm thickness is initially etched out to define narrow channels. Thus, the narrow channels are 10 μm wide and 100 nm deep. The polysilicon layer is etched away from the top of the hot and the cold cavities, which allows thermal isolation of the polysilicon heater present in the hot cavity. This heater hangs from the top dielectric stack and is located close to the ends of the narrow channels' opening in the hot cavity. This architecture achieves a thermal isolation of ≈1570 K/mm, while heating the hot chamber upto 1373 K with an input power of 80 mW.

A finite element based ANSYS model, with the topology discussed above, is used to compute the temperature distribution along the narrow channels (Fig. 2.5) [Gup06,

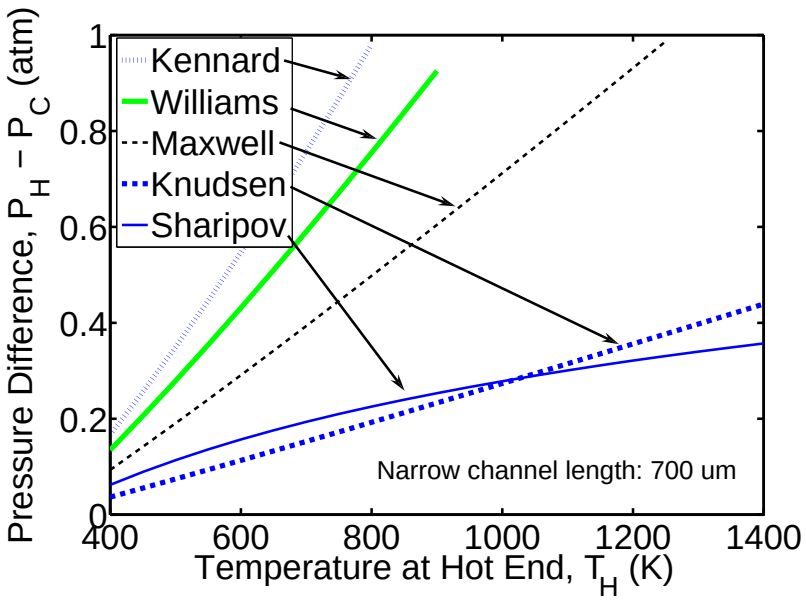

Fig. 2.6: Total pressure drop (P_H-P_C) along the narrow channel as a function of the temperature in hot chamber (T_H) – as predicted by various thermal transpiration models.

Gup07]. This temperature profile serves as an input to various analytical models, which are used to estimate the equilibrium pressure distribution along the narrow channel. The ANSYS model assumes a fixed temperature boundary condition (300 K) at the base. A convection boundary condition is imposed on the top and the side faces of the device with ambient at 300 K.

2.4.2 Results and Discussion

Figure 2.6 shows the steady state pressure drop (P_H-P_C = ΔP) across the narrow channels, as predicted by various models, for different temperatures (T_H) at the hot end of the 700 μm long narrow channels. For a given T_H, the temperature distribution along the narrow channel is assumed to follow a trend similar to that shown in the Fig. 2.5. The temperature profile for a T_H other than that shown in Fig. 2.5, is obtained by scaling up/down the profile shown in Fig. 2.5, while keeping the cold end temperature (T_C) at 300 K. Figure 2.6 shows that with the increase in T_H, the ΔP increases linearly for the Maxwell, Williams and Kennard models. The results from these three models suggest that T_H on the order of 1000 K would evacuate the cold cavity to zero pressure (i.e. P_C = 0 atm). This is not physically possible, because Eqn. 2.1 suggests that for complete evacuation of the cold chamber (i.e. P_C = 0 atm), the temperature at the hot end will need to be infinitely large. The Knudsen model and the Sharipov model have a more reasonable prediction of ΔP for a given T_H. Figure 2.6 shows that the Knudsen model also follows a linear trend, but a closer look at the mathematical expression (Eqn. 2.14) suggests that no finite value of T_H would result in complete evacuation of the cold chamber (i.e. P_C = 0 atm). Similarly, as T_H is increased from the room temperature, the Sharipov model predicts a higher initial ΔP than the Knudsen model. However, the rate

of the rise of the ΔP, with the increase in T_H, tends to reduce with increasing values of T_H. Thus, the Knudsen and Sharipov are physically more reasonable models for the analysis of the phenomenon of thermal transpiration.

The pressure profiles, as predicted by the Maxwell, Kennard and Williams models deviate significantly from the DSMC results, potentially because they are based on the analytical models that are corrected for first order velocity slip and temperature jump boundary conditions (Fig. 2.7). The Maxwell model accounts for the velocity slip at the channel boundary by a coefficient of slipping, G (Eqn. 2.8). The pressure profile evaluated using the Maxwell model, shown in Fig. 2.7, assumes the coefficient of slipping to be twice the mean free path of the gas molecules. Similarly, the Kennard model has a term called '*slip length*', which is typically on the order of the mean free path of the gas molecules. Slip length is the thin layer along the channel walls where the thermal creep flow occurs. The pressure profile evaluated using the Kennard model,

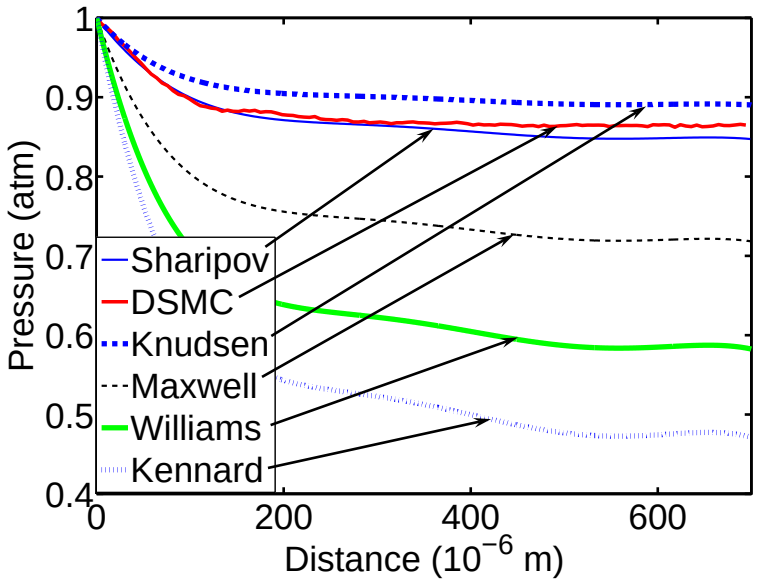

Fig. 2.7: The pressure distribution along the narrow channel as predicted by various analytical and semi-analytical models for thermal transpiration. These pressure profiles are benchmarked against the pressure profile obtained from the DSMC technique.

shown in Fig. 2.7, assumes the slip length equal to the mean free path of the gas molecules. Further, for the Williams model, the slip length is more rigorously defined in terms of the accommodation coefficient. The pressure profile presented here assumes the accommodation to be 0.87. The pressure profile by the Williams model, with unity accommodation coefficient, yields a pressure profile identical to the pressure profile by the Kennard model.

The pressure distribution along the narrow channel (Fig. 2.7) corresponding to the temperature profile shown in Fig. 2.5 suggests that the Sharipov model is the most representative model for the DSMC technique. The Sharipov model is potentially one of the most generic form of the semi-analytical model that is applicable to the full range of gas flow regimes ($Kn > 0$). It uses the S-model to simplify the collision term in the Boltzmann equation and then numerically integrate the equation for different flow regimes [Sha74]. The model has a set of numerically evaluated temperature and pressure gas flow coefficients that make this semi-analytical model reasonably precise, while preserving ease of use. Hence, the Sharipov model is the best alternative to the computationally expensive DSMC technique [Sha99].

The Knudsen model, an empirically corrected model for very low and very high Knudsen number flows, is applicable only to the narrow channels with circular cross-sections. Similarly, the Maxwell, Williams and Kennard models are applicable to the near continuum gas flows in the circular capillaries, whereas the model under consideration has gas flow in free molecular or transitional flow regime. Hence, the Knudsen, Maxwell, Williams and Kennard models are the less preferred models for the present analysis. The Sharipov model is preferred because it is applicable to the gas flow

in all the flow regimes. Moreover, unlike all other models, the Sharipov model can be applied to the thermal transpiration flow through rectangular channels, which will be more representative of the case being studied here. Apart from its applicability to all flow regimes, the Sharipov model is applicable to non-isothermal gas flows as well.

As part of this research effort, the applicability of the Sharipov model was further ascertained by another hypothetical test case, which benchmarks the thermal transpiration generated pressure profile predicted by the Sharipov model against the pressure profiles predicted by two types of DSMC techniques [Mas06]. Figure 2.8 shows the pressure profile from a series of numerical simulations that were performed on channels with a length of 5 μm and various heights (1 μm, 100 nm, and 20 nm respectively), which had a

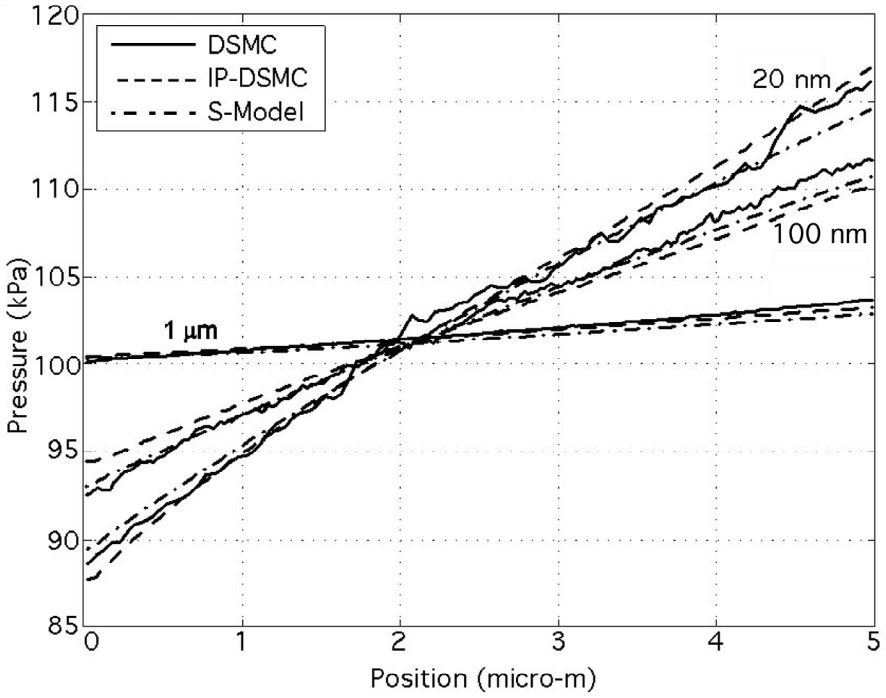

Fig. 2.8: Pressure profiles, for various channel heights, corresponding to a test case for which the temperature profile was assumed to be linear and ΔT = 300 K. The results from DSMC, IP-DSMC and S-model are in close agreement with each other for all the three cases. IP-DSMC differs from DSMC in exploiting the continuum behavior along with the particle dynamics to achieve a better computational performance. This figure has been adapted from [Mas06].

linearly varying temperature from 273 K to 573 K along the channels. The plots suggest that the results from the Sharipov model closely resemble those of the DSMC and the IP-DSMC results: IP-DSMC being a more efficient DSMC technique that blends information from continuum theory into particle dynamics to achieve a better computational efficiency [Mas06]. Once again, the ability of the Sharipov model to reproduce the results as predicted by the DSMC technique makes it a very strong candidate for the initial design and simulation requirements of the thermal transpiration driven flows.

The Sharipov model was then used to establish some scaling guidelines to design a Knudsen pump. Figure 2.9 shows a typical variation of the cold end pressure (P_C) with the variation in the channel heights, as predicted by the Sharipov model, for the 700 μm long channel. As expected, while operating at atmospheric pressure, the thermal

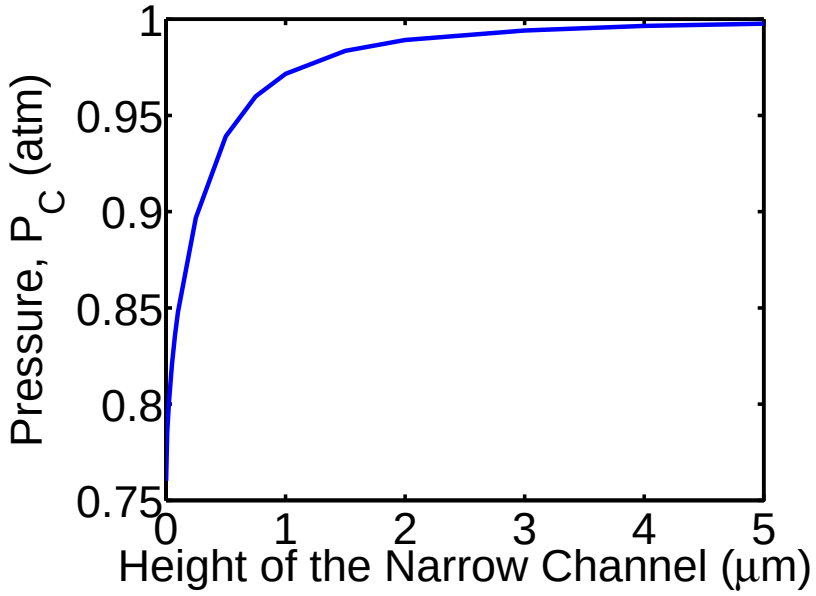

Fig. 2.9: An estimate of the vacuum pressures generated at the cold end of the channel for different channel heights. The Sharipov model is used to estimate the steady state vacuum pressure at the cold end of the narrow channel, 10 μm wide, while the hot end of the channel is vented to the ambient (that is P_H = 1 atm). The gas compression efficiency increases with decreasing channel height.

transpiration effects are observable for the narrow channels (Kn>1) with channel heights <100 nm. This is so, because for larger diameters the Poiseuille flow is large enough to nullify the flow induced by thermal creep. This suggests that a device with narrower channel heights is more effective in retaining a larger pressure difference across the narrow channel. However, for a smaller channel height the gas molecules flowing across the channel are reduced in number, hence the response time of the device will increase. Thus, the channel height is one of the control parameters for pressure differential achieved vs. the response time of a thermal transpiration based gas pump.

For vacuum pumping applications, the reduction in hot cavity pressure (P_H), results in a more effective vacuum (i.e. higher P_H/P_C) generated at the cold end of the narrow channel (Fig. 2.10). This indicates that an open system, for which cavity 3 is vented to the ambient, such that P_H can never exceed 1 atm., is more effective than a closed system.

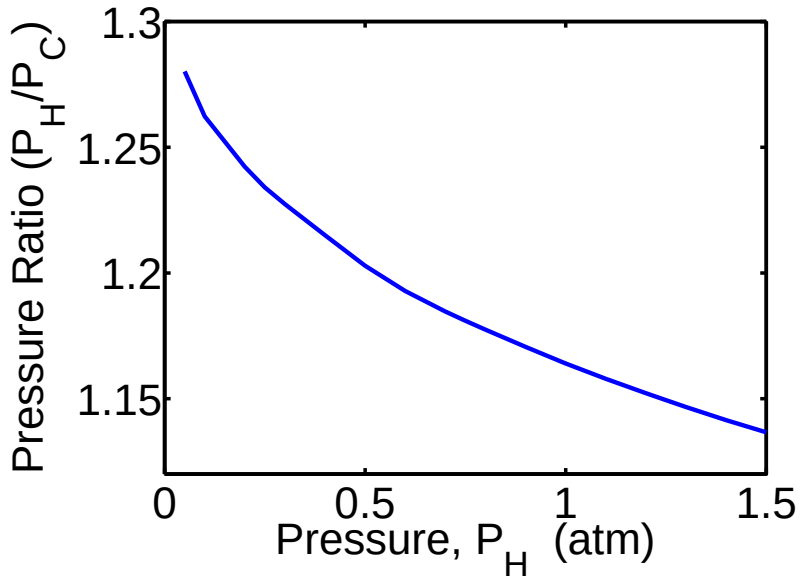

Fig. 2.10: An estimate of the pressure ratio at the two ends of the narrow channel for different hot end pressures. The Sharipov model is used to estimate the pressure ratio, at the two ends of the narrow channel – 10 μm wide and 100 nm high. The gas compression ratio increases with decreasing pressure at the hot end of the narrow channel. This is favorable for a multistage Knudsen vacuum pump.

Moreover, the plot in Fig. 2.10 also suggests that a multistage thermal transpiration driven vacuum pump will benefit from higher-pressure ratios in successive stages with the reduction in average operating pressure of a particular stage.

Finally, the Sharipov model suggests that unlike the case for gas compression, the gas pumping mechanism benefits from greater height of the narrow channels. The Sharipov model was used to evaluate the mass flux of gas through varying widths of narrow channels for channel heights of 50 nm (channel A) and 100 nm (channel B) at ambient pressure. The analysis suggests that as the height-to-width ratio reduces from unity, the mass flux through a channel of a given height increases and then attains a saturation value for widths much larger than the height (Fig. 2.11). This indicates that depending on the fabrication complexity, one can choose to have multiple channels with smaller widths, so long as the mass flux is in saturation regime. However, for higher mass flow

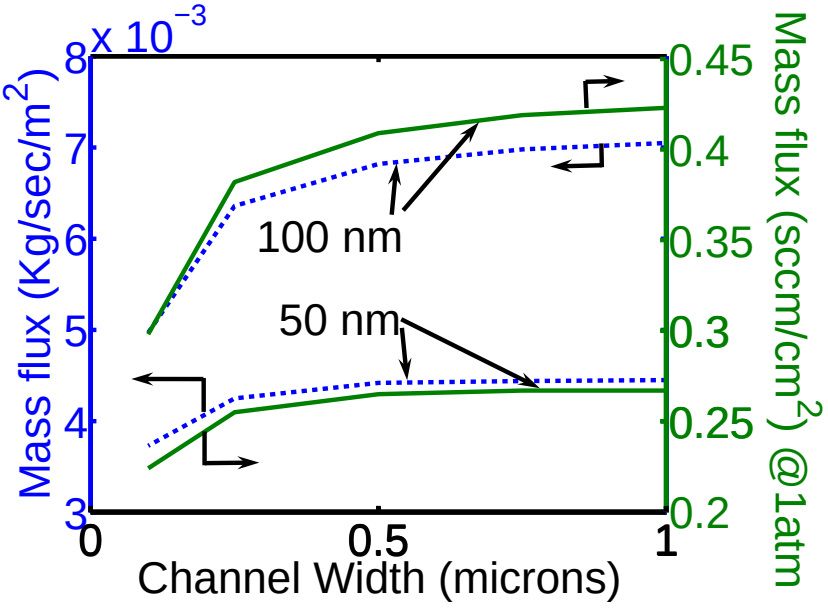

Fig. 2.11: The molecular flux across the narrow channels with two different heights for different channel widths. As the height to width ratio reduces from unity the molecular flux increases initially and then attains a saturation value. The molecular flux is high for channel with greater height.

rate channels with greater height are preferred, but as discussed earlier the channels with greater heights will essentially have lower pumping pressure capabilities.

2.4.3 Summary

The study suggests that the Sharipov model can be used to predict the behavioral response of a thermal transpiration driven microsystem with reasonable accuracy. Application of the Sharipov model to the Knudsen pump design suggests that: (a) Relatively high pressure ratios (P_H/P_C) are available at lower values of P_H in the hot chamber, thus predicting higher pressure ratios in the successive stages of a multistage Knudsen pump. (b) The mass flow rate calculations using the Sharipov model indicate that the mass flux increases with the channel height (for narrow channels), and for a channel with given height, the mass flux first increases with increasing width and then attains a saturation value for widths much larger than channel height. However, with the increasing channel heights the pumping pressure capability of the pump decreases. Hence, the Knudsen pump design requires an optimal choice between two opposing performance metrics – the desired gas flow rate and the desired pumping pressure.

.

CHAPTER 3

NANOPOROUS CERAMIC-BASED SINGLE STAGE KNUDSEN PUMP

One of the primary challenges faced with a typical Knudsen pump for conventional sensing applications at atmospheric pressure is that the thermal transpiration driven gas flow rates are low. This is so because the mean free path λ of air molecules at atmospheric pressure is 100 nm, approximately, which limits the diameter of flow channels. This chapter describes the use of bulk nanoporous materials for thermal transpiration in Knudsen pumps[2]. Bulk nanoporous materials have a high density of interconnected nanochannels ($\approx 10^{14}$ channels/cm^2), which can pump gas in parallel. Thus, Knudsen pumps using bulk nanoporous materials bear the promise of generating meaningful gas flow rates.

3.1 Nanoporous Ceramic (Zeolite) Based Knudsen Pump

A naturally occurring zeolite, clinoptilolite, is chosen to demonstrate the feasibility of thermal transpiration driven gas pumping using bulk nanoporous ceramic materials. Naturally occurring zeolites have a dense interconnected network of narrow channels ($>10^{14}$ pores/cm^2). Clinoptilolite, the zeolite used in this study, is one of the most

[2] Portions of this chapter have been published in Applied Physics Letters [Gup08b].

abundant and widely mined natural zeolites, and is easily machinable. It has nanopores with hydraulic diameter of ≈0.45 nm and has bulk porosity of ≈34% (Fig. 3.1) [Li05, Jia04]. It is an inexpensive, easily accessible and mechanically strong nanoporous material. The nanoporous structure of zeolites inherently provides them with high surface area to volume ratio and hence makes them favorable for various surface chemistry related applications, such as, domestic and commercial water purification, agriculture, construction, medicine and so on [Fen05, Gho99, Kes94, Oza06, Sak05, Smi99, Wei00].

3.1.1 Device Structure

The zeolite-based Knudsen pump designed as part of this research effort is intended to have a hot core and a cool exterior. It has two circular zeolite discs with a flexible heater (≈18.7 Ω) sandwiched between them (Fig. 3.2, 3.3). The heater is formed by a thin, etched-foil resistive element laminated between insulating layers of Kapton (Minco, MN). Perforated aluminum discs are used on both sides of the zeolite discs to improve

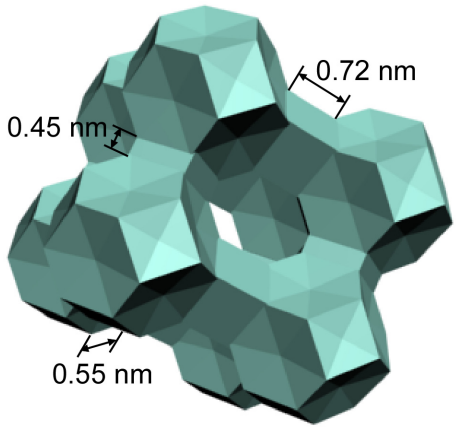

Fig. 3.1: Symbolic structure of the naturally occurring zeolite molecule, clinoptilolite. It has billions of parallel nanochannels formed by a dense interconnected network of nanopores (>10^{21} pores/cm^3, which is 10^{14} channels/cm^2). Clinoptiloite has an average pore diameter of 0.45 nm and bulk porosity of 34%.

the temperature uniformity on these surfaces without blocking the gas flow. This assembly is packaged in a thermally insulating polyvinyl chloride (PVC) cavity. The two zeolite discs are bonded peripherally to the cavity using a vacuum grade epoxy (STYCAST 2850FT/Catalyst 9) to prevent leakage. The thermally insulating PVC substrate leads to a higher temperature gradient across the thickness of the ceramic disc for a given input power, and this results in higher thermal efficiency. Stainless steel capillaries are used at the inlet and at the outlet ports. The device has two inlets one at the top and other at the bottom, and a common outlet for both sides of the pump is located at its center. Thermocouples, embedded in the top and the bottom aluminum discs, are used to record the temperature in the top and the bottom cold chambers, and a thermocouple, bonded to the heater, is used to record the temperature of the heater.

The zeolite discs divide the device into three compartments. The central portion, with heating element sandwiched between the two zeolite discs, comprises the hot chamber. Compartments formed between the zeolite discs and the PVC casings comprise the two cold chambers in the device.

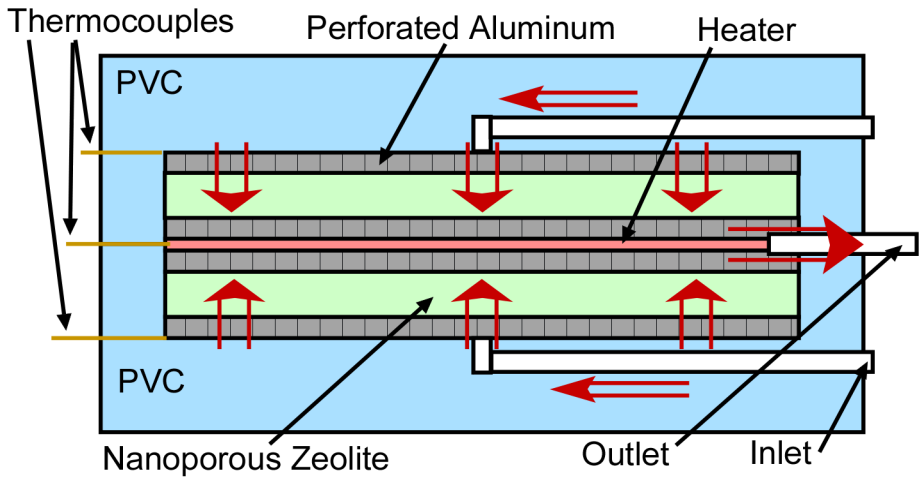

Fig. 3.2: Sectional view of a Knudsen pump with the heater sandwiched between two zeolite discs. This allows us to have hot core and cool exterior.

3.1.2 Steps of Fabrication

Figure 3.4 shows various steps of fabrication of the zeolite based thermal transpiration driven Knudsen pump. A PVC package is used for the pump; it consists of two halves that are bonded together after all the components are assembled into them. Each half has a circular pocket, ports for inlet, outlet, heater leads and thermocouple wires etc.

Step 1 shows the substrate half of the PVC package. For the current prototype (footprint ≈55x55 mm^2, and thickness ≈6 mm), it is machined conventionally, but can be

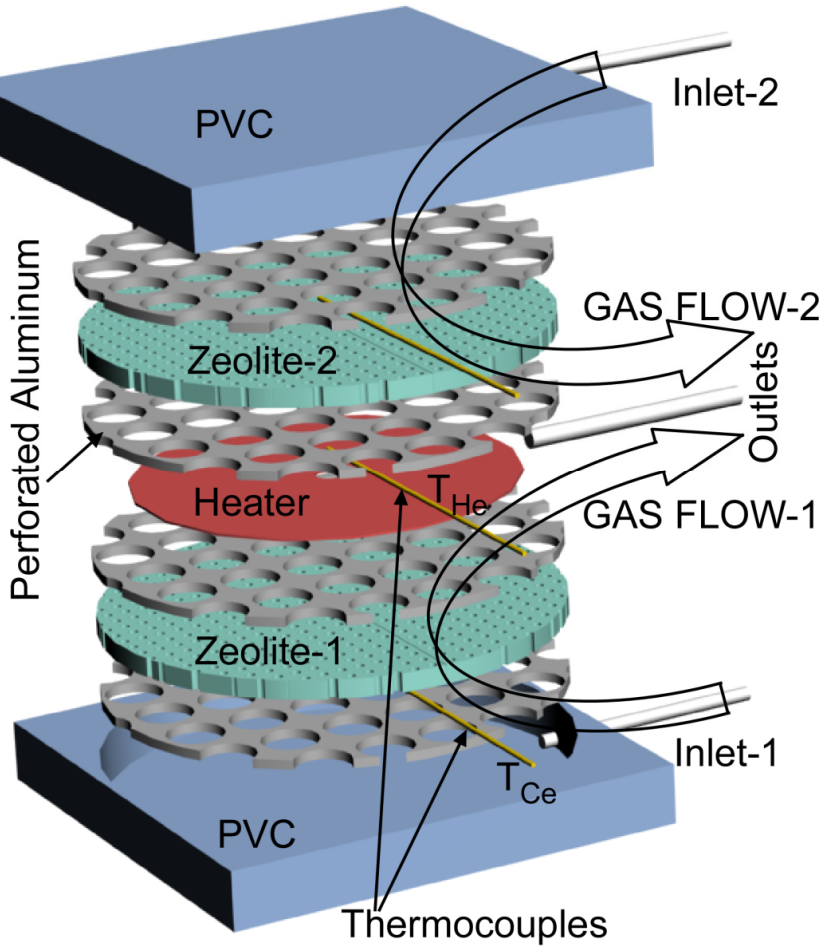

Fig. 3.3: Exploded view of a zeolite-based Knudsen pump showing relative location of various components. The double arrows show the direction of the flow of pumped gas.

formed by other means as well. For pumps with a small footprint or for high volume production, a molding process may be more appropriate.

Step 2 shows the substrate half of the PVC encapsulation with inlet SS capillary tube and the cold end thermocouple assembled in place using a vacuum grade epoxy. A disc

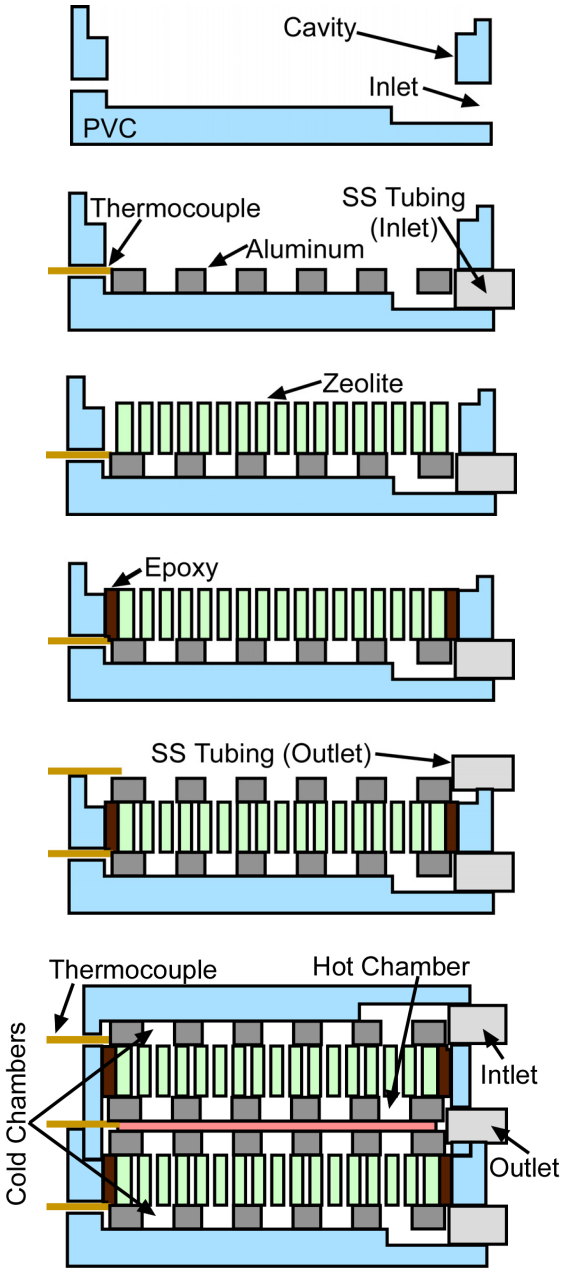

Step 1: Conventionally machined PVC encapsulation. It has a central cavity for zeolite pumping assembly and ports for gas inlet tubing and thermocouples.

Step 2: SS Inlet tubing, perforated aluminum and thermocouple installed in place.

Step 3: Zeolite disc is placed on the bottom (perforated) Aluminum layer.

Step 4: A vacuum grade epoxy is used to bond the zeolite to the PVC encapsulation at its periphery.

Step 5: A second thin layer of (perforated) aluminum is placed on the top of the zeolite. An outlet SS tubing and second thermocouple are assembled in place.

Step 6: A second half similar to that in step 5 is used to cap the structure in step 5 with an intermediate layer of thin film heater. The two structures are identical except for the fact that the second half does not have separate outlet tubing and second thermocouple.

Fig. 3.4: A typical fabrication sequence for a bulk nanoporous material based Knudsen pump.

of perforated aluminum is inserted into the cavity in the PVC. The disc is punched out of a sheet with 850 μm thickness and ≈15 perforations per cm^2.

Next, a zeolite disc that is machined into desired shape is placed above the perforated aluminum (Step 3, Fig. 3.4). Diamond machining tools are used to shape the zeolite – a cylindrical core (≈48 mm diameter) is cut out of a bulk zeolite rock, which is then sliced into discs of desired thicknesses (≈2.3 mm).

The zeolite disc is bonded to the PVC structure at its periphery, using a vacuum grade epoxy (Step 4, Fig. 3.4). The vacuum epoxy shields the hydraulic path for the gas flow from one side of the zeolite to the other. This results in an isolated air pocket underneath the zeolite – this air pocket is one of the cold chambers of the Knudsen pump (Fig. 1.2).

The zeolite is then covered by another thin perforated layer of aluminum (Step 5, Fig. 3.4). A SS capillary, which serves as output to the pump, is bonded to the outlet port of the PVC encapsulation located at the top of the zeolite wafer. A second thermocouple required to measure the temperature at the hot end of the zeolite is assembled onto the device.

Steps 1 to 5 are followed to fabricate the second half, which is similar to first one, except for the fact that the second half shares the outlet port and the thermocouple at the hot end of the zeolite with the first half. This second half is flipped and bonded on the top of the first half, such that the heater is sandwiched between the two zeolite discs (step 6, Fig. 3.4). This configuration has the advantage that the hot core of the structure is adjacent to two different thermal transpiration elements, while the cold sides of these zeolite discs face the outside. Thus, the cold sides of the zeolite discs can be easily maintained at lower temperature without penalizing the thermal budget of the device.

The device has a final packaged volume of 55x55x12 mm^3 (Fig. 3.6).

3.2 Fitted Model

A semi-analytical model was developed as part of this research effort to study the system level transient response of the Knudsen pumps based on bulk nanoporous materials. In particular, the model is used to estimate the temporal evolution of pressure at the sealed outlet (i.e. hot chamber) of these pumps. Three physical phenomena that

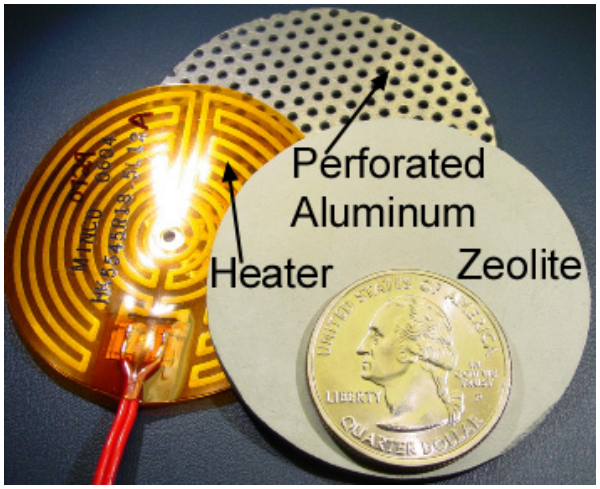

Fig. 3.5: Various components used in a zeolite-based Knudsen pump – zeolite disc, thin-flexible heating element, and perforated aluminum disc.

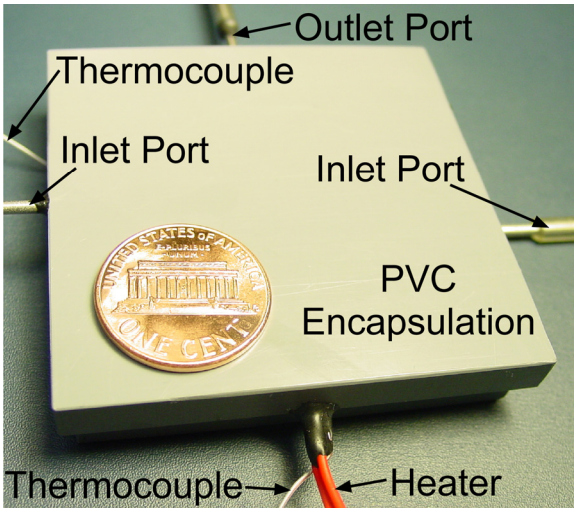

Fig. 3.6: Picture of the final device; it has a final packaged volume of 55x55x12 mm^3.

play dominant role in the temporal evolution of pressure at the sealed outlet of a Knudsen pump were identified. These include: (a) thermal transpiration driven gas flow across the nanoporous ceramic; (b) thermal expansion/contraction of air in the hot chamber; and (c) pressure gradient driven leakage flow through various structural imperfections in the ceramic. The first phenomenon is responsible for gas pumping in a Knudsen pump; the latter two do not contribute to gas pumping. In fact, the third phenomenon, pressure driven leakage flow, is not desirable, because it counteracts the thermal transpiration driven gas flow. The fitted model presented here quantifies various non-idealities in terms of four fitted parameters.

Analysis suggests that the initial transients of the Knudsen pumps, which occur as soon as the heater is turned on or off, depend strongly on the rate of thermal expansion/contraction of air encapsulated in the hot chamber. Experimentally measured temperature, T_{He}, is used to estimate the thermal time constants of the heater, τ_{htr}. A fitted parameter, f_{air}, is used to estimate the factor by which the thermal time constant for the air, τ_a, entrapped in the hot chamber exceeds τ_{htr}. Hence:

$$\tau_a = f_{air}.\ \tau_{htr} \tag{3.1}$$

A second fitted parameter, the leak aperture diameter, D_L, in nanoporous ceramic, is used to model the pressure driven leakage flow across the ceramic. A typical nanoporous ceramic has grain boundaries, crystal imperfections and other structural imperfections that may have hydraulic diameter significantly greater than the mean free path of the gas molecules (i.e. Kn<0.01) [Kar05]. Literature suggests that the grain boundaries of a natural clinoptilolite can have mesopores ranging from 25-50 nm upto 100 nm, and crystal boundaries have been reported to have macropores with an aggregate pore size of

500 nm [Kow06]. Some of these defects may result from the choice of manufacturing techniques. The gas flow through these imperfections is in the viscous regime and it counteracts the thermal transpiration-driven gas pumping through the nanopores. The pressure driven gas flow across the leak apertures is representative of the total leakage flow out of the hot chamber. For a given nanoporous material, D_L may vary from device to device because, apart from crystal imperfections, it also accounts for leakage flow across the packaging etc.

A third fitted parameter, κ, is used to quantify the fraction of experimentally measured temperature bias that actually appears across the nanoporous ceramic. The actual temperature drop that appears across the thickness of the ceramic disc is smaller than the experimentally measured value due to the thermal contact resistances at various interfaces. Thermal contact resistances at these interfaces are primarily due to micro-asperities and surface roughness. These micron size features are functionally important because they serve as the hydraulic paths for the gas molecules moving in/out of the ceramic disc. The (overall) loss in temperature bias due to the thermal contact resistances is modeled as parasitic heating of the bottom facet of the ceramic disc. All other interfaces are assumed to have no thermal contact resistance. The fitted parameter κ quantifies the rate of parasitic heating of the bottom facet of the ceramic.

Finally, a fourth fitted parameter, V_{crr}, corrected volume of the hot chamber, is used to account for non-uniformity in temperature of air molecules in the hot chamber. As mentioned earlier, the hot chamber has a SS outlet, which is connected to a pressure sensor through (slender) clear Tygon tubing. The air molecules in vicinity of the heater are significantly hotter than the gas molecules away from the heater. This non-uniformity

in temperature of air molecules in the hot chamber is modeled by dividing the air molecules into two sets, each of them at two different but uniform temperatures. The first set of air molecules, close to the heater, is assumed to have temperature same as the hot facet of the nanoporous ceramic, that is, T_{Hm}; second set of air molecules is assumed to be at ambient temperature T_{amb}. The volume occupied by the first set of air molecules at ambient temperature and pressure is assumed to be V_{crr}. For the purpose of the model presented here, the corrected volume is treated as the actual volume of the hot chamber and the air encapsulated in this volume is assumed to heat up with the heater to a steady state temperature T_{fin}, but with an increased time constant τ_a.

The fitted model presented here takes into account the three physical phenomena listed above and establishes a step-by-step procedure to estimate the four fitted parameters such that the root mean square (RMS) error between the estimated and the experimentally measured temporal evolution of pressure at the sealed outlet is minimized.

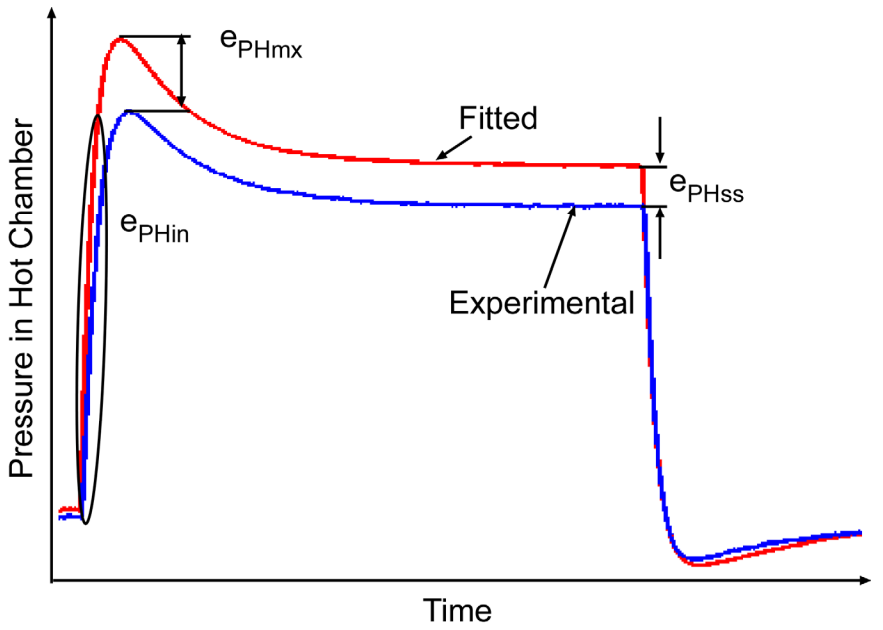

Fig. 3.7: Typical variation in the estimated (i.e. fitted) and the experimentally measured temporal evolution of pressure at the sealed outlet of a Knudsen pump.

Figure 3.7 shows a typical variation in the estimated (i.e. fitted) and the experimentally measured transient pressures at the sealed outlet of a Knudsen pump. The deviation of fitted pressure profile from the experimental pressure profile can be minimized in four steps:

1. The difference between the steady state values of the experimental and the fitted pressure profiles, e_{PHss}, has been observed to depend primarily on D_L. Hence, the error e_{PHss} is minimized by choosing D_L appropriately.
2. The RMS error between the fitted and the experimental pressure profile immediately after the heater is turned on or off, e_{PHin}, has been observed to depend primarily on f_{air}. Hence, the error e_{PHin} is minimized by choosing f_{air} appropriately.
3. The difference between the maximum pressure values for the fitted and the experimental pressure profiles, e_{PHmx}, has been observed to depend primarily on V_{crr}. Hence, the error e_{PHmx} is minimized by choosing V_{crr} appropriately.
4. The fitted parameter κ is used to minimize the total RMS error, e_{RMS}, between the fitted and the experimental pressure profiles. Hence, the error e_{RMS} is minimized by choosing κ appropriately.

Figure 3.8 shows the flowchart for the fitted model and a detailed step-by-step algorithm for the fitted model is presented below:

Step 1: Choose a suitably small time step (Δt) and interpolate $T_{He}(t)$, $T_{Ce}(t)$ and $P_{He}(t)$ for all the time steps.

Step 2: Choose initial values for D_L, κ, f_{air}, and V_{crr}. Due to the asymmetric nature of the problem, some of these parameters may have different values, while the heater is on and while it is off.

Step 3: Estimate the initial number of moles of air in the hot chamber based on the initial temperature, pressure of the device and the corrected volume of the hot chamber.

$$N(0) = \frac{P_{He}(0).V_{crr}}{R.T_{He}(0)} \tag{3.2}$$

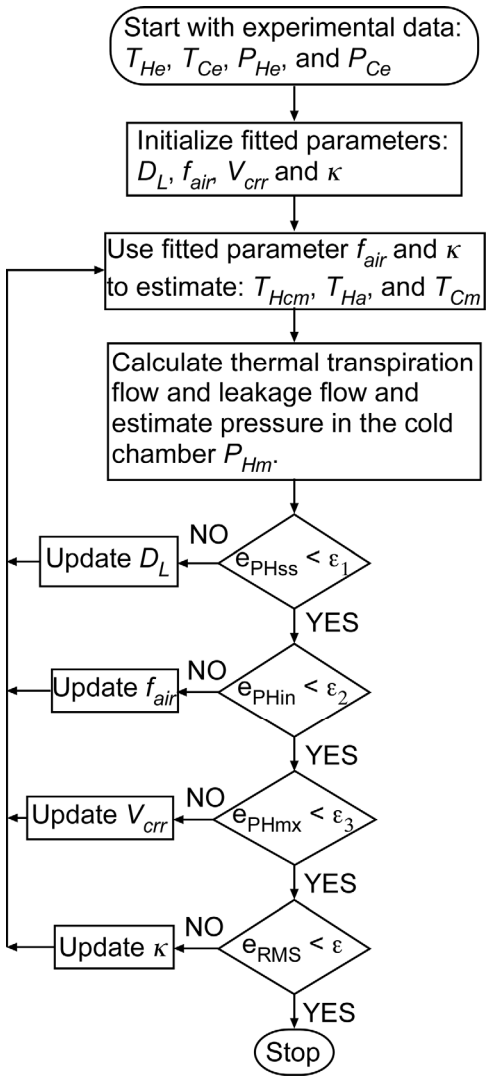

Fig. 3.8: The flowchart for key steps involved in the fitted model.

Step 4: The temperature at the hot facet of the ceramic $T_{Hm}(t)$ is assumed to be same as the experimentally measured temperature $T_{He}(t)$. So:

$$T_{Hm}(t) = T_{He}(t) \tag{3.3}$$

Step 5: The steady state temperature of the hot end of the ceramic with the heater on is T_{fin}. The air in the hot chamber is assumed to attain the same steady state temperature, but with a longer time constant τ_a ($= f_{air}.\tau_{htr}$). Use τ_a to estimate the temperature of the air in the hot chamber $T_{Ha}(t)$ as a function of time t.

$$T_{Ha}(t) = T_{in} + (T_{fin} - T_{in}).(1 - e^{-t/\tau_a}) \tag{3.4}$$

Step 6: The fitted parameter κ for the rate of parasitic heating of the cold facet of the ceramic is used to estimate the temperature of the cold facet of the ceramic:

$$T_{Cm}(t+\Delta t) = T_{Ce}(t+\Delta t) + [T_{Cm}(t) - T_{Ce}(t)] + \kappa.\Delta t \tag{3.5}$$

Step 7: The transient evolutions of pressure at every time step has been addressed as combination of two independent sub-steps. First sub-step: For any change in heater temperature during the time interval t to $t+\Delta t$, ideal gas law is used to estimate the intermediate pseudo-equilibrium pressure P_{Hi} ($t+\Delta t$).

$$P_{Hi}(t + \Delta t) = \frac{P_{Hm}(t)}{T_{Ha}(t)} T_{Ha}(t + \Delta t) \tag{3.6}$$

Step 8: Second sub-step: Average values for T_{Hm}, T_{Cm} and P_{Hi} are used to estimate the thermal transpiration gas flow and the Poiseuille (leakage) flow during the time t to $t+\Delta t$.

$$\overline{P}_{Hi}(t + \Delta t) = \frac{P_{Hi}(t + \Delta t) + P_{Hm}(t)}{2} \tag{3.7}$$

$$\overline{T}_{Hm}(t + \Delta t) = \frac{T_{Hm}(t + \Delta t) + T_{Hm}(t)}{2} \tag{3.8}$$

$$\overline{T}_{Cm}(t + \Delta t) = \frac{T_{Cm}(t + \Delta t) + T_{Cm}(t)}{2} \tag{3.9}$$

Step 9: Substitute for $T_H = \overline{T}_{Hm}(t+\Delta t)$; $T_C = \overline{T}_{Cm}(t+\Delta t)$; $P_H = \overline{P}_{Hi}(t+\Delta t)$ and $P_C = P_{amb}$ in Eqn. 2.15 to calculate the thermal transpiration driven mass flow rate and divide it by the molecular mass M of air to estimate the number of moles of gas molecules $N_{TT}(t+\Delta t)$ pumped into the hot chamber.

Step 10: Substitute $P_H = \overline{P}_{Hi}(t+\Delta t)$, $P_C = P_{amb}$ and use D_L in Eqn. 2.19 to calculate the leakage flow, multiply it with the density of air (Eqn. 2.7), and divide it by the molecular mass M of air to estimate the effective number of molecules $N_{POS}(t+\Delta t)$ leaking in/out of the hot chamber.

Step 11: The effective number of moles of gas in the hot chamber after time $t+\Delta t$ is calculated by accounting for the gas molecules moving in and out of chamber due to the thermal transpiration flow and Poiseuille flow.

$$N(t+\Delta t) = N(t) + N_{TT}(t+\Delta t) - N_{POS}(t+\Delta t) \tag{3.10}$$

Step 12: Estimate the final pressure in the chamber

$$P_{Hm}(t+\Delta t) = \frac{P_{Hi}(t+\Delta t)}{N(t)} N(t+\Delta t) \tag{3.11}$$

Step 13: Increment time, i.e. $t = t+\Delta t$; and repeat steps 5 to 12 for all the time steps.

Step 14: Update D_L and repeat steps 5 to 13 until e_{PHss} is smaller than ε_1, where ε_1 is the acceptable tolerance in minimizing e_{PHss}.

Step 15: Update f_{air} and repeat steps from 4 to 14 until e_{PHin} is smaller than ε_2, where ε_2 is the acceptable tolerance in minimizing e_{PHin}.

Step 16: Update V_{crr} and repeat steps from 3 to 15 until e_{PHmx} is smaller than ε_3, where ε_3 is the acceptable tolerance in minimizing e_{PHmx}.

Step 17: Update κ and repeat steps from 3 to 16 such that e_{RMS} is smaller than ε, where ε is the acceptable tolerance in minimizing e_{RMS}.

In the end, the model gives an estimate for the fitted parameters V_{crr}, D_L, f_{air}, and κ, such that the RMS error between the experimentally measured and the fitted pressure in the hot chamber is minimized. Note than the tolerances ε_1, ε_2, ε_3, and ε may vary from one iteration to the next.

3.3 Experimental Results

While the structure described in Section 3.1 is capable of pumping simultaneously through both the zeolite discs that sandwich the heater, only one side of the pump (only the bottom zeolite discs in Fig. 3.3) was used for the preliminary characterization.

3.3.1 Test Set-Up

Two different experimental set-ups are described in this section. The first set-up was used for isothermal pressure driven gas flow characterization of the nanoporous ceramic

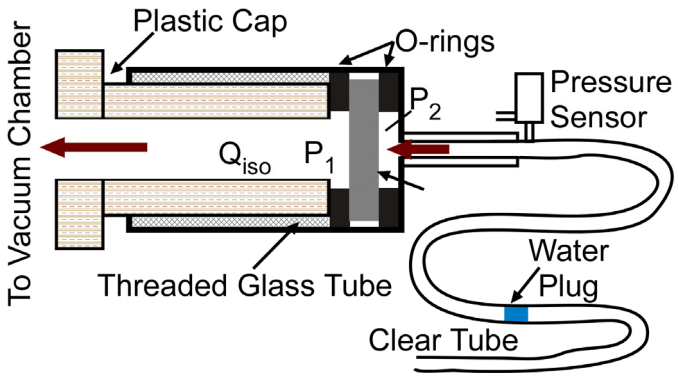

Fig. 3.9: Test set-up for isothermal pressure driven gas flow characterization of the nanoporous ceramic discs. The ceramic disc was sandwiched between two "O"-rings and vacuum pressure was applied from the left side to create a known pressure difference across the ceramic.

discs (Fig. 3.9). A 25 mm diameter disc of nanoporous ceramic sample was sandwiched between a threaded glass tube and its plastic cap. "O"-rings were used to seal the ceramic disc between the glass tube and the plastic cap. The glass tube, ceramic disc, and plastic cap assembly was mounted in horizontal position. The plastic cap was connected to a vacuum chamber, which was used to apply an externally controlled pressure differential across the nanoporous ceramic. The other end of the glass tube was connected to clear Tygon tubing with a water plug to visualize and quantify the gas flow across the ceramic disc. The Tygon tubing was laid down horizontally to eliminate the effect of gravity on the movement of the water plug. These tests were performed in ambient air at room temperature (≈293 K) and atmospheric pressure (≈735 Torr).

The second test set-up was used to study the temperature gradient driven thermal transpiration flow characteristics of Knudsen pumps (Fig. 3.10). As shown in the Figure 3.10, the Knudsen pump was kept on a large metallic block, which acted as a heat sink required to cool the bottom facet of the lower zeolite disc (Fig. 3.3). The metallic block

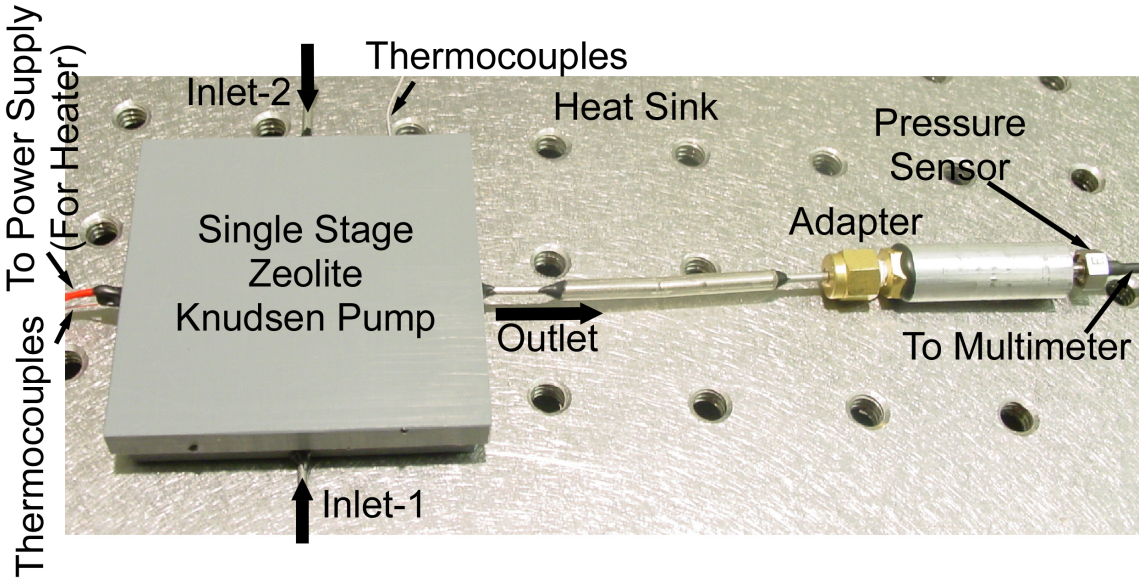

Fig. 3.10: Pressure Mode Testing: Experimental set-up for pressure measurement at the sealed outlet.

was maintained at room temperature passively. With this apparatus, the device was tested in two different operation modes: *pressure mode* and *flow mode*. While operating in pressure mode, the outlet was sealed, a differential pressure sensor (Kulite Semiconductor Inc., NJ) was attached at the sealed outlet, and the inlet was open to the ambient (Fig. 3.10). The pressure sensor was used to record the temporal evolution of pressure at the sealed outlet. It had a sensitivity of 10.8 mV/psi (1.57 mV/kPa). Voltage output from the pressure sensor was read into HP34401A multimeter, which was connected to a PC using a GPIB-USB-HS. *HP Benchlink* program was used to acquire voltage output measured by the multimeter at a sampling frequency of about 1 Hz.

While operating in flow mode, the inlet was open to the ambient. At the outlet, a flexible, clear Tygon tubing (ID 1.57 mm) with water droplet plug (≈2 mm long) was connected to the Knudsen pump (Fig. 3.11). The water plug was used to visualize and quantify the gas flow rate generated by the Knudsen pump. The load pressure was estimated by the length of the droplet.

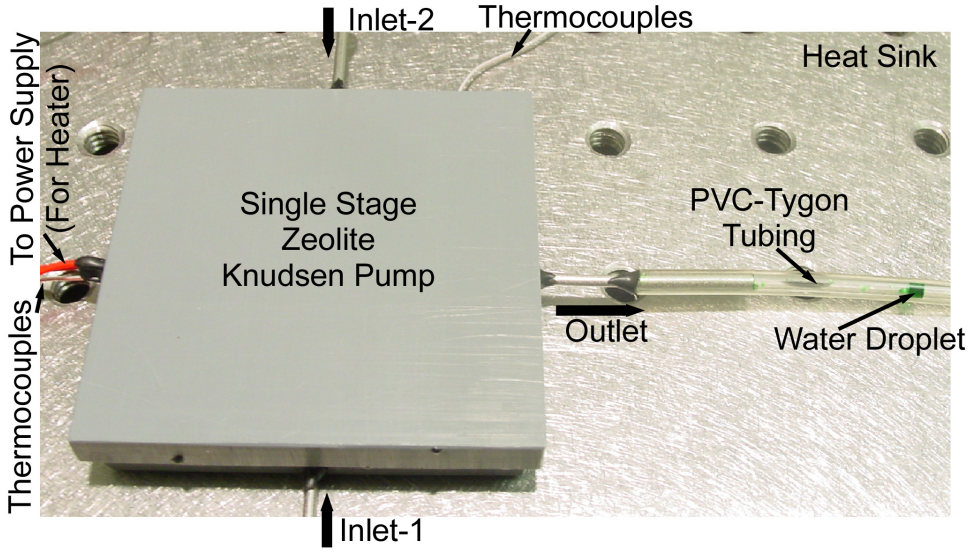

Fig. 3.11: Flow Mode Testing: Experimental set-up with flexible tubing attached to the outlet of the device and with a water droplet plug in it. The rate of movement of water droplet quantifies the rate of gas flow generated by the pump.

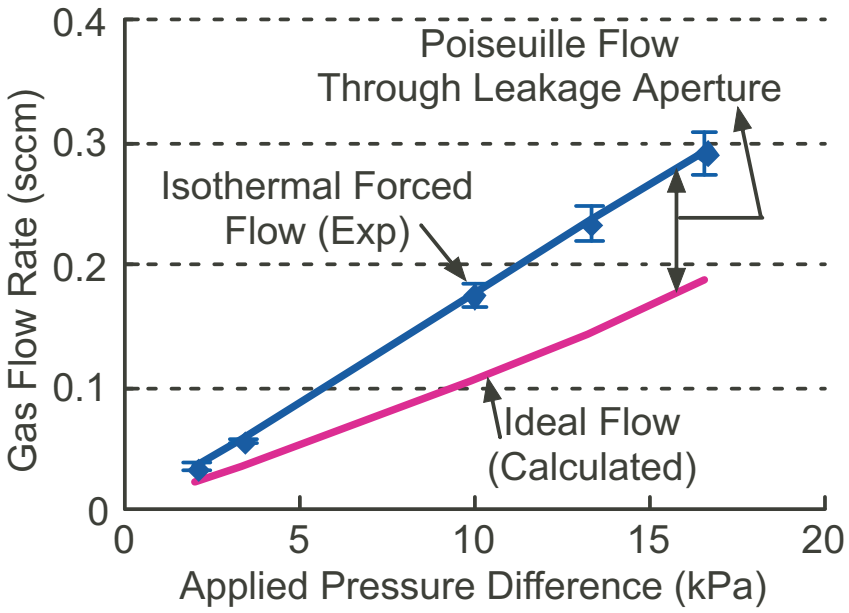

Fig. 3.12: Experimental characterization of pressure driven gas flow across a typical ≈25 mm diameter and ≈1.15 mm thick zeolite disc.

3.3.2 Steady State Response

Isothermal Poiseuille Gas Flow: Figure 3.12 plots the experimentally measured isothermal pressure driven gas flow across the zeoltie disc (diameter ≈25 mm and thickness ≈1.15 mm). The same plot also shows the corresponding flow rate expected under conditions assuming a perfect zeolite element of 0.45 nm pore size and 34% porosity, as calculated from Eqn. 2.15. The two flow rates deviate because of various leakage flow paths that might exist across the thickness of the zeolite. The difference between the experimentally measured flow and the ideal flow for the nanoporous material indicates the leakage (Poiseuille) flow. Equation 2.19 was used to estimate the leak aperture diameter in the zeolite discs based on the leakage flow estimated from Fig. 3.12. Figure 3.12 suggests that 1.15 mm thick clinoptilolite samples have typical leak aperture diameters per unit area of transpiration element (d_L) of 10.2-13.5 μm/cm^2:

$$\frac{D_L}{d_L} = \left(\frac{\pi D_{TE}}{4} \right)^{0.25} \tag{3.12}$$

where, D_{TE} is the diameter of the transpiration element with leak aperture D_L.

Device Response: The device, while operating with a single zeolite element, resulted in a gas flow rate of 0.12 sccm, against a nominal pumping load presented by the water plug (Fig. 3.13). The driving voltage for this device was 10 V and the power required was 5.35 W. This resulted in a temperature drop of about 40 K across the 2.3 mm thick zeolite, while limiting the temperature rise at the cold end of zeolite to 17 K. A Tygon tube (inner diameter ≈1.57 mm) with water plug (2 mm long) was connected at the outlet to visualize and quantify the gas flow generated by the pump.

The pumping load offered by a water plug has two components – resistance due to viscous drag at the capillary wall and the water interface, and resistance due to the

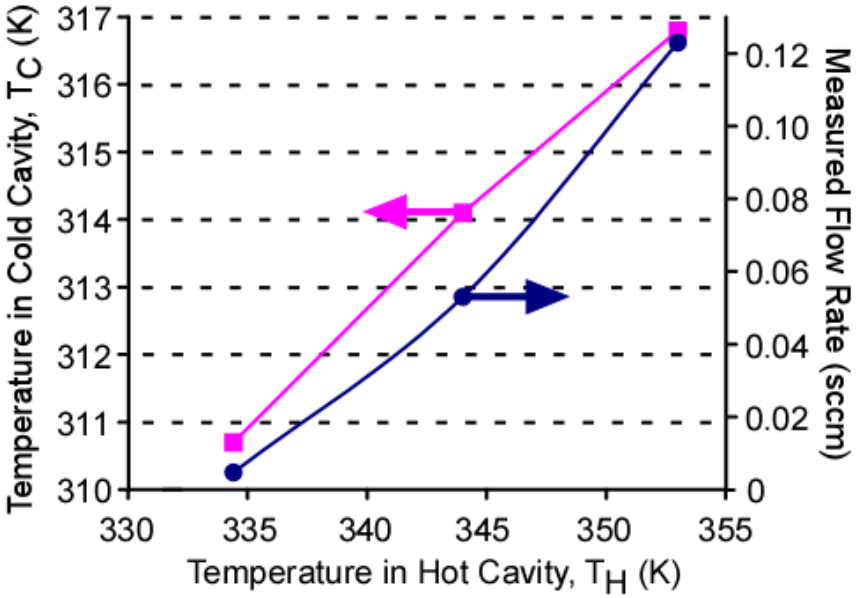

Fig. 3.13: Experimentally observed steady state flow rates for one side of the pump, as the hot cavity temperature is changed. Parasitic heating of cold cavity is also plotted. Unloaded gas flow rate is slightly higher because the droplet presents a small load (≈50 Pa).

movement of the two end menisci of the water plug. The movement of the end menisci involves continuous absorption and release of free energy, which translates into the pumping load required to move the plug. A preliminary estimate of the flow resistance offered by the water droplet was obtained using [Mye05]:

$$\Delta P_{\text{int}} = \frac{2\sigma \cos\beta}{r} \tag{3.13}$$

This correlation suggested that the flow resistance offered by a 2 mm long water droplet

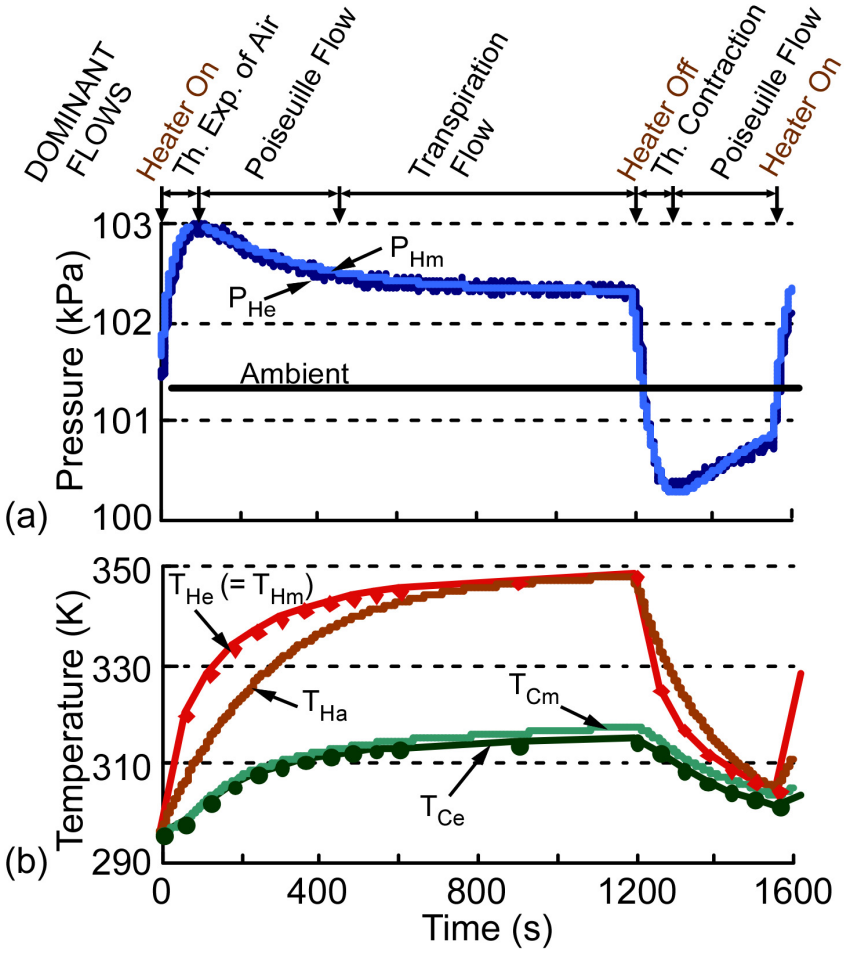

Fig. 3.14: (a) Experimental (P_{He}) and modeled (P_{Hm}) pressure transients recorded with a sealed outlet for a single side of the Knudsen pump, showing a root mean square error of <0.15 kPa. (b) T_{He} and T_{Ce} show the recorded temperature from the thermocouples. The corrected temperatures are T_{Hm} and T_{Cm} respectively. T_{Ha} is the temperature of the air encapsulated in the hot chamber.

in Tygon tubing with 1.57 mm inner diameter was about 50 Pa.

3.3.3 Transient Response

Figure 3.14 shows the experimentally measured pressure (P_{He}) at the sealed outlet of the Knudsen pump. The corresponding experimental measurement of the temperature at the hot and the cold ends of the zeolite disc are plotted as T_{He} and T_{Ce}, respectively. The plots suggest that as soon as the heater was turned on, the experimentally measured pressure increased sharply from 101.3 kPa to 103 kPa within 120 seconds and then decayed to a steady state value of about 102.3 kPa. Similarly, as soon as the heater was turned off, the experimentally measured pressure droped almost instantaneously to a pressure lower than the atmospheric pressure (≈100.3 kPa) and then rose asymptotically to atmospheric pressure. Based on these observations, various dominant phenomena that govern the temporal evolution of pressure at the sealed outlet of the Knudsen pump have been marked on top of Fig. 3.14.

The fitted model described in Section 3.2 was used to identify and quantify various non-idealities that affect the performance of a nanoporous ceramic based Knudsen pump. For a corrected volume V_{crr} of 2.8 cm^3, the numerically modeled pressure profile P_{Hm} could reproduce the experimentally observed pressure profile P_{He} with a root mean square error (RMSE) of <150 Pa.

Given the earlier characterization of the leakage aperture per unit area in the zeolite samples, it is expected that the leakage apertures, D_L, for a typical zeolite disc of 48 mm diameter is 21.1-27.8 μm. In comparison, the fitted value of D_L, as determined from the semi-analytical simulation model – see Fig. 3.14, P_{Hm} – is ≈37.5 μm while heating, and

≈31.6 μm while cooling. The difference in the leak apertures during heating and during cooling is attributed to the difference in the hydraulic path followed by gas molecules in these cases. For example, the leakage path may have different hydraulic diameters at the hot and the cold facets of the ceramics. This may result in different hydraulic resistances offered to the air molecules moving in the two directions – hot chamber to cold chamber and cold chamber to hot chamber. The pressure transient when the pump turns on is adequately captured by the fitted parameter f_{air}. The fitted model suggests that $f_{air} = 2.25$ while heating and 1 while cooling. Figure 3.14 illustrates the delay between the temperature rise of heater T_{He} (or the ceramic surface T_{Hm}) and heating up of air T_{Ha}. T_{Cm} plots the corrected temperature at the cold facet of the zeoltie disc after accounting for the parasitic heating at various interfaces. The analysis suggests that the fitted value κ is on the order of 0.005 K/s for the case when heater is on and κ is 0.01 K/s when the heater is turned off.

3.4 Discussion and Summary

This chapter has evaluated the use of naturally occurring zeolite for thermal transpiration driven gas pumping. Isothermal pressure driven flow characteristics show that the experimentally measured flow resistance, variation in applied pressure head that would result in unity change of (isothermal) pressure driven gas flow across the ceramic, is higher than the ideal flow resistance. This suggests that, the nanoporous ceramic disc has shunt paths, i.e., leakage paths, which contribute to the reduction in the hydraulic resistance of these ceramic discs. Note that this technique provides an average estimate of the flow resistance of the bulk nanoporous material. Tortuosity in the narrow channels

will result in higher flow resistance, and leakage paths will reduce the effective flow resistance.

Although the temperature rise at the cold end of the nanoporous ceramic is nominal (≈17 K), limiting the cold end temperature to even lower values may allow lower average operating temperature for the devices. Further, there is a possibility that lower cold end temperatures may limit the parasitic heating of some of the interfaces, which will help in improving the performance of the Knudsen pumps. The parasitic heating at various interfaces of the device is addressed in the subsequent chapters by replacing the PVC at the cold facet of the ceramic with a thermally conducting element.

Thermal contact resistance plays an important role in determining the performance of a Knudsen pump. Thermal contact resistances at various interfaces might result in undesirable loss in temperature bias at these interfaces. Thus, the temperature reading observed experimentally from thermocouple could be significantly different from what actually exists across the nanoporous material. Lack of planarity of the zeolite-aluminum interface and surface asperities due to conventional machining processes may result in significant thermal contact resistance.

The fitted model adequately captures the transient pressure response in the sealed hot chamber with the help of four fitted parameters. The four fitted parameters are: (i) leak aperture diameter in the zeolite disc (D_L); (ii) factor by which the thermal time constant of air exceeds the thermal time constant of the heater (f_{air}); (iii) rate of parasitic heating of the cold facet of the zeolite disc (κ); and (iv) corrected volume of air in the hot chamber (V_{crr}). These fitted parameters quantify various non-idealities in the system that cannot be measured directly due to various limitations.

In conclusion, it is evident that a zeolite-based Knudsen pump using naturally occurring nanoporous clinoptilolite (and potentially other bulk nanoporous materials as well) can be built for atmospheric pressure operation. Having no moving parts, it offers the promise of high reliability. The architecture of the Knudsen pump presented here can be potentially extended to serial or parallel multistage pumping. Idealized analysis suggests that a suitable combination of series/parallel multistage pumping configurations can potentially result in gas flow rates of 0.005-0.02 sccm/cm^2 of zeolite disc, or gas pumping pressure on the order of 50 kPa, for power density levels of roughly 1 W/cm^2.

CHAPTER 4

NANOPOROUS CERAMIC-BASED MULTISTAGE KNUDSEN PUMP

The zeolite based Knudsen pump discussed in Chapter 3 results in a gas flow rate of 0.12 sccm and a pressure head of about 1 kPa with a single stage architecture using a pumping area of 3.77 cm^2 and input power of 5.35 W. Its performance was limited by microstructural defects, grain/crystal boundaries that cause leakage and allow backflow in naturally occurring zeolites. This chapter evaluates the possibility of replacing Clinoptilolite by three possible candidates all of which are synthetic nanoporous ceramics[3]. These ceramics include:

(a) A 15 bar nanoporous ceramic (denoted 15PC) – clay based nanoporous ceramic from Soil Moisture Corp. with air entry value of 15 bar. The air entry value is the pressure at which air will break through a wetted pore channel.

(b) A 5 bar nanoporous ceramic (denoted 05PC) – clay based nanoporous ceramic from Soil Moisture Corp. with air entry value of 5 bar.

(c) A porous glass VYCOR (denoted VYPG) from Corning Inc.

Single stage Knudsen pumps (SSKP) based on these three ceramics are fabricated and tested for pressure and flow characteristics. The performance metrics of these three pumps are compared with that of a similar single stage Knudsen pump based on

[3] Portions of this chapter have appeared in conference abstract form in [Gup09]

clinoptilolite (denoted ZEO). Subsequently, the most preferred ceramic is chosen for a multistage Knudsen pump (MSKP). Finally, the performance characteristics of a 9 stage Knudsen pump based on the most preferred ceramics are reported. It is shown that a pumping pressure head in excess of 12 kPa can be generated, which is better aligned with the needs of various microfluidic systems such as polymerase chain reaction (PCR), electrophoresis, cell sorting, cell culture etc. [Ung00, Sia03]. Section 4.1 describes the device structure, Section 4.2 describes the fitted model used to model the system level performance of the device, test set-ups and experimental results are presented in Section 4.3 and finally notable observations have been discussed in Section 4.4.

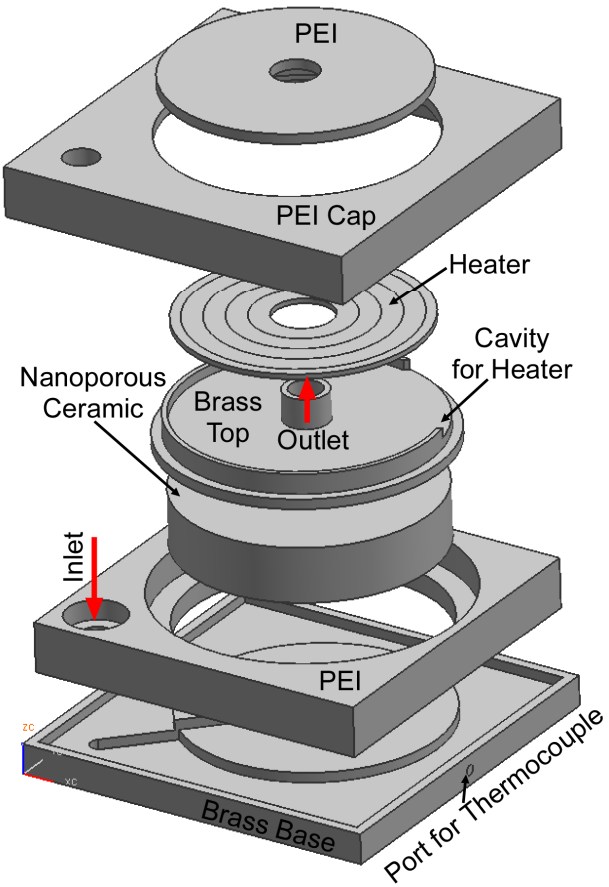

Fig. 4.1: Exploded view of a single stage Knudsen pump showing relative location of various components.

4.1 Device Structure

Figure 4.1 shows an exploded view of SSKP discussed in this chapter. A nanoporous ceramic disc is bonded peripherally to a thermally insulating polyetherimide (PEI) substrate using a vacuum grade epoxy (STYCAST 2850FT/Catalyst 9). A thermally insulating substrate allows higher temperature gradient across the thickness of the ceramic disc for a given input power, which results in higher thermal efficiency. A brass

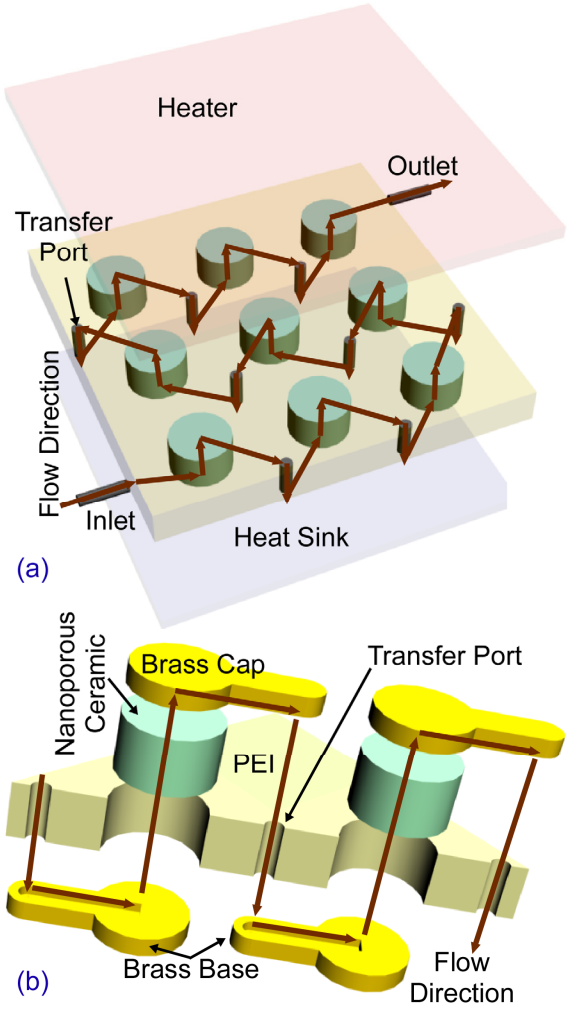

Fig. 4.2: Planar architecture for the multistage Knudsen pump (MSKP): a) Planar array of 9 single stage Knudsen pumps encapsulated in a polyetherimide substrate; the arrows mark the direction of flow of the gas molecules from one stage to another; b) Exploded view of two successive stages of the pump; the arrows show the direction of flow through different elements.

base ensures effective thermal contact of the bottom facet of the ceramic to an external heat sink. The top facet of the ceramic is in thermal contact with a heater through a brass top. The brass top has a cavity, which holds a heater (≈26.5 Ω). The heater has a thin, etched-foil resistive element laminated between two insulating layers of Kapton (Minco, MN). Finally, a PEI cap and a PEI top are used to hold all the components in place and seal the device from above. The PEI cap and the brass base are bonded to the PEI substrate resulting in two sealed chambers, a hot one and a cold one, on either side of the ceramic disc. The use of thermally insulating PEI cap ensures effective thermal isolation between the top and the bottom surfaces of the ceramic. This particular architecture allows the heater to be located outside the hot chamber of the device, which minimizes the possibility of leakage. Stainless steel capillaries are used to provide inlet and outlet ports from the bottom and the top surfaces of the nanoporous ceramic respectively. Conventional machining techniques are used to fabricate the brass and PEI components, while the nanoporous ceramics are machined using diamond tools.

The basic architecture for the MSKP is derived from the SSKP discussed above. The 9-stage Knudsen pump has stages arranged in a 3x3 planar array (Fig. 4.2). The planar architecture allows a common heater and a common heat sink, which helps with overall thermal efficiency of the device. As in the SSKP, the MSKP uses a PEI substrate to achieve thermal efficiency. The PEI substrate is patterned with 9 cavities that house the transpiration elements, and 9 vertical transfer ports that serve to serially connect the outlet of one stage to the inlet of next stage. The nanoporous ceramic discs are bonded peripherally into the cavities in the PEI substrate. Brass caps with embedded microgroove channels seal each porous ceramic disc from above and below, and direct

the gas flow laterally – into/out of each stage through the vertical transfer ports. The caps also ensure good thermal contact of the ceramic discs with the heater and the heat sink.

Figure 4.3 shows the final assembled SSKP, it uses nanoporous ceramic disc with diameter ≈12.75 mm and thickness ≈2.75 mm. The final packaged volume of the SSKP

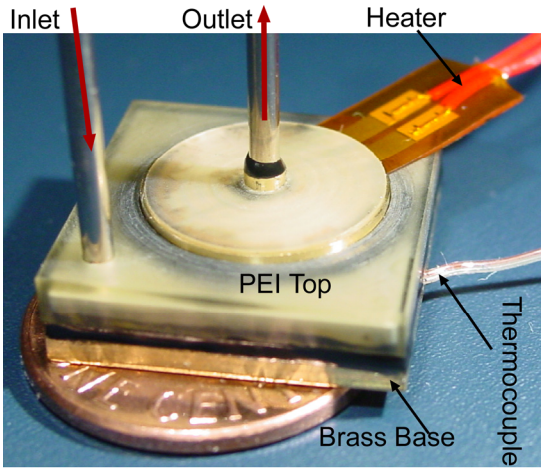

Fig. 4.3: Photograph of the final packaged single stage Knudsen pump.

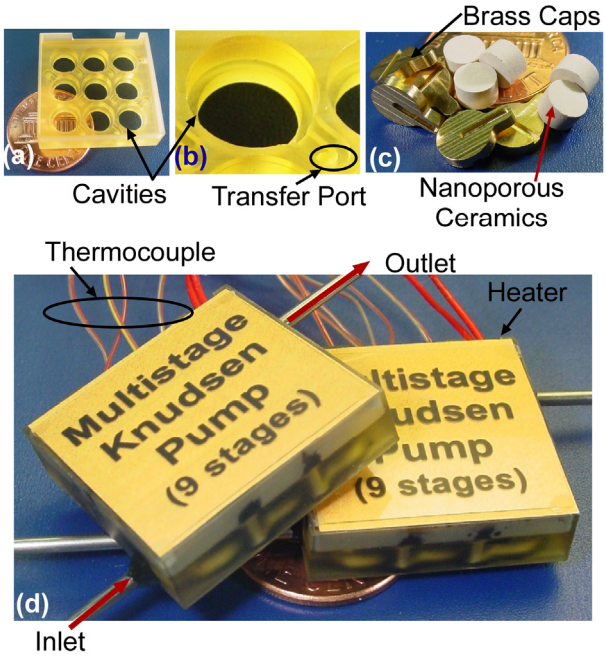

Fig. 4.4: Photographs of various components used in the multistage Knudsen pump and the final packaged multistage Knudsen pump. These pictures are of: a) Patterned polyetherimide; b) enlarged view of a single cavity; c) other components used in the pump; and (d) final packaged multistage Knudsen pump.

is 18x18x6.5 mm^3.

Figure 4.4a-c shows various components used in the MSKP. The nanoporous ceramic discs are ≈5 mm in diameter and ≈2.85 mm thick. The vertical transfer ports are 1 mm in diameter. The final packaged volume of the MSKP, shown in Figure 4.4d, is 25x25x7.25 mm^3.

4.2 Fitted Model

The fitted model presented here resembles closely the model presented in Chapter 3, albeit with adjustment in some of the fitting parameters.

The first fitted parameter f_{air} is replaced by τ_a. Note that in the fitted model presented in Chapter 3, the fitted parameter f_{air} was used to calculate τ_a. In contrast, the fitted model presented in this chapter uses τ_a as a fitted parameter.

The second fitted parameter, effective leak aperture diameter (D_L), remains same as in the model discussed in Chapter 3. However, in order to compare the leak aperture sizes in the transpiration element of different sizes, a parameter leak aperture diameter per unit area of the transpiration material d_L is used, as defined in Chapter 3 (Eqn. 3.12).

For the third fitted parameter, instead of assuming continuous (parasitic) heating of the cold facet of the ceramic, the model uses a fitted parameter f. It is defined as the fraction of the experimentally measured temperature bias that actually appears across the nanoporous ceramic. The experimentally measured temperature bias is recorded across the top and the bottom brass caps. However, the actual temperature drop that appears across the thickness of the ceramic disc is smaller than the experimentally measured value due to the thermal contact resistances at the top and the bottom facets of the

ceramic. The model assumes that the (overall) loss in temperature bias due to the thermal contact resistances appears at the top facet of the ceramic disc.

The fourth fitted parameter is the corrected volume of the hot chamber V_{crr} – this is same as in Chapter 3.

As in Chapter 3, the flow and the pressure measurements in this chapter are also at the outlet. So, the variation in the pressure profile will be identical to the pressure profile shown in Fig. 3.7. Hence, the approach for fitted model remains identical to the

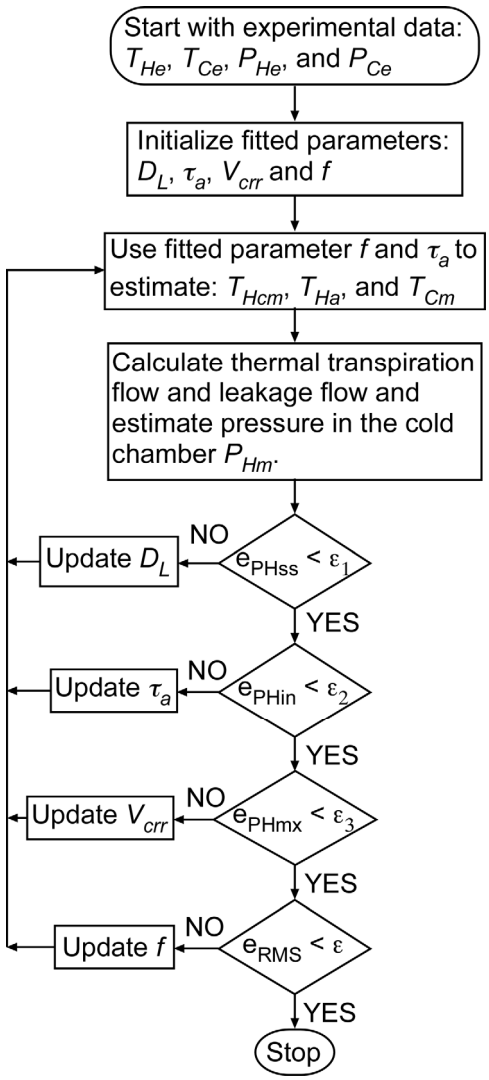

Fig. 4.5: The flowchart for key steps involved in the fitted model.

description in Chapter 3, except the fitted parameter τ_a is used instead of f_{air} and the fitted parameter f is used instead of κ.

Figure 4.5 shows the flowchart for the fitted model and a detailed step-by-step algorithm for the fitted model is presented below:

Step 1: Choose a suitably small time step (Δt) and interpolate $T_{He}(t)$, $T_{Ce}(t)$ and $P_{He}(t)$ for all the time steps.

Step 2: Choose initial value for V_{crr}, D_L, τ_a, and f. Due to the asymmetric nature of the problem, these parameters may have different values, while the heater is on and while it is off.

Step 3: Estimate the initial number of moles of air in the hot chamber based on the initial temperature, pressure of the device and the corrected volume of the hot chamber.

$$N(0) = \frac{P_{He}(0).V_{crr}}{R.T_{He}(0)} \tag{4.1}$$

Step 4: Evaluate the temperature at the hot end of the ceramic at time t.

$$T_{Hm}(t) = T_{in} + f.(T_{He}(t) - T_{in}) \tag{4.2}$$

Step 5: The steady state temperature of the hot end of the ceramic when the heater is on is given by $T_{in} + f.(T_{fin} - T_{in})$, where T_{in} is the steady state temperature of the heater in its off state and T_{fin} is its steady state temperature in on state. The air in the hot chamber is assumed to attain the same steady state temperature as the hot facet of the ceramic, but with a longer time constant τ_a. Use τ_a to estimate the temperature of the air in the hot chamber $T_{Ha}(t)$ at a given time t. Assume, $T_{Cm}(t) = T_{Ce}(t)$.

$$T_{Ha}(t) = T_{in} + f.(T_{fin} - T_{in}).(1 - e^{-t/\tau_a}) \tag{4.3}$$

Step 6: The transient evolutions of pressure at every time step has been addressed as combination of two independent sub-steps. First sub-step – for any change in heater temperature during the time interval t to $t+\Delta t$, ideal gas law is used to estimate the intermediate pseudo-equilibrium pressure $P_{Hi}(t+\Delta t)$.

$$P_{Hi}(t+\Delta t) = \frac{P_{Hm}(t)}{T_{Ha}(t)} T_{Ha}(t+\Delta t) \tag{4.4}$$

Step 7: Second sub-step – average values for T_{Ha}, T_{Cm} and P_{Hi} are used to estimate the thermal transpiration gas flow and the Poiseuille (leakage) flow during the time t to $t+\Delta t$.

$$\overline{P}_{Hi}(t+\Delta t) = \frac{P_{Hi}(t+\Delta t) + P_{Hm}(t)}{2} \tag{4.5}$$

$$\overline{T}_{Hm}(t+\Delta t) = \frac{T_{Hm}(t+\Delta t) + T_{Hm}(t)}{2} \tag{4.6}$$

$$\overline{T}_{Cm}(t+\Delta t) = \frac{T_{Cm}(t+\Delta t) + T_{Cm}(t)}{2} \tag{4.7}$$

Step 8: Substitute for $T_H = \overline{T}_{Hm}(t+\Delta t)$; $T_C = \overline{T}_{Cm}(t+\Delta t)$; $P_H = \overline{P}_{Hi}(t+\Delta t)$ and $P_C = P_{amb}$ in Equation 2.15 to calculate the thermal transpiration driven mass flow rate and divide it by the molecular mass M of air to estimate the number of moles of gas molecules $N_{TT}(t+\Delta t)$ pumped into the hot chamber.

Step 9: Substitute $P_H = \overline{P}_{Hi}(t+\Delta t)$ and $P_C = P_{amb}$ in Equation 2.19 to calculate the leakage flow, multiply it with the density of air (Eqn. 2.7), and divide it by the molecular mass M of air to estimate the effective number of molecules $N_{POS}(t+\Delta t)$ leaking in/out of the hot chamber.

Step 10: The effective number of moles of gas in the hot chamber after time $t+\Delta t$ is calculated by accounting for the gas molecules moving in and out of chamber due to the thermal transpiration flow and Poiseuille flow.

$$N(t+\Delta t) = N(t) + N_{TT}(t+\Delta t) - N_{POS}(t+\Delta t) \tag{4.8}$$

Step 11: Estimate the final pressure in the chamber

$$P_{Hm}(t+\Delta t) = \frac{P_{Hi}(t+\Delta t)}{N(t)} N(t+\Delta t) \tag{4.9}$$

Step 12: Increment time, i.e. $t = t+\Delta t$; and repeat steps 4 to 11 for all the time steps.

Step 13: Update D_L repeat steps 4 to 12 until e_{PHss} is smaller than ε_1, where ε_1 is the acceptable tolerance in minimizing e_{PHss}.

Step 14: Update τ_a and repeat steps from 4 to 13 until e_{PHin} is smaller than ε_2, where ε_2 is the acceptable tolerance in minimizing e_{PHin}.

Step 15: Update V_{crr} and repeat steps from 3 to 14 until e_{PHmx} is smaller than ε_3, where ε_3 is the acceptable tolerance in minimizing e_{PHmx}.

Step 16: Update f and repeat steps from 3 to 15 such that e_{RMS} is smaller than ε, where ε is the acceptable tolerance in minimizing e_{RMS}.

Thus, the fitted model gives an estimate for the fitted parameters V_{crr}, D_L, τ_a, and f, such that the RMS error between the experimentally measured and modeled pressure in the hot chamber is minimized. Note than the tolerances ε_1, ε_2, ε_3, and ε may vary from one iteration to the next.

4.3 Experimental Results

4.3.1 Characterization of Nanoporous Ceramics

15PC, 05PC and VYPG have a bulk porosity of 32%, 31%, and 28%, respectively. While these are commercially available ceramics with known bulk porosity (f_p); however, no reliable data for the pore size distribution is available. In contrast, clinoptilolite has an average pore diameter D_{NP} ($=2a$) of 0.45 nm and bulk porosity f_p of 34% [Li05]. However, the porosity data is not reliable because the naturally occurring zeolite samples may have impurities that block the nanopores. In addition to the structural parameters a and f_p, a complete analysis of the gas flow across a nanoporous ceramic requires the knowledge of the leak aperture D_L in the nanoporous disc.

This section summarizes a technique that uses experimental results and one of the (known) structural parameters (a or f_P) to estimate the other two (unknown) structural parameters. It requires two sets of experimental results: (a) The experimentally measured isothermal pressure driven gas flow characteristic of a ceramic, typical variation shown in

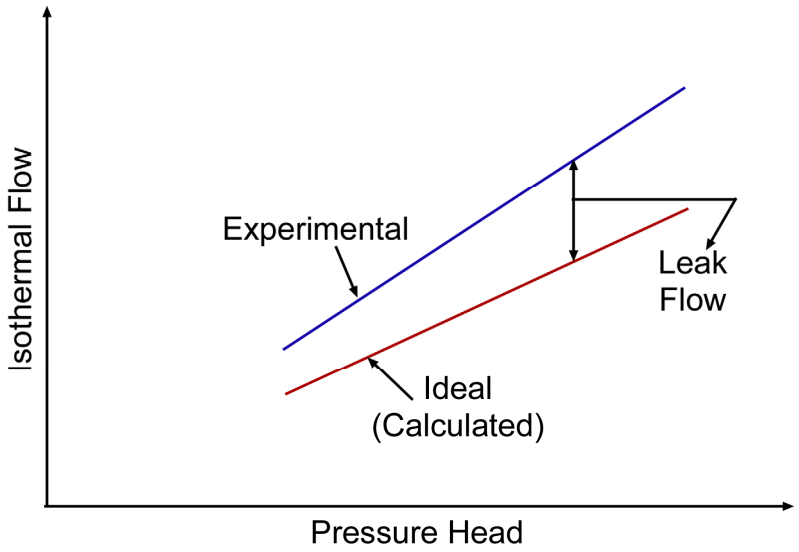

Fig. 4.6: A typical variation in the isothermal pressure driven gas flow generated across a ceramic with the externally applied pressure head.

Fig. 4.6; and (b) The experimentally measured variation in the gas flow generated by a single stage Knudsen pump based on that ceramic, typical variation shown in Fig. 4.7.

Gas flow rate versus pressure head characteristic of a SSKP is extrapolated to estimate the gas flow Q_{mxE} that the pumps can generate with zero pressure head at its outlet (Fig. 4.7). The flow characteristic also suggests the maximum pressure head P_{mxE} generated by the pump. Since, zero pressure head operation of a Knudsen pump implies no leakage flow, Q_{mxE} will have no contribution from leakage flow. Hence, Q_{mxE} is the thermal transpiration driven gas flow across the ceramic. Knowing Q_{mxE} and one of the structural parameters, a or f_p, the first step is to use Eqn. 2.15 to get an initial estimate of the second (unknown) structural parameter (f_p or a). In the second step, parameters a and f_P are used to calculate the ideal isothermal flow expected across the ceramic (shown in Fig. 4.6). The difference between the experimentally measured and the ideal flows shown in Fig.

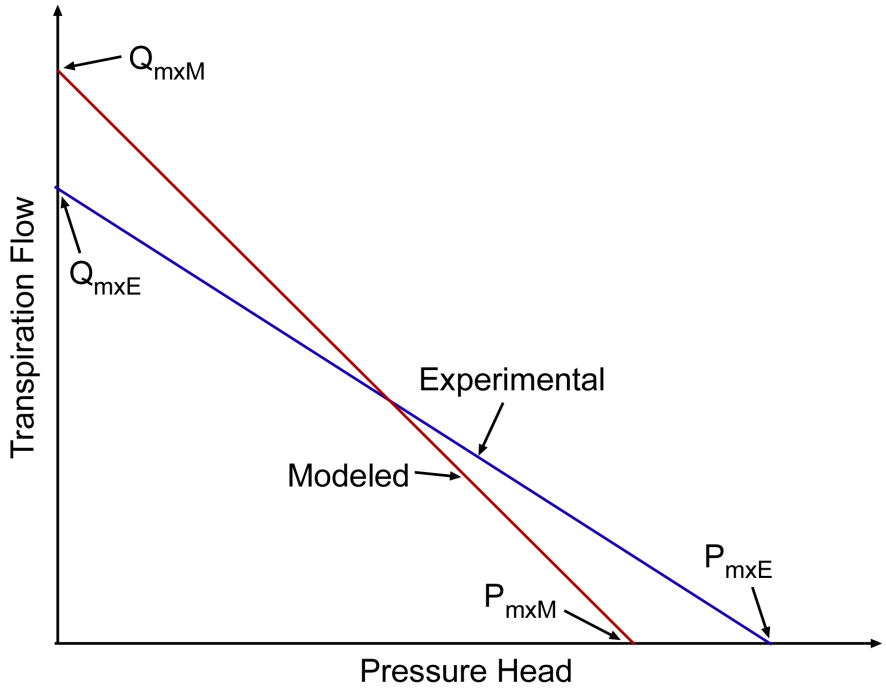

Fig. 4.7: A typical variation in the thermal transpiration driven gas flow rate generated across a Knudsen pump with pressure head at its outlet (or inlet).

4.6 gives an estimate of D_L (Eqn. 2.19). In the third step, a, D_L and f_p are used to estimate modeled variation in the thermal transpiration driven gas flow generated by the Knudsen pump (shown in Fig. 4.7). This modeled flow characteristic gives an estimate of the maximum pressure head, P_{mxM}, and maximum flow rate, Q_{mxM}, expected from the device for a given set of parameters – a, f_P and D_L. Steps 1-3 described above are iterated and the unknown parameter, a or f_p, is fine-tuned further such that:

$$\left\| \frac{Q_{mxE} - Q_{mxM}}{Q_{mxE}} \right\| \approx \left\| \frac{P_{mxE} - P_{mxM}}{P_{mxE}} \right\| \tag{4.10}$$

Each iteration yields a corresponding value for D_L. The parameters Q_{mxM} and P_{mxM} may deviate significantly from Q_{mxE} and P_{mxE} respectively because Q_{mxM} and P_{mxM} do not account for all the non-idealities present in the system (as noted in Section 4.2).

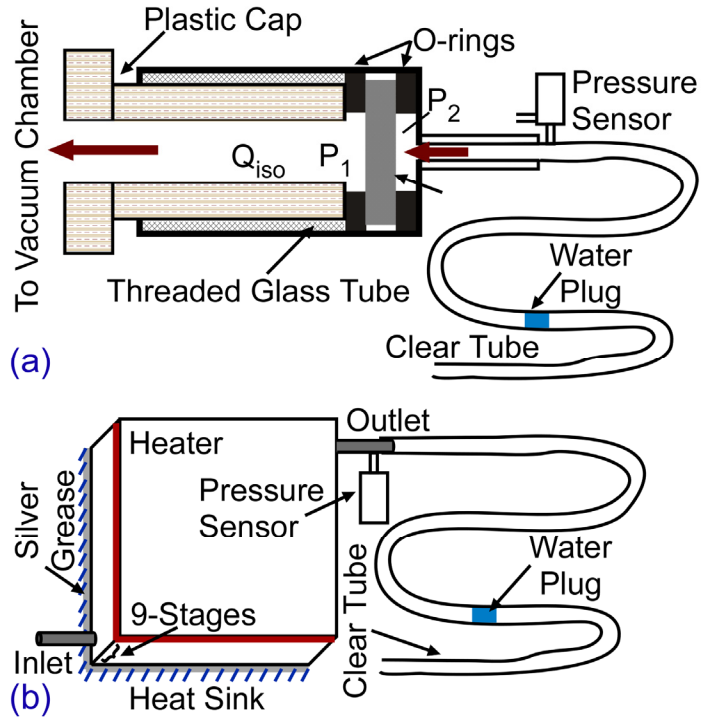

Fig. 4.8: Test set-ups for: (a) Isothermal pressure driven gas flow characterization of nanoporous ceramics; and (b) Thermal transpiration driven gas flow characterization of a Knudsen pump.

4.3.2 Test Set-Up

Two different experimental set-ups were used for this chapter. As in chapter 3, the first set-up was for isothermal pressure driven gas flow characterization of the nanoporous ceramic discs (Fig. 4.8a). A 25 mm diameter disc of nanoporous ceramic sample was sandwiched between a threaded glass tube and its plastic cap. "O"-rings were used to seal the ceramic disc between the glass tube and the plastic cap. The plastic cap was connected to a vacuum chamber, which was used to apply a (externally) controlled pressure differential across the nanoporous ceramic. The other end of the glass tube was connected to a clear Tygon tubing with a water plug to visualize and quantify the gas flow across the ceramic disc.

The second test set-up that was used to study the performance characteristics of the Knudsen pumps (Fig. 4.8b). The bottom facet of the device under test was attached to a heat sink – a metallic block with large thermal mass maintained at room temperature. Silver grease was used for effective thermal coupling of the Knudsen pump with the heat sink. As in Chapter 3, the device was tested in two different operation modes: pressure mode and flow mode. While operating in pressure mode, the outlet was sealed, a pressure sensor (Model# MPXM2053D by Freescale Semiconductor) was attached at the sealed outlet, and the inlet was open to the ambient. This mode was used to quantify the maximum limiting pressure head against which the device could pump gas. While operating in flow mode, flexible tubing (ID 0.79 mm) for water plugs, and a pressure sensor with water plugs, and a pressure sensor were connected to the outlet of the pump through a T-joint; the inlet was open to ambient. This mode was used to characterize the variation, with applied pressure head, in the air flow generated by the pump at the outlet

for different input power levels. Thermocouples, attached to the brass top and the brass base, were used to record the applied temperature bias across the nanoporous ceramic. The voltage output from the two thermocouples and the pressure sensor were read into HP34401A multimeters, which was connected to a PC running a Labview™ program, through a National Instruments GPIB-USB-HS data transfer cable to record the temporal variation of the voltage outputs.

4.3.3 Steady State Characterization

A. Isothermal Poiseuille Gas Flow

Figure 4.9 illustrates the isothermal pressure driven gas flow characteristics across ≈25 mm diameter and ≈2.7 mm thick nanoporous discs. The rate of variation of the gas flow rate across the ceramic disc with the externally applied pressure head was used to

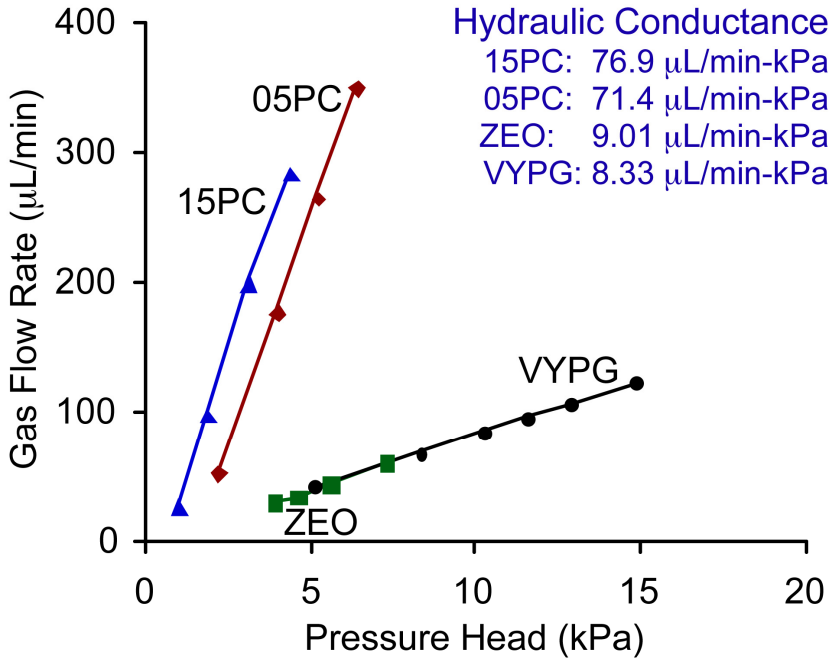

Fig. 4.9: Isothermal pressure driven gas flow characteristics of various nanoporous ceramic discs. Variation in the experimentally measured isothermal pressure driven gas flow rates across 25 mm diameter and ≈2.7 mm thick nanoporous ceramic discs with externally applied pressure head were used to estimate their hydraulic conductance.

estimate the hydraulic conductance of these ceramic discs. Experiments suggested that 15PC has highest conductance (≈76.9 μL/min-kPa) followed closely by 05PC (≈71.4 μL/min-kPa). ZEO and VYPG were observed to have about an order of magnitude lower hydraulic conductance (≈9 μL/min-kPa) than 15PC and 05PC.

The experimentally measured isothermal pressure driven gas flow has two components: (i) pressure driven transpiration flow through the nanopores (Eqn. 2.15); and (ii) leakage (Poiseuille) flow through the leak apertures (Eqn. 2.19). For a perfect (ideal) nanoporous ceramics, that is, ceramic with no structural imperfections, there is no leakage flow and the expected idealized gas flow rate is given by Eqn. 2.15. The deviation of the experimentally measured gas flow from the ideal case gives an estimate of D_L for the bulk nanoporous ceramic discs. A detailed procedure to calculate (unknown) structural parameters of the bulk nanoporous materials has been discussed in Section 4.3.1.

B. Thermal Transpiration – SSKP

Figure 4.10 shows the relative performance of SSKPs based on various nanoporous ceramics. While operating in pressure mode, 15PC-, 05PC-, and ZEO-SSKP resulted in almost identical pressure ratios, P_H/P_C, for a given temperature ratio, T_H/T_C (Fig. 4.10a). However, the VYPG-SSKP resulted in a significantly higher pressure ratio than the 15PC, 05PC and ZEO SSKP(s). The plot also identifies the idealized limit for the performance of a Knudsen pump. Idealized limit corresponds to the case for which (a) the nanoporous ceramics has no structural defects; (b) there exists no thermal contact

resistance at the interface between the ceramic disc and the brass elements; and (c) the ceramic disc have uniform in-plane temperature.

Flow mode testing of these single stage pumps suggested that the maximum pressure head (P_{mxE}) generated by VYPG-SSKP was ≈2x greater than that of any other SSKP. However, under similar operating conditions VYPG-SSKG had ≈5x smaller no load gas flow generation capabilities (Q_{mxE}) as compared to the best performing 15PC-SSKP (Fig. 4.10b). The gas flow generated by each of these pumps decreased linearly with

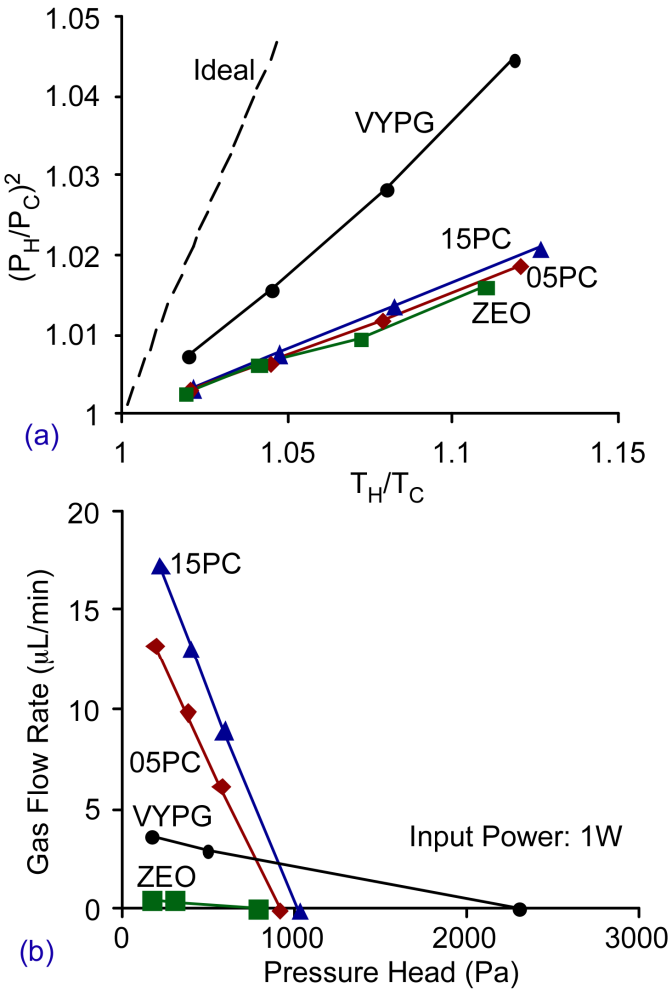

Fig. 4.10: Performance characteristics of single stage Knudsen pumps (SSKPs) based on various nanoporous ceramics: 15 bar nanoporous ceramic (15PC), 5 bar nanoporous ceramic (05PC), VYCOR nanoporous glass (VYPG), and zeolite (ZEO). (a) Variation in square of pressure ratio P_H/P_C with applied temperature ratio T_H/T_C for single stage Knudsen pumps. (b) The gas flow rate generated by single stage pumps, based on each of these ceramics, for different applied pressure head at the outlet.

increasing pressure head at the outlet.

As described in Section 4.3.1, the flow characteristics illustrated in Figure 4.9 and 4.10b were used to estimate the unknown structural parameters of the nanoporous ceramics. Table 4.1 summarizes the average value for the three structural parameters for the ceramics. Note that the parameter values in bold were already known, while the remaining parameter were estimated based on the procedure discussed in Section 4.3.1.

C. Thermal Transpiration – MSKP

Based on the SSKP performance, ceramic 15PC was identified as the preferred material for the MSKP. A 15PC-MSKP operating in pressure mode resulted in a maximum pressure head of ≈12 kPa for a temperature gradient of ≈16.5 K/mm across the nanoporous ceramics (Fig. 4.11). The pressure head at the sealed outlet was directly proportional to the temperature gradient applied across the nanoporous ceramics, which, in-turn, was linearly dependent on the input power density to the device.

The variation in the gas flow rate generated by 15PC-MSKP was observed to decrease linearly with the applied pressure head at its outlet (Fig. 4.12). The flow also scaled down linearly with the applied power density to the device. A sustained temperature gradient of ≈16.5 K/mm across the 15PC ceramic discs in a MSKP required an input

Table 4.1: Summary of nanopore diameter D_{NP}, bulk porosity f_p, and leak aperture diameter d_L of various nanoporous ceramics.

Material	**Nanopore Diameter**	**Percent Porosity**	**Leak Aperture**
Units	nm	%	μm/cm^2
Symbol	D_{NP} (=2.a)	f_p	d_L
15PC	$1.23^{-0.26}_{+0.66}$	**32**	21.1 – 22.5
05PC	$1.08^{-0.22}_{+0.52}$	**31**	21.0 – 22.2
ZEO	**0.45**	$5.2^{-1.8}_{+4.7}$	14.4 – 14.9
VYPG	$0.47^{-0.02}_{+0.01}$	**28**	13.5 – 13.7

power density of 525 mW/cm^2. While operating in flow mode, a temperature gradient of 16.5 K/mm resulted in a maximum gas flow rate of ≈3.7 µL/min against a pressure head of ≈160 Pa.

Fluid manipulation capability of 15PC-MSKP for potential application to droplet manipulation in microfluidic assays is shown in Fig. 4.13. For an input power density of 525 mW/cm^2, the device could maneuver a water droplet plug through a 250 µm ID fluorinated ethylene propylene (FEP) tubing, connected at its outlet, at speeds in excess of 1.2 mm/sec. The plot suggests that the droplet speed is directly proportional to the input power to the device.

In order to test the reliability of ceramic based Knudsen pumps, the MSKP is being operated continuously in flow mode for extensive periods. To date, it has operated

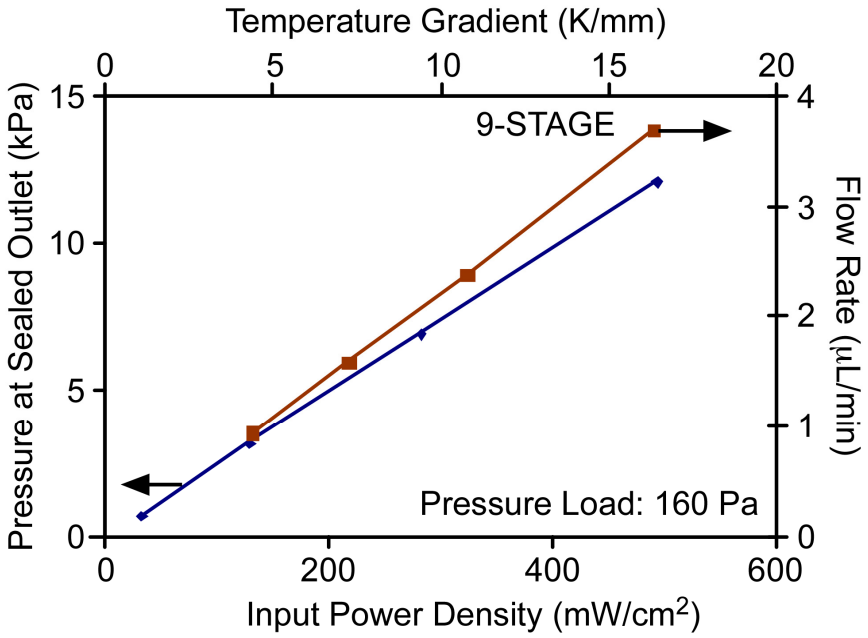

Fig. 4.11: Steady state performance characteristics of a 15PC 9-stage Knudsen pump. The maximum pressure generated at sealed outlet increases linearly with the input power density to the device. Similarly, the gas flow rate measured at the outlet against a pressure head of ≈160 Pa increases linearly with the input power. Top axis indicates the temperature gradient across the thickness of the nanoporous ceramic corresponding to various input power densities to the device.

continuously for more than 7000 hours without any deterioration in its performance (Fig. 4.14). For an input power of 1.9 W, the average gas flow generated by MSKP during this period is ≈2.2 μL/min. with a standard distribution of ≈0.04 μL/min. (This flow rate is measured against a pressure load of 150 Pa.) The variation in gas flow rate is primarily due to the variation in the ambient operating temperature of the device. Variation in ambient temperature results in fluctuation of the effective temperature gradient across the ceramic discs, which, in-turn, results in variation of the gas flow rate generated.

4.3.4 Transient Response

A. Transient Response of SSKP

Figure 4.15 shows the experimentally measured transient pressure response P_{He} of 15PC-SSKP at its sealed outlet corresponding to temperatures T_{He} and T_{Ce} (measured

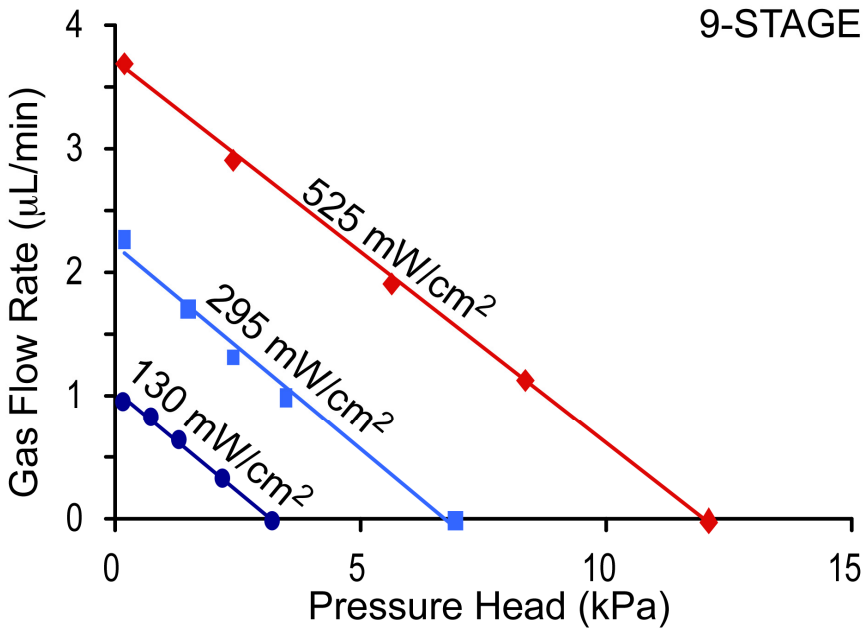

Fig. 4.12: Gas flow characteristics of 15PC 9-stage Knudsen pump. Gas flow rate generated by each of these pumps decreases linearly with increasing pressure head applied at the outlet.

experimentally) at the hot and the cold ends of the pump, respectively. The fitted model discussed in Section 4.2 was used to quantify the four fitted parameters that control the temporal evolution of pressure at the sealed outlet of the device. The device had an estimated leak aperture d_L of ≈18.8 μm/cm^2 while heating and ≈19.2 μm/cm^2 while cooling. The initial pressure transients that occured as soon as the heater was turned on (or off) were captured adequately by the fitted parameters V_{crr} and τ_a. The corrected volume of the hot chamber V_{crr} was 0.32 cc, which was 20% of the actual physical volume of the hot chamber. The time constants τ_a for heating (≈494 sec) was 5.5 times the corresponding time constant for heater, whereas τ_a (≈568 sec) was 8 times the time constant for heater during cooling. Finally, the model suggested that the loss in temperature gradient due to thermal contact resistance was about 49% (i.e. $f \approx 0.51$). Based on these fitted parameters, the modeled pressure profile P_{Hm} could reproduce the experimentally observed pressure profile P_{He} with a root mean square error (RMSE) of <30 Pa.

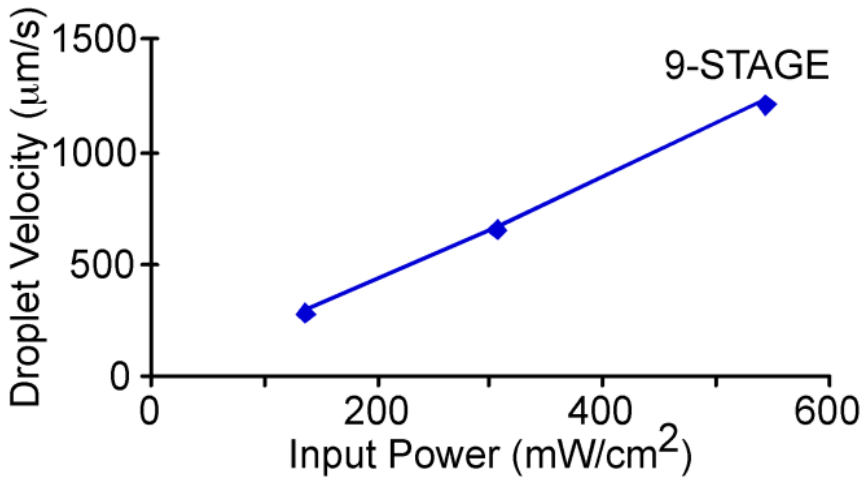

Fig. 4.13: Velocity at which the 15PC 9-stage Knudsen pump could push a water droplet through a 250 μm ID fluorinated ethylene propylene capillary for different input power densities to the device.

B. Transient Response of MSKP

Figure 4.16 shows the experimentally measured transient pressure at the sealed outlet of 15PC-MSKP, P_{He}, corresponding temperatures measured at the hot and the cold facets of the device are shown by T_{He} and T_{Ce}, respectively (Fig. 4.16). Temperatures T_{He} and T_{Ce} were measured at the top and the bottom of the 5th stage and the pressure was measured at the outlet of the 9th stage.

The fitted model for MSKP comprises of 9 interlinked fitted models, one for each of the 9 stages, such that the pressure at the outlet of one stage is reflected at the inlet of the next stage. Table 4.2 summarizes the values for various fitted parameters that adequately capture the temporal evolution of pressure at the sealed out of the device. The relative location of individual stages in MSKP with respect to the inlet (I) and outlet (O) are indicated by dark circles in the first row of Table 4.2. Based on these fitted parameters, the modeled pressure profile P_{Hm} could reproduce the experimentally observed pressure profile P_{He} with a RMS error ≈110 Pa.

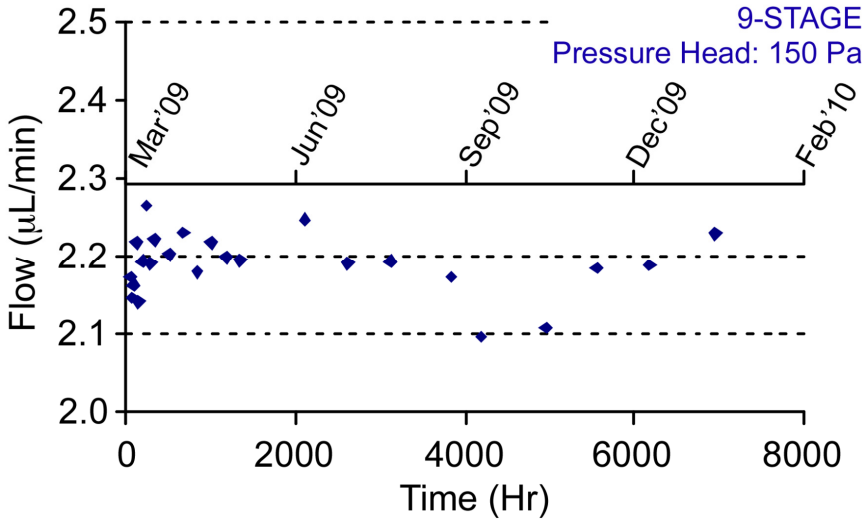

Fig. 4.14: The variation in gas flow rate with time during a continuous 7000 hours operation of the 15PC 9-stage Knudsen pump. The average gas flow rate generated during this period is 2.2 µL/min with a standard deviation of 0.04 µL/min.

4.4 Discussion

Although ceramic 15PC has the largest leak aperture, d_L (Table 4.1), it offers the best performance of the ceramic materials considered. This is so because it has the largest pore diameter D_{NP} and the highest porosity f_p, which provide significantly higher thermal transpiration driven gas flow to overcome the disadvantage due to its large d_L.

The leak aperture d_L (≈22.2 μm/cm^2) for 15PC-SSKP, as estimated from the steady

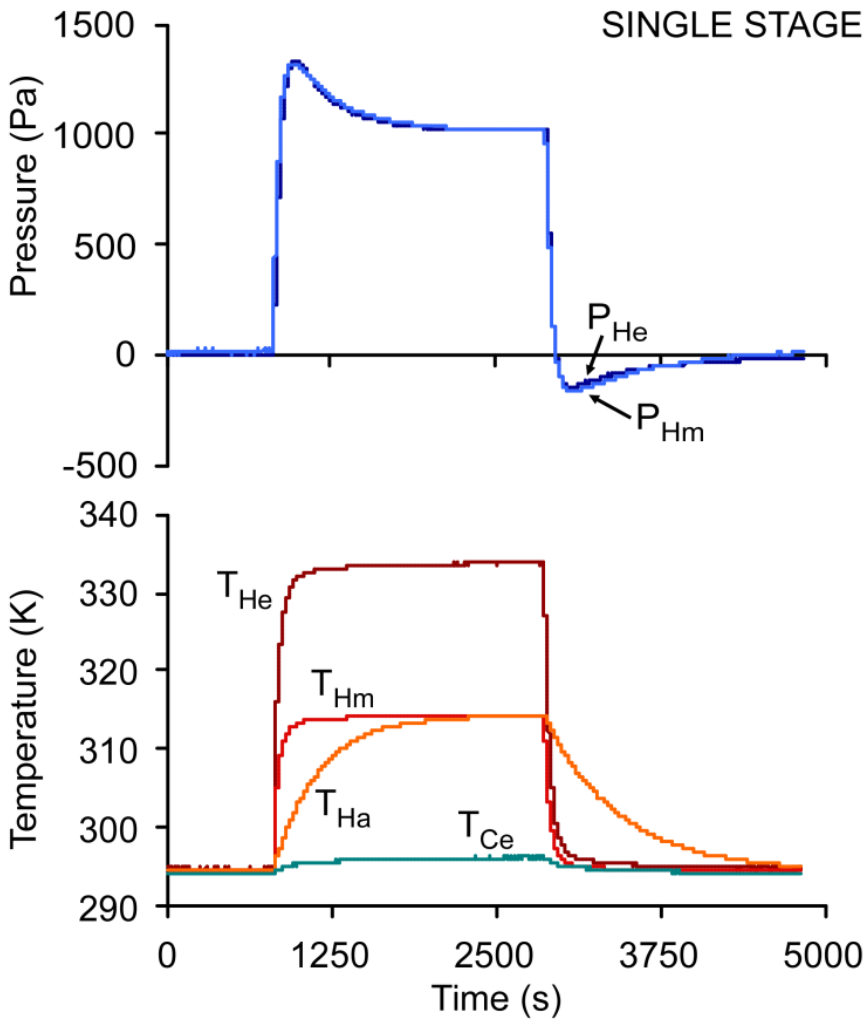

Fig. 4.15: Variation in the experimentally measured pressure P_{He} at the sealed outlet of the 15PC single stage Knudsen pump corresponding to the experimentally measured temperatures T_{He} at the hot and T_{Ce} at the cold ends of the nanoporous ceramic. T_{Hm} is the corrected temperature of the hot facet of the nanoporous ceramic, T_{Ha} is the modeled temperature of the air in the hot chamber; and P_{Hm} is the pressure at the sealed outlet – as predicted by the fitted model. The root mean square error between P_{He} and P_{Hm} <30 Pa.

state characterization, is reasonably close to the d_L (≈19 μm/cm^2) predicted by the fitted model. Similarly, the d_L (≈22 μm/cm^2) for stages 1-8 in 15PC is in good agreement with the estimate value for d_L. However, d_L for the 9th stage is larger (≈29 μm/cm^2) than the remaining stages, potentially because of additional leakage across various joints/fitting at the outlet of the device.

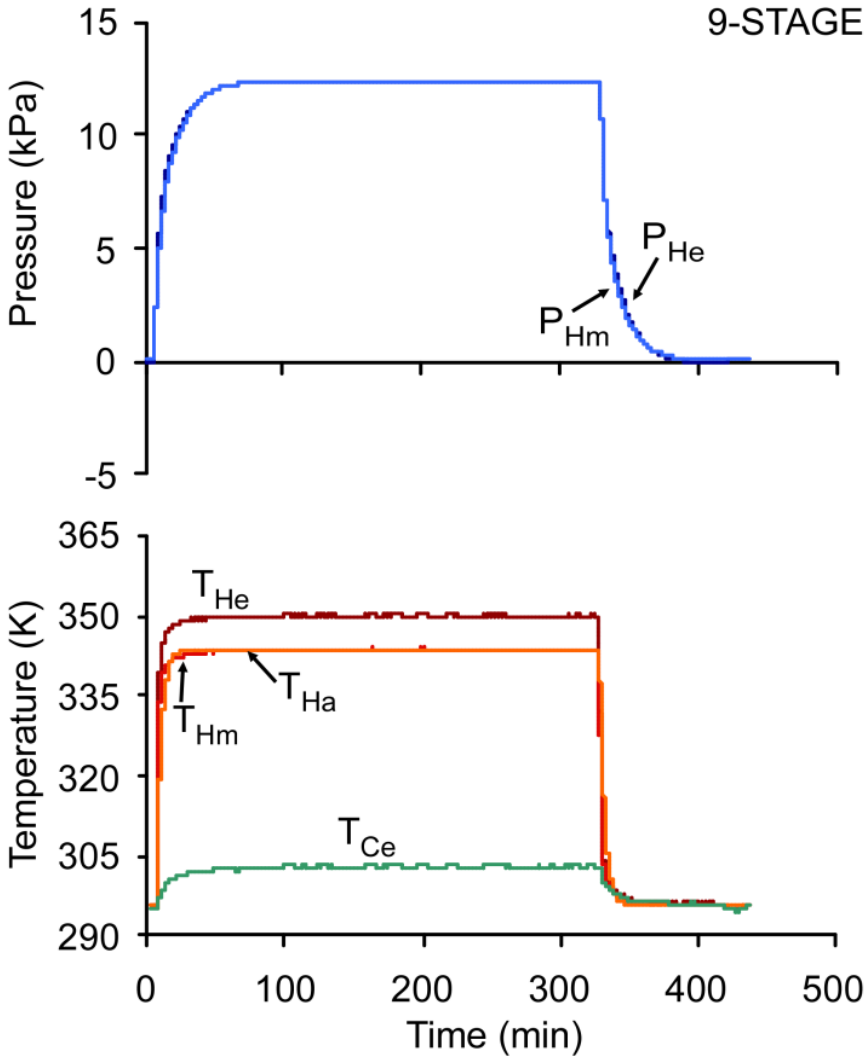

Fig. 4.16: Variation in the experimentally measured pressure P_{He} at the sealed outlet of the 15PC 9-stage Knudsen pump corresponding to the experimentally measured temperatures T_{He} at the hot and T_{Ce} at the cold ends of the nanoporous ceramic. T_{Hm} is the modeled temperature of the hot facet of the nanoporous ceramic, T_{Ha} is the corrected temperature of the air in the hot chamber; and P_{Hm} is the corresponding pressure at the sealed outlet – as predicted by the fitted model. The root mean square error between P_{He} and P_{Hm} <110 Pa.

Based on the experimental characterization of various ceramics, 15PC has been identified as a favorable ceramic for multistage Knudsen pumping. Although VYPG-SSKP results in about 2 times greater pressure head than 15PC-SSKP, the maximum gas flow rate generated by 15PC-SSKP is more than 5 times greater than the maximum gas flow rate generated by VYPG-SSKP (Fig. 4.10b). Hence, 15PC is a better thermal transpiration material than VYPG.

The fitted model for 15PC-SSKP suggests that only 20% of the actual physical volume of the hot chamber contributes to V_{crr} (≈0.32 cm^3). However, the contribution reduces to 17% for 15PC-MSKP, potentially because the footprint of individual stage in MSKP is significantly smaller than the footprint of SSKP. Hence, the volume of air closer to heater is significantly less in MSKP than in SSKP. In contrast, for stages 1-8 in the MSKP, 85% of the actual physical volume of the hot chamber constitutes V_{crr}. This high percentage for V_{crr} in stages 1-8 is probably because the hot chambers for stages 1-8 are comprised primarily of the vertical transfer ports that serve to connect subsequent stages. These transfer ports are embedded in the PEI substrate and are sealed at ends with brass caps. They fall directly underneath the heater. Hence, a significant portion of the air entrapped in these hot chambers gets heated resulting in higher percentage for V_{crr}.

Table 4.2: Summary of fitted parameters for 15PC 9SKP.

Location in 3x3 Array												
Fitted Parameters		Units	Heater	1st Stage	2nd Stage	3rd Stage	4th Stage	5th Stage	6th Stage	7th Stage	8th Stage	9th Stage
V_{crr}		cm^3	-	0.01	0.01	0.01	0.01	0.01	0.01	0.01	0.01	0.26
τ_a	Heat	s	90	126	126	126	126	126	126	126	126	207
	Cool	s	94	132	132	132	132	132	132	132	132	216
d_L	Heat	µm/ cm^2	-	22	22	22	22	22	22	22	22	29
	Cool	µm/ cm^2	-	22	22	22	22	22	22	22	22	29
f			-	0.88	0.88	0.88	0.93	0.93	0.93	0.88	0.88	0.88

For stages 1-8 in 15PC-MSKP, τ_a is 1.4 times the thermal time constant for heater itself. Whereas, τ_a for the air entrapped in the 9th stage is ≈2.3 times the thermal time constant for heater. The 9th stage has a longer time constant because it has a larger volume of air encapsulated in its hot chamber that must heated. However, τ_a for heating/cooling in 15PC-SSKP is significantly larger than either of the stages in 9SKP because it has the significantly large V_{crr}.

The arrayed structure of the MSKP results in non-uniform thermal loss from different stages. Hence, the temperature gradient across various stages is expected to be non-uniform. Moreover, the heater used is narrower on one side, so the stages 1-3 and 7-9 are not completely covered by the heater, which contributes to the non-uniformity in temperature gradient across various stages. A finite element (COMSOL^{TM}) model is used to estimate the relative variation in temperature gradient across various stages with respect to the 5th stage. (The temperature gradient across 5th stage is used as reference because it is located at the center and is expected to have the highest temperature gradient.) Subsequently, the fitted model is used to estimate the fitted parameter f for the 5th stage. The parameters f for remaining stages are determined by scaling down the fitted value of f for the 5th stage based on the relative variation in the temperature bias across various stages, as predicted by the FE model. The fitted parameter f is 0.88 for stages 1-3 and 7-9, whereas its value for stages 4-6 is 0.93.

The model uses nominal values for the unknown parameters (a or f_p), which are derived from the steady state characterization of various ceramics (Table 4.1). The limiting values for the derived structural parameters are associated with the cases:

$$\left\| \frac{Q_{mxE} - Q_{mxM}}{Q_{mxE}} \right\| \approx 0 \tag{4.11}$$

and

$$\left\| \frac{P_{mxE} - P_{mxM}}{P_{mxE}} \right\| \approx 0 \tag{4.12}$$

These structural parameters have significantly large error margins associated with them because the steady state analysis does not account for all the non-idealities. Moreover, large error bars for a (or f_p) may be due to their relatively large standard deviation of the pore sizes and percent porosity of the ceramics (Table 4.1). A more rigorous analysis may require the knowledge of pore size distribution, impurities in the nanoporous ceramic, etc. Such detailed characterization may require sophisticated imaging techniques that can image the bulk nanopores and their distribution without damaging the sample itself. Detailed imaging of these nanoporous ceramics is out of the scope of present analysis.

This work suggests that 15PC-MSKP is effective in generating desired gas flow rates at required pressure heads, which was not possible with the single stage Knudsen pump [Var01, McN05, Gup08]. The performance results from 15PC-MSKP affirm the fact that Knudsen pumps can potentially be useful for liquid droplet manipulation in biological assays. Rate of increase in the droplet speed per unit increment in input power suggests that the device can provide volumetric delivery of liquid sample into a designated assay with a precision of ≈1 nL/min per unit mW input power (Fig. 4.13). The slope of load-flow characteristics, shown in Figure 4.12, suggests that the volumetric delivery of fluid sample into a designated assay can also be controlled upto a precision of 0.3 nL/min/Pa by regulating the pressure head driving the droplet.

4.5 Summary

The 15 bar nanoporous ceramic (15PC) from Soil Moisture and Equipment Corporation is one of the most promising ceramics for Knudsen pumps. Large nanopore diameter and high porosity of 15PC result in gas flow rates as high as high as 3.7 μL/min against a pressure head of 160 Pa. Further, for an input power of 1.9 W, the serially connected 9-stage structure of MSKP, with footprint 25x25 mm^2, allows a pressure head as high as 12 kPa. These operating characteristics suggest the potential utility of multiple stage Knudsen pumps for liquid droplet manipulation capabilities in biological assays. The 9-stage pump has also been demonstrated as pumping water drops through a 250 μm ID fluorinated ethylene propylene capillary at speeds in excess of 1.2 mm/sec. The MSKP has also been demonstrated to operate continuously for more than 7000 hours without any observable deterioration in its performance. A semi-analytical fitted model has been proposed that uses four fitted parameters to estimate the highly nonlinear temporal evolution of the pressure at the sealed outlet of the single stage and the multistage Knudsen pumps. The fitted model can reproduce the experimentally measured results with root mean square error of <110 Pa.

Having demonstrated the feasibility of the multistage Knudsen pump to meet the performance requirement of various microsystems, the fabrication process and the materials used can be refined further to optimize the efficiency of the device and to minimize the size of the device. A suitable choice of materials and fabrication steps is expected to enable batch fabrication methods for these devices.

CHAPTER 5

NANOPOROUS POLYMER MEMBRANE BASED SINGLE STAGE KNUDSEN PUMP

Although nanoporous ceramic based Knudsen pumps continue to show promise for thermal transpiration driven Knudsen pumping at atmospheric pressures, these have limited gas flow generation capability. Nanoporous polymer membranes have been introduced that have pore sizes significantly larger than the pore sizes in the nanoporous ceramics, which allows them to achieve higher thermal transpiration driven gas flow rates[4]. These membranes have higher percent porosity, which is also favorable for high gas flow rates. Although these membranes are about 100 μm thick, high thermal insulation allows them to sustain significant thermal gradient with reasonably low power inputs.

The primary goal for the work described in this chapter is to maximize the thermal transpiration driven gas flow rate of a Knudsen pump by using nanoporous polymer membrane as the transpiration element. In addition, the secondary goal is to study the vacuum generation capabilities of polymer based Knudsen pumps.

[4] Portions of this chapter have appeared in conference abstract form in [Gup10].

5.1 Nanoporous Polymer Membranes

Conventionally, nanoporous polymer membranes are used for filtration purposes and therefore have well controlled nanopore diameters. The nanopore diameters are on the order of 25-100 nm, and porosity is on the order of 70-75%, both of which are promising for high gas flow rates in Knudsen pumps. The low thermal conductivity of these membranes also acts in favor of the power efficiency. In this chapter, a mixed cellulose ester (MCE) nanoporous polymer membranes has been used, which are marketed as microfilters by Millipore Corporation. They have high percent porosity (≈70%), low (bulk) thermal conductivity (≈0.2 W/m-K).

Experiments performed as part of this effort suggest that commercially available nanoporous polymer membranes are relatively defect-free as compared to the bulk nanoporous ceramics reported in Chapters 3 and 4. Transpiration elements based on membranes with three different pore sizes – 25 nm, 50 nm, and 100 nm – are evaluated in this chapter. Gas flow characteristics and vacuum generation capabilities of Knudsen pumps based on these transpiration elements are used to identify the most favorable element for thermal transpiration driven gas pumping. Finally, the performance

Table 5.1: Summary of the types of polymer membranes and number of layers of polymer membranes used in different transpiration elements and corresponding Knudsen pumps.

Device#	Membrane Layout	Membrane Diameter	Thickness of individual layer	Nanopore diameter	% porosity	# of layers
		mm	μm	Nm	%	
SSKP1	PM1	11.5	105	25	70	1
SSKP2	PM2	11.5	105	25	70	5
SSKP3	PM3	11.5	105	50	72	1
SSKP4	PM4	11.5	105	50	72	5
SSKP5	PM5	11.5	105	100	74	1
SSKP6	PM6	11.5	105	100	74	5

characteristics of single stage Knudsen pumps using that transpiration element are studied in detail.

5.2 Device Structure

Six different transpiration elements were studied in this effort. A transpiration element refers to the component of a Knudsen pump that results in thermal transpiration driven gas flow when subjected to a temperature gradient. The transpiration elements were made from mixed cellulose ester (MCE) nanoporous polymer membranes, with pore sizes 25 nm, 50nm, and 100 nm; and percent porosity of 70%, 72%, and 74%, respectively. Three of the transpiration elements used a single layer of these membranes; three additional elements used 5 layers of these membranes (Table 5.1).

One of the primary challenges in using transpiration elements based on such thin

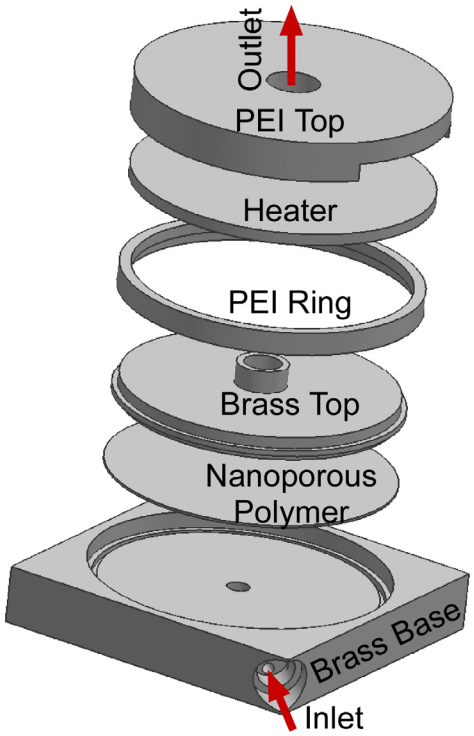

Fig. 5.1: Exploded view of a nanoporous polymer based single stage Knudsen pump.

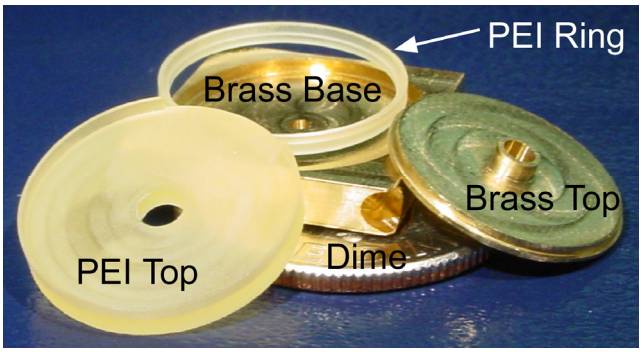

Fig. 5.2: Various components used in nanoporous polymer membrane based single stage Knudsen pumps.

membranes is to impose a meaningful temperature gradient across its thickness. This is accomplished by sandwiching the transpiration element between two brass elements – the brass base and the brass top (Fig. 5.1). The brass base is cooled by a passively cooled heat sink. The brass top is maintained at a higher temperature with the help of a heater above it. A polyetherimide (PEI) ring is used to thermally isolate the top and the bottom brass elements. The heater, located on the brass top, has a thin, etched foil, resistive element (≈26 Ω) laminated between insulating layers of Kapton (Minco, MN). Finally, the structure is sealed from top using a PEI cap. Thermocouples are used to record the temperature of the heater and the brass base. Stainless steel capillaries are used at the inlet and outlet ports.

For this effort, the brass and PEI elements were machined using CNC milling (Fig. 5.2). A vacuum epoxy, STYCAST2850FT/Catalyst 9 was used to hermetically seal various elements in place. Figure 5.3 shows the final assembled device – it has a final packaged volume of 14x14x4.5 mm^3. Note that the transpiration element PM1 is used in the Knudsen pump SSKP1, PM2 is used in SSKP2 and so on (Table 5.1).

5.3 Fitted Model

The fitted model presented here is a derivative of the models presented in the previous two chapters. However, unlike Chapter 3 and 4, the work in this chapter addresses the vacuum generation capabilities of a polymer based Knudsen pump. So, the fitted model here emulates the temporal evolution of vacuum generated in the (sealed) cold chamber, that is, at the inlet.

Note that since the fitted model here addresses the transient pressure response at the sealed cold chamber, there is no heating of air molecules under consideration. Hence, two of the fitted parameters – thermal time constant of air, f_{air} or τ_a; and corrected volume, V_{crr} – discussed in Chapters 3 and 4 can be eliminated. So, the fitted model presented here has only two fitted parameters: (i) Leak aperture, D_L, present in the transpiration element. (ii) loss in the temperature bias at various interfaces due to the thermal contact resistance, f.

The definition for D_L is same as in Chapters 3 and 4. However, the second fitted

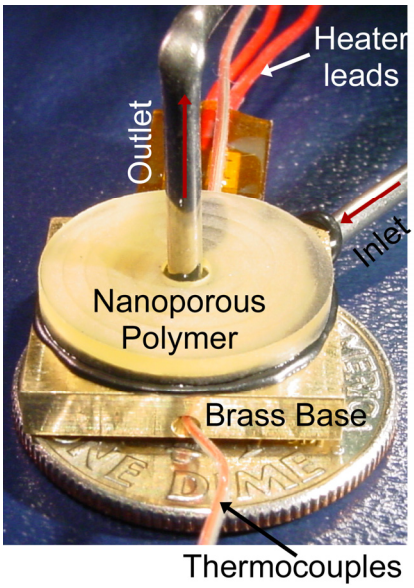

Fig. 5.3: Photograph of a nanoporous polymer based single stage Knudsen pump. It has a final packaged volume of 14x14x4.4 mm^3.

parameter has been redefined to predict the effect of thermal contact resistances more precisely. The second fitted parameter is denoted by f and, as in Chapter 4, it is used to estimate the fraction of experimentally measured applied temperature bias to the Knudsen pump that actually appears across its transpiration element. However, unlike Chapter 4, the model presented here assumes that the (overall) loss in temperature bias due to the thermal contact resistances is divided equally at the top facet and at the bottom facet of the transpiration element.

Figure 5.4 shows typical variation in the estimated (i.e. fitted) and the experimentally measured temporal evolution of pressure at the sealed inlet of a Knudsen pump. Unlike the pressure profile presented in the Fig. 3.7, the pressure profile here can be controlled by using only two fitted parameters, discussed above. The difference between the steady state values of the experimental and the fitted pressure profiles, e_{PHss}, depends primarily on D_L and the fitted parameter f is used to minimize the total RMS error, e_{RMS}, between

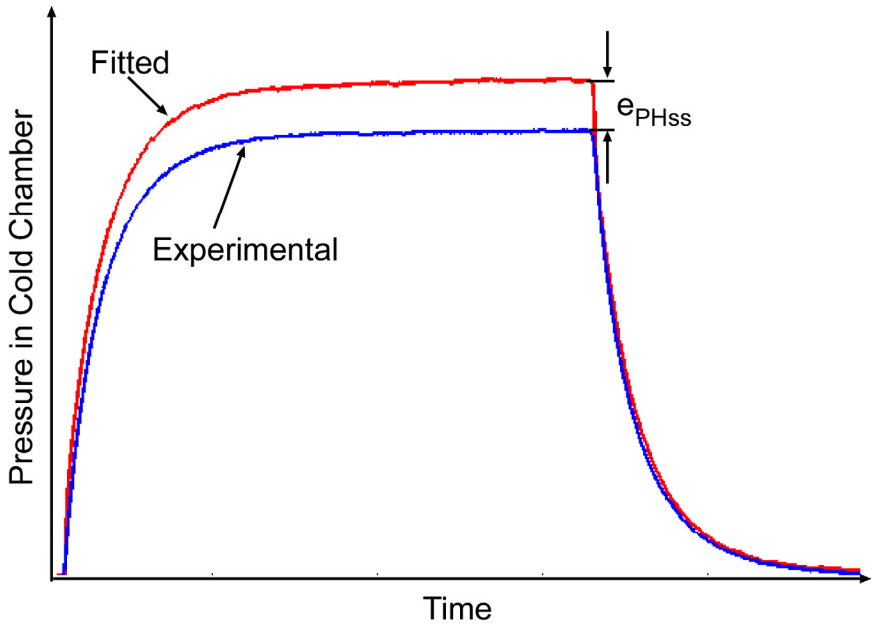

Fig. 5.4: A typical variation in the estimated (i.e. fitted) and the experimentally measured temporal evolution of pressure at the sealed inlet of a Knudsen pump.

the fitted and the experimental pressure profiles.

Figure 5.5 shows the flowchart for the fitted model and a detailed step-by-step algorithm for the fitted model is presented below:

Step 1: Choose a suitably small time step (Δt) and interpolate $T_{He}(t)$, $T_{Ce}(t)$, $P_{He}(t)$ and $P_{Ce}(t)$ for all the time steps.

Step 2: Choose initial value for D_L, and f. Due to the asymmetric nature of the problem, these parameters may have different values, while the heater is on and while it is off.

Step 3: Estimate the initial number of moles of air in the cold chamber based on the

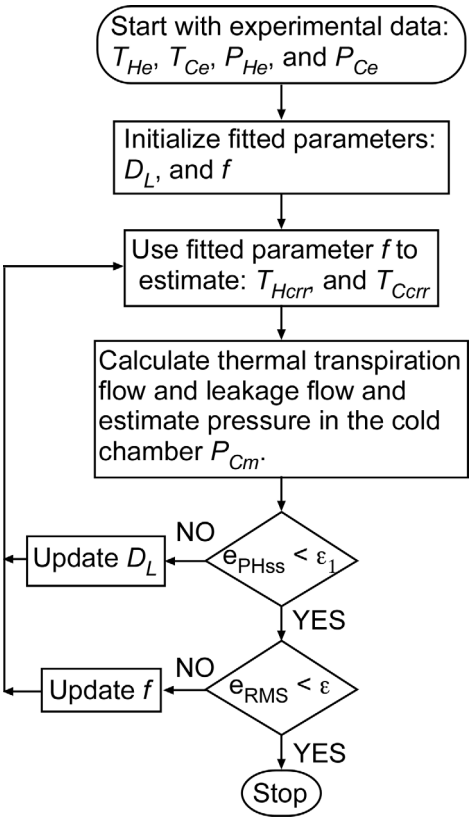

Fig. 5.5: The flowchart for key steps involved in the fitted model.

initial temperature, pressure of the device and the volume of the cold chamber.

$$N(0) = \frac{P_{Ce}(0).V_C}{R.T_{He}(0)} \tag{5.1}$$

Step 4: Evaluate the temperature at the hot and the cold facets of the transpiration element at time t.

$$T_{Hcrr}(t) = \frac{T_{He}(t) + T_{Ce}(t)}{2} + f\,\frac{T_{He}(t) - T_{Ce}(t)}{2} \tag{5.2}$$

$$T_{Ccrr}(t) = \frac{T_{He}(t) + T_{Ce}(t)}{2} - f\,\frac{T_{He}(t) - T_{Ce}(t)}{2} \tag{5.3}$$

Step 5: Evaluate average values of T_{Hcrr}, and T_{Ccrr} over the period t to t+Δt.

$$\overline{T}_{Hcrr}(t + \Delta t) = \frac{T_{Hcrr}(t + \Delta t) + T_{Hcrr}(t)}{2} \tag{5.4}$$

$$\overline{T}_{Ccrr}(t + \Delta t) = \frac{T_{Ccrr}(t + \Delta t) + T_{Ccrr}(t)}{2} \tag{5.5}$$

Step 6: Substitute for $T_H = \overline{T}_{Hcrr}(t + \Delta t)$; $T_C = \overline{T}_{Ccrr}(t + \Delta t)$; $P_H = P_{Hm}(t) = P_{He}(t)$ and $P_C = P_{Cm}(t)$ in Equation 2.15 to calculate the thermal transpiration driven mass flow rate and divide it by the molecular mass M of air to estimate the number of moles of gas molecules $N_{TT}(t+\Delta t)$ pumped out of the cold chamber due to the thermal transpiration pumping.

Step 7: Use D_L, P_H and P_C in Equation 2.19 to calculate the leakage flow, multiply it with the density of air (Eqn. 2.7), and divide it by the molecular mass M of air to estimate the effective number of molecules $N_{POS}(t+\Delta t)$ leaking into the cold chamber.

Step 8: The effective number of moles of gas in the cold chamber after time $t+\Delta t$ is:.

$$N(t+\Delta t) = N(t) - N_{TT}(t+\Delta t) + N_{POS}(t+\Delta t) \tag{5.6}$$

Step 9: Estimate the final pressure in the chamber, assuming ideal gas behavior

$$P_{Cm}(t+\Delta t) = \frac{P_{Cm}(t)}{N(t)} N(t+\Delta t) \tag{5.7}$$

Step 10: Increment time, i.e. $t = t+\Delta t$; and repeat steps 4 to 9 for all the time steps.

Step 11: Update D_L and repeat steps 3 to 10 until e_{PHss} is smaller than ε_1, where ε_1 is the acceptable tolerance in minimizing e_{PHss}.

Step 12: Update f and repeat steps from 3 to 11 such that e_{RMS} is smaller than ε, where ε is the acceptable tolerance in minimizing e_{RMS}.

Thus, the fitted model provides an estimate for the fitted parameters D_L, and f, such that the RMS error between the experimentally measured and modeled pressure in the hot chamber is minimized. Note than the tolerances ε_1, and ε may vary from one iteration to the next.

5.4 Results and Discussion

This section presents steady state and transient testing results from the six transpiration elements (PM1 to PM6) and Knudsen pumps (SSKP1 to SSKP6) based on these transpiration elements (Table 5.1). Performance characteristics of these Knudsen pumps have been studied at and below atmospheric pressure. *However, all the experimental results are at atmospheric pressure unless specified.*

5.4.1 Test Set-up

A. Isothermal Pressure Driven Flow

Figure 5.6 shows a schematic layout of the test set-up used for isothermal pressure driven gas flow characterization of the transpiration elements PM1 to PM6. Each of these transpiration elements were mounted in a transpiration element assembly, which

was sandwiched between a threaded glass tube and its plastic cap. "O"-rings were used to seal the assembly between the glass tube and the plastic cap. The plastic cap was connected to a vacuum chamber, which was used to apply a (externally) controlled pressure differential across the transpiration element. The other end of the glass tube was connected to a clear Tygon tubing, inner diameter 1/32", with a water plug to visualize and quantify the gas flow across the transpiration element. The corresponding pressure drop across the transpiration element was recorded using a differential pressure sensor.

The transpiration element assembly had a transpiration element sandwiched between two perforated brass discs, which was then bonded peripherally inside a metallic washer (exploded view shown in Fig. 5.6). Brass discs were used to support the transpiration

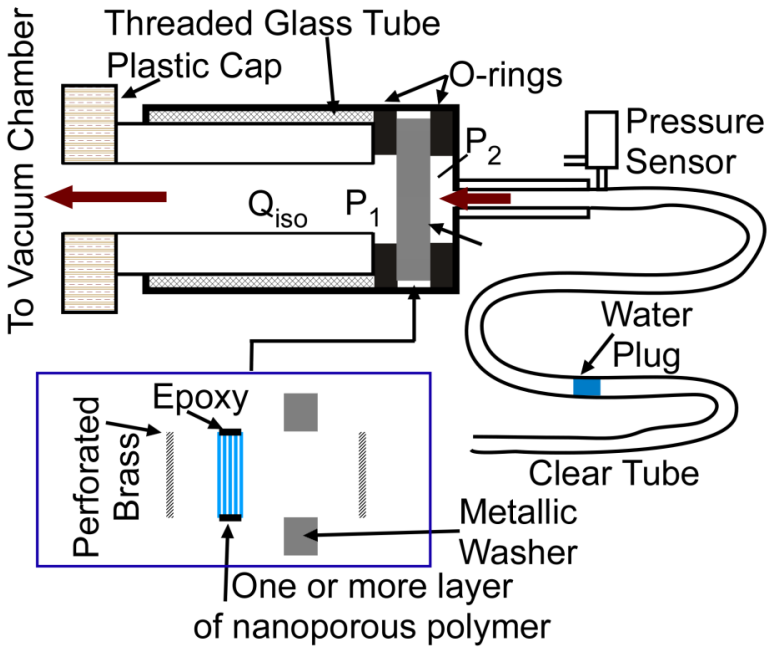

Fig. 5.6: Test set-up for isothermal pressure driven gas flow characterization of various tranpiration elements. (a) Transpiration element assembly was sandwiched between two "O"-rings and vacuum pressure was applied from one side to create pressure difference across the transpiration element. (b) The transpiration element assembly compised of transpiration element sandwiched between two perforated brass discs; transpiration element and the brass discs were mounted inside and bonded peripherally to a metallic washer that could be firmly clamped between the two "O"-rings.

element in order to protect it from structural damage due to the externally applied differential pressure. The metallic washer provided structural support to the transpiration element, so that it could be clamped firmly in the test set-up.

B. Knudsen Pumping Characteristics

Figure 5.7 shows the schematic layout of the test set-up used to quantify the Knudsen pumping characteristics of the devices SSKP1 to SSKP6. These devices were tested in a controlled pressure chamber (CPC). The pressure inside CPC and hence the ambient operating pressure of these devices was regulated using an external vacuum pump. The bottom facet of the device was maintained in thermal equilibrium with a heat sink, which was passively maintained at room temperature. Vacuum grease was used at the bottom facet of the Knudsen pump to ensure effective thermal coupling between the brass base and the heat sink. In this study, Knudsen pumps were tested in two different modes – *pressure mode* and *flow mode*. While operating in pressure mode, the inlet of the pump was sealed and the outlet was open to the CPC. The temporal evolution of pressure at the

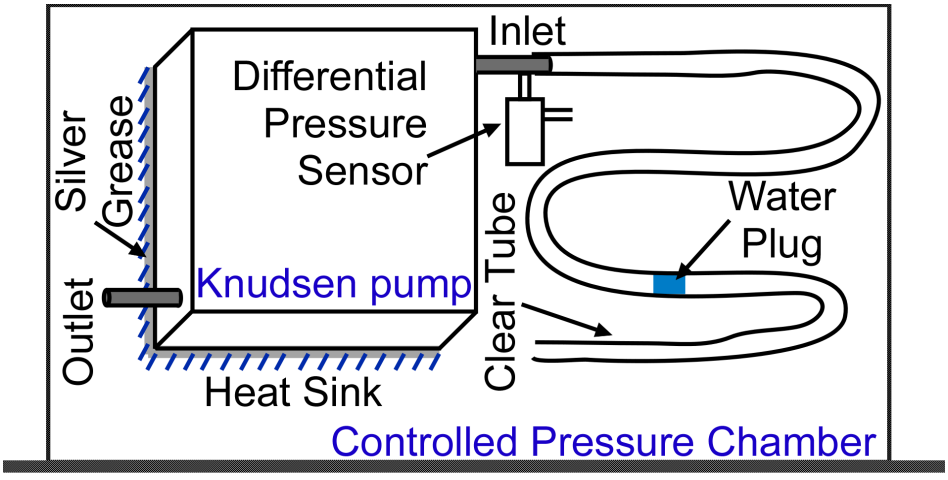

Fig. 5.7: Test set-up for thermal transpiration driven gas flow characterization of a Knudsen pump. The pressure chamber is used to regulate the ambient operating pressure of the Knudsen pump.

sealed inlet was recorded using a differential pressure sensor – one end of the pressure sensor was connected to the inlet of the Knudsen pump and the other end was open to CPC. While operating in flow mode, the inlet of the Knudsen pump was connected to a differential pressure sensor, and Tygon tubing with one or more water plugs in it. Again, water plugs were used to visualize and quantify the gas flow generated by these devices and corresponding pressure load at the inlet was recorded using the differential pressure sensor. Pressure load applied at the inlet was controlled by changing the number of water plugs in the tubing. Note that there are two mechanisms by which a water plug offers resistance to the gas flow: (i) viscous drag at the outer periphery of the water plug; (ii) absorption/release of free energy at the two menisci of a plug. Experiments suggested that pressure load from the later is significantly larger than the former. Hence, the pressure load applied to the Knudsen pump was controlled by varying the number of water plugs instead of varying the length of a single water plug.

The voltage output from the two thermocouples and the pressure sensor were read into HP34401A multimeters. These multimeters were further connected to a PC, running a Labview™ program, through a National Instruments's GPIB-USB-HS data transfer cable to record the temporal variation in the voltage outputs.

Table 5.2: Experimentally measured hydraulic conductance K_H and its percentage deviation from the ideal hydraulic conductance K_{Hideal} for various transpiration elements.

Transpiration element	**K_H**	**K_{Hideal}**	**Deviation**
	sccm/Pa	sccm/Pa	%
PM1	1.97×10^{-3}	1.85×10^{-3}	6.5
PM2	4.21×10^{-4}	3.71×10^{-4}	13.5
PM3	3.15×10^{-3}	3.71×10^{-3}	15.1
PM4	6.76×10^{-4}	7.44×10^{-4}	9.1
PM5	5.46×10^{-3}	7.62×10^{-3}	28.3
PM6	1.1×10^{-3}	1.53×10^{-3}	27.5

5.4.2 Steady State Results

A. Isothermal Pressure Driven Flow Characteristics

Figure 5.8 illustrates the isothermal pressure driven gas flow characteristics of the six transpiration elements studied here. The gas flow through these elements, Q_{iso}, increased linearly with (externally) applied pressure differential ΔP across these elements. Hence:

$$Q_{iso} = K_H.\Delta P \tag{5.8}$$

Based on the experimentally measured values for Q_{iso} and ΔP, the hydraulic conductance K_H of various transpiration elements (diameter ≈11.5 mm) is listed in Fig. 5.8. The experimentally measured hydraulic conductance values, K_H, of these transpiration elements were in close agreement with the ideal hydraulic conductance, K_{Hideal}, estimated using Sharipov's model (Table 5.2). In particular, the transpiration element PM1 could approach 95% of the ideally estimated value for hydraulic conductance, calculated using nominal values for polymer membrane parameters. Close

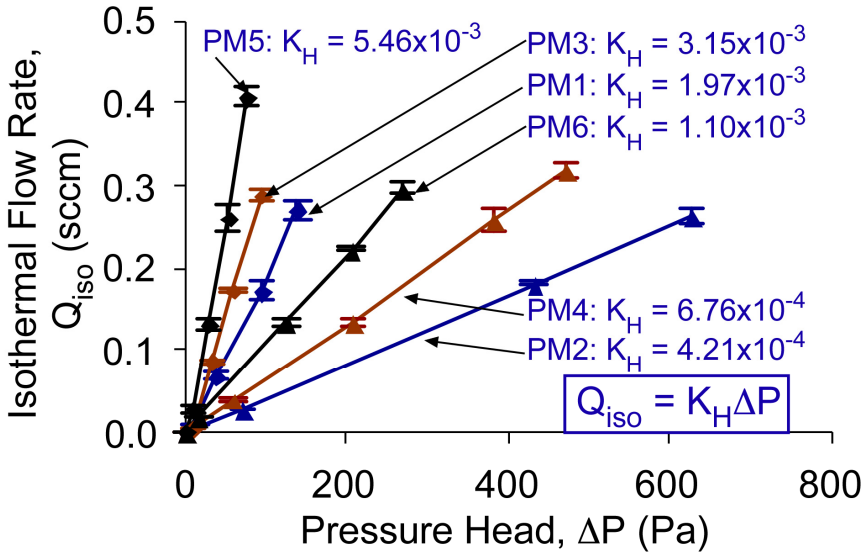

Fig. 5.8: Rate of variation in the isothermal pressure driven gas flow rate with the applied pressure drop across the transpiration element yields the hydraulic conductance K_H of each of these elements.

resemblance between K_H and K_{Hideal} suggested that the pore size and the porosity of the polymer membranes had minimal deviation from their nominal values.

B. Thermal Transpiration – Pressure Mode Testing

As mentioned in Chapter 1, ideally, the pressure ratio generated by a Knudsen pump is equal to the square root of the temperature ratio across the transpiration element (Eqn. 1.1). However, in practice, the pressure ratio generated is smaller than the square root of the temperature ratio due to various non-idealities present in the system. A lumped parameter f_N was introduced in this chapter to quantify the effects of various non-idealities on the pressure ratio generation capabilities of the polymer based Knudsen pumps discussed here (Fig. 5.9). This lumped parameter was defined as:

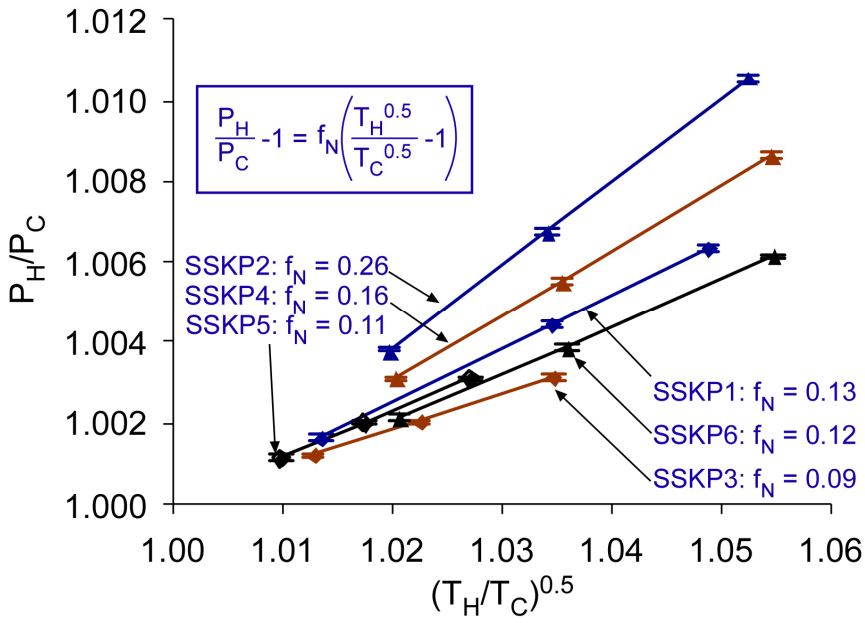

Fig. 5.9: Pressure Mode Testing: Variation in pressure ratio generated by various Knudsen pumps with applied temperature ratio. A limped parameter f_N was introduced to quantify various non-idealities that diminish the pressure (ratio) generation capability of a Knudsen pump.

$$\frac{P_H}{P_C} - 1 = f_N \left[\left(\frac{T_H}{T_C} \right)^{0.5} - 1 \right] \tag{5.9}$$

Figure 5.9 shows variation in the pressure ratio generated by devices SSKP1 to SSKP6 with applied temperature ratio. Parameter f_N has been identified for each of these devices. It is expected to be higher for transpiration elements with smaller nanopore diameter and it is also expected to have greater values for Knudsen pumps based on transpiration elements with 5-layered structure than for the Knudsen pumps with single-layered structure. However, some of the pumps (SSKP3, in particular) do not follow these trends (Fig. 5.9), potentially because of the variation in the non-idealities from device to device. These non-idealities include thermal contact resistance, leak aperture diameter, etc.

Similar experiments at sub-atmospheric pressures suggested that the pressure ratio generation capabilities of these Knudsen pumps, for a given temperature ratio, increase

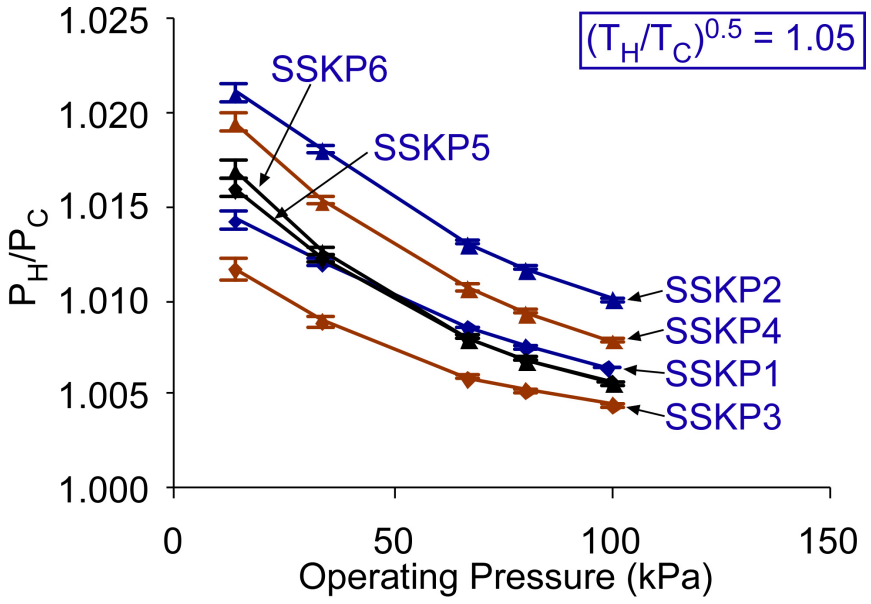

Fig. 5.10: Pressure Mode Testing: Pressure ratio generated by a Knudsen pump increases as the ambient operating pressure of these pumps decrease.

with decreasing operating pressures. Figure 5.10 illustrates the variation in pressure ratio P_H/P_C with ambient operating pressure P_{vc} of the devices SSKP1 to SSKP6 held at $(T_H/T_C)^{0.5} = 1.05$. This happens because with reduction in pressure the gas flow through the transpiration element extends further into the free molecular regime, i.e., the Knudsen number increases. Higher Knudsen number reduces the leakage flow and is more favorable for achieving higher P_H/P_C for a given T_H/T_C. Moreover, at sufficiently low pressures the mean free path of the gas molecules becomes larger than the hydraulic diameter of the micro-defects in the transpiration element and these (also) start supporting thermal transpiration flow through them.

Figure 5.11a shows the maximum (differential) vacuum pressure generated by devices SSKP1 to SSKP6 at their sealed inlet for an input power of ≈1 W. The bar graph suggests that SSKP2 has the best vacuum generation capabilities followed by SSKP4, SSKP6, SSKP1, SSKP3, and SSKP5 in decreasing order. In other words, for a given number of layers of nanoporous membranes in a transpiration element, Knudsen pumps that used transpiration elements based on membranes with 25 nm pore sizes had higher vacuum generation capabilities than those which used transpiration elements based on membranes with 50 nm or 100 nm pore sizes. For example, among Knudsen pumps with single layered structure for transpiration element, SSKP1 had the highest vacuum generation capability; similarly, among Knudsen pumps with five-layered structure for transpiration element, SSKP2 resulted in highest vacuum. The input power to each of these pumps was 1W.

Further, the experimentally measured temporal evolution of vacuum at the sealed inlet of each of these pumps was used to estimate their respective time constants for evacuating an encapsulated volume ≈0.43 cm^3 (Fig. 5.11b) to their respective steady state pressure shown in Fig. 5.11a. Analysis suggested that both the Knudsen pumps that used membranes with 25 nm pore size have almost identical time constants. Other pumps either have poor vacuum generation capability or high time constant for evacuation or both. Hence, Knudsen pumps SSKP1 (based on transpiration element PM1) and SSKP2 (based on transpiration element PM2) have been chosen for the purpose of further analysis.

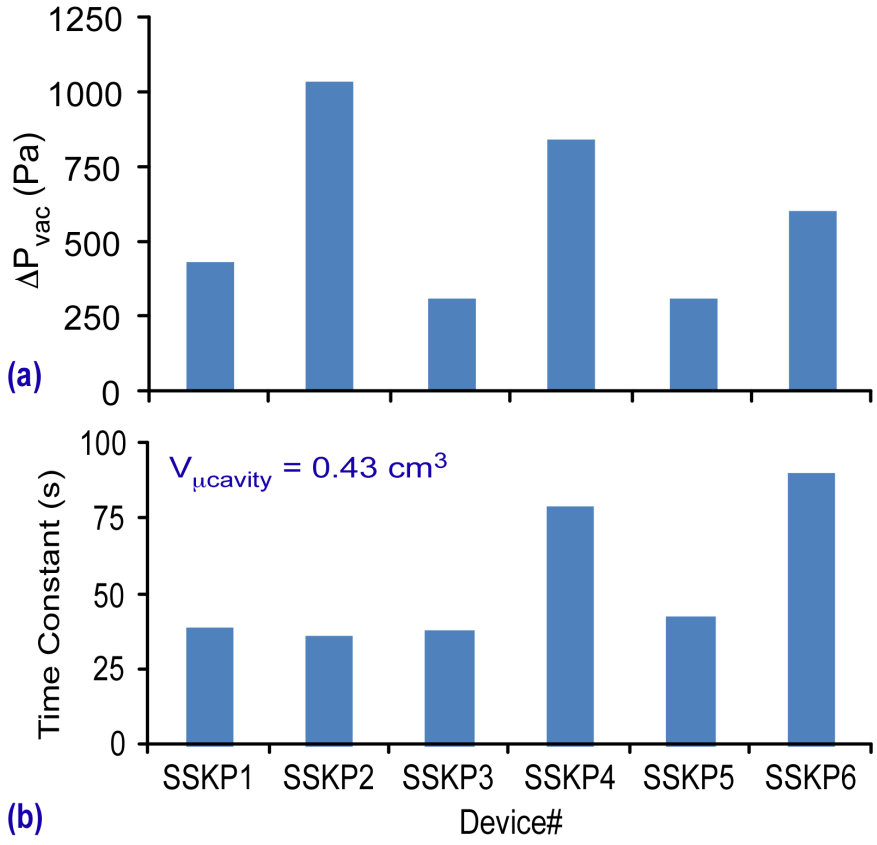

Fig. 5.11: Pressure Mode Testing: Vacuum pressure generation capabilities of various Knudsen pumps. (a) The maximum vacuum pressure generated by various Knudsen pump for an input power of 1 W; (b) The time constant for each of these pumps to evacuate a 0.43 cm^3 micro-cavity down to the corresponding maximum vacuum pressures shown in (a).

C. Thermal Transpiration – Flow Characteristics

If Q_{TT} is the temperature gradient driven thermal transpiration flow from the cold side to the hot side of the transpiration element, and Q_{PR} is the pressure gradient-driven gas flow across the transpiration element from its hot side to its cold side. The net flow Q_{eff} is the algebraic sum of these two gas flow rates, that is:

$$Q_{eff} = Q_{TT} - Q_{PR} \tag{5.10}$$

For the purpose of present analysis it is assumed that the non-isothermal pressure (only) driven gas flow characteristics as identical to the isothermal pressure driven gas flow characteristics of the transpiration element. Hence:

$$Q_{PR} = Q_{iso} = K_H.\Delta P \tag{5.11}$$

As mentioned earlier, inlet of a Knudsen pump is sealed while testing it in pressure mode. This implies that the effective gas flow across its transpiration element at steady state is zero: $Q_{eff} = 0$. Hence, $Q_{TT} = Q_{PR} = K_H.\Delta P$. This value of Q_{TT} can, therefore, be

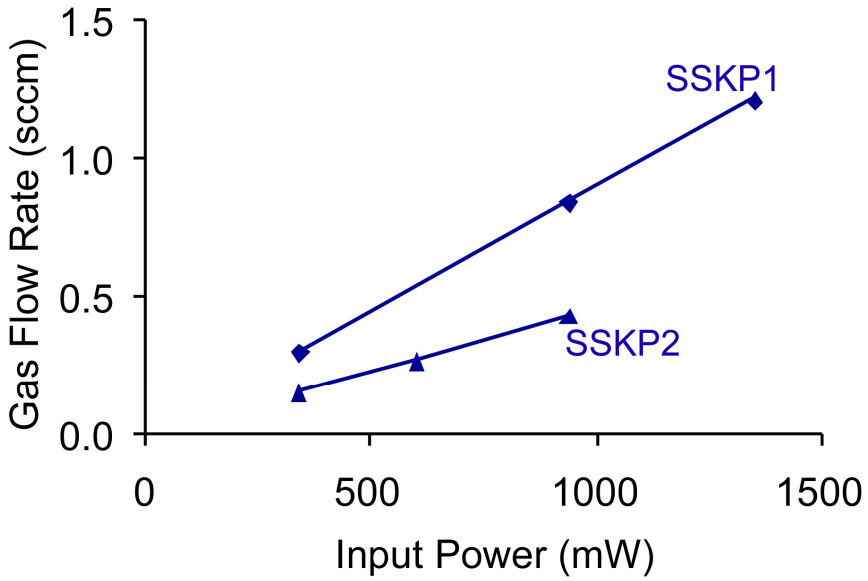

Fig. 5.12: Pressure Mode Testing: Variation in the thermal transpiration driven gas flow Q_{TT} generated by Knudsen pumps SSKP1 and SSKP2 with the input power to the devices.

extracted from the Pressure Mode Tests. Figure 5.12 shows that Q_{TT} for SSKP1 is about 2x greater than that for SSKP2 under similar operating conditions. However, SSKP2 has 2.4x more vacuum generation capability than SSKP1 under similar operating conditions (Fig. 5.11). So, there exists a trade-off in choosing the 5-layered transpiration element PM2 (used in SSKP2) versus a single layered transpiration element PM1 (used in SSKP1). Although PM2 had slight advantage over PM1, PM1 was preferred because it yielded results that were more representative of the idealized results estimated based on the Sharipov model (Table 5.2). Moreover, use of the multilayered transpiration element PM2 would have increased the fabrication complexity, which would adversely affect the yield. Hence, PM1 was the preferred transpiration element for thermal transpiration driven Knudsen pumping, particularly while operating close to atmospheric pressure.

Equation 5.10 and 5.11 suggest that for the no load case $\Delta P = 0$, $Q_{eff} = Q_{TT}$. Hence, the pressure mode testing results, shown in Fig. 5.12, suggest that for an input power of

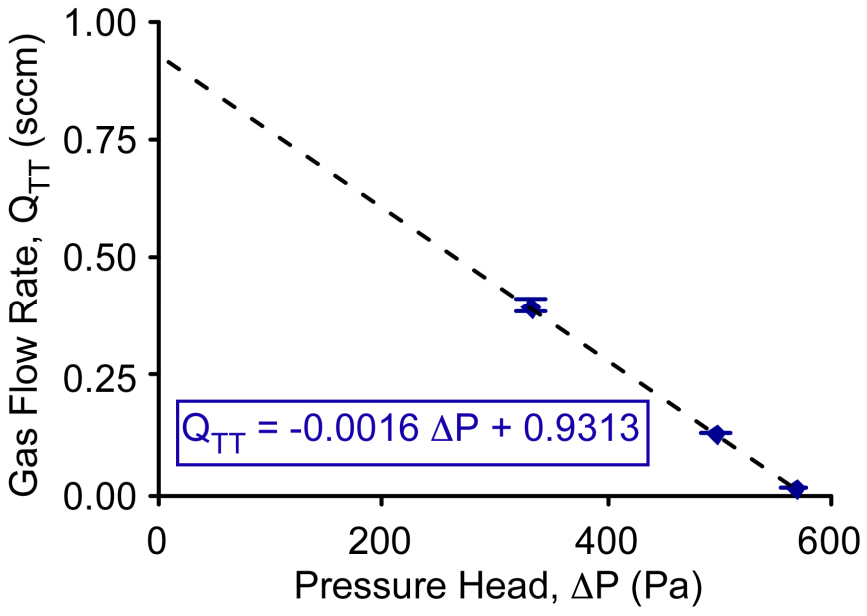

Fig. 5.13: Flow Mode Testing: Variation in the experimentally measured gas flow rate generated at the inlet of SSKP1 with applied pressure head at the inlet.

1.4 W, SSKP2 can result in a no load gas flow rate of about 1.2 sccm.

Figure 5.13 shows the experimentally measured gas flow generated by the device Q_{eff} with pressure load ΔP at the inlet. The input power was held constant at 1.4 W for this experiment. The pump was demonstrated to generate a gas flow rate of 0.4 sccm against a pressure load of 330 Pa at its inlet. As expected, the measured gas flow increased with reduction in the pressure load. The load flow characteristics illustrate that for a limiting case with no (external) pressure load at its inlet, the pump could result in gas flow rates as high as 0.93 sccm. Note that, while operating in flow mode, the pump has to overcome internal load offered by various elements. Hence, no (external) load gas flow rate, extrapolated from direct flow measurement results, is smaller than the no load flow estimated from pressure mode testing results.

In order to test the reliability of the polymer based Knudsen pumps, the SSKP1 is being operated continuously in flow mode for extensive periods. To date, it has operated continuously for more than 600 hours without any deterioration in its performance (Fig.

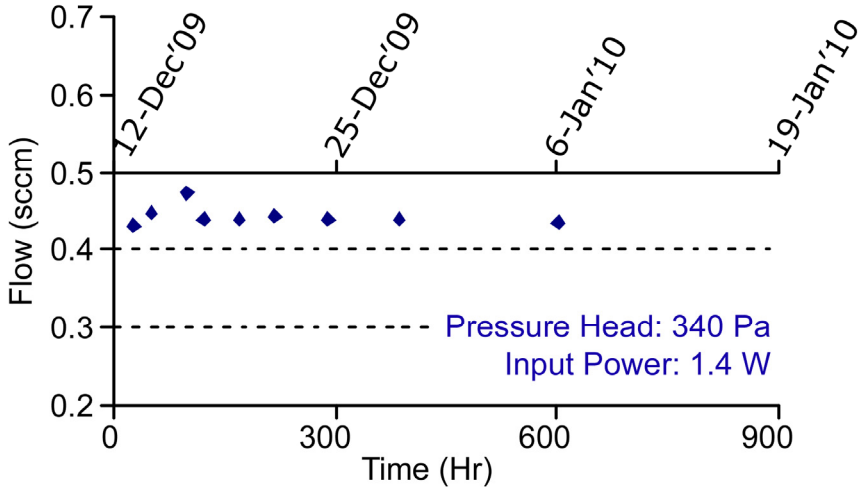

Fig. 5.14: The variation in gas flow rate with time during a continuous 600 hours operation of the SSKP1. The average gas flow rate generated during this period is 0.44 sccm with a standard deviation of 0.01 sccm.

5.14). For an input power of 1.4 W, the average gas flow generated by SSKP1 during this period is ≈0.44 sccm with a standard distribution of ≈0.01 sccm (This flow rate is measured against a pressure load of 337 Pa.) The variation in gas flow rate is primarily due to the variation in the ambient operating temperature of the device. Variation in ambient temperature results in fluctuation of the effective temperature gradient across the ceramic discs, which, in-turn, results in variation of the gas flow rate generated.

5.4.3 Transient Results

A. Pressure/Flow Transients

Pressure Mode Testing: Figure 5.15a shows the experimentally measured transient differential vacuum pressure P_H-P_C ($=\Delta P(t)$) in the sealed cold chamber of SSKP1. The corresponding experimentally measured temperatures at the hot and at the cold ends of the transpiration element are plotted as T_H and T_C, respectively. The volume of the cold chamber was 0.46 cm^3 and the input power to the device was 1.4 W.

Time derivative of $\Delta P(t)$ is proportional to the gas pumped out of the cold chamber $Q_{eff}(t)$ (Fig. 5.15b). The product of K_H and $\Delta P(t)$ results in the rate of pressure driven gas flow into the cold chamber $Q_{PR}(t)$ (Eqn. 5.11). Sum of $Q_{PR}(t)$ and $Q_{eff}(t)$ provides the temporal evolution of the thermal transpiration flow $Q_{TT}(t)$ (Eqn. 5.10, Fig. 5.15b).

Figure 5.15 suggests that the device SSKP1 could generate thermal transpiration gas flow rate on the order of 1.2 sccm, while operating at temperature smaller than 60 °C. Moreover, the plot suggested that the time constant for P_H-P_C is almost identical to the time constant of T_H-T_C, which means that the primary factor limiting the rate of evacuation of the cold chamber was the thermal mass of the device. Reduction in thermal

mass of the device is expected to reduce the time constant for T_H-T_C and hence will reduce the time constant for P_H-P_C.

B. Fitted Model

Based on the experimentally measured T_H and T_C, the fitted model discussed in Section 5.3 was used to reproduce the experimentally measured P_H-P_C. This model

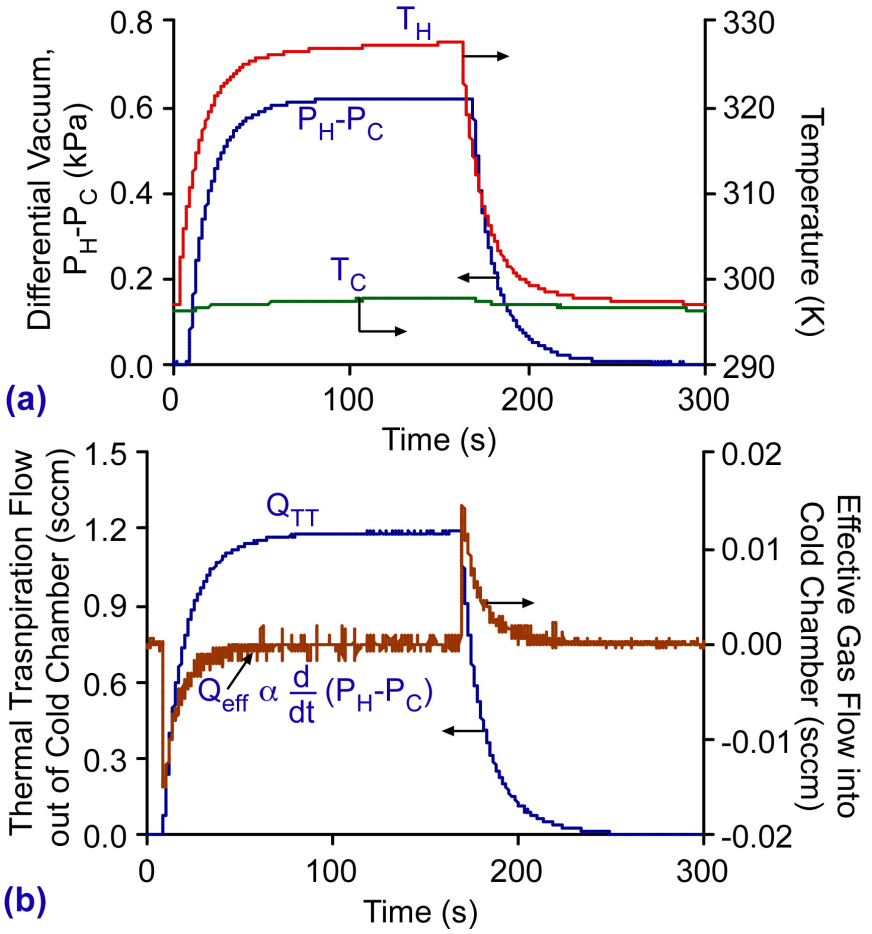

Fig. 5.15: Pressure mode transient pumping characteristics of SSKP1: (a) Measured temporal evolution of differential vacuum (P_H-P_C) at the sealed inlet, corresponding temperatures at the hot and at the cold ends of the transpiration element are T_H and T_C, respectively. (b) Effective gas flow into the cold chamber, calculated based on the variation in pressure at the sealed inlet. The sum of the effective gas flow Q_{eff} and the pressure driven backflow, $Q_{PR} = \Delta P.K_H = (P_H\text{-}P_C).K_H$, provides an estimate of the temporal evolution of thermal transpiration driven gas flow Q_{TT} generated by SSKP1.

served to quantify the two fitted parameters, f and D_L, such that the RMS deviation of the experimentally measured pressure and the modeled pressure was minimized. A preliminary estimate for the fitted parameter D_L was obtained from the deviation of the experimentally measured hydraulic conductance K_H of PM1 from its ideal value K_{Hideal} (Table 5.2). The difference in the two hydraulic conductance values suggested that the 11.5 mm diameter nanoporous polymer membrane with nanopore diameter 25 nm and percent porosity 70% had a leak aperture of 19.9 μm. This value for leak aperture was further verified using the fitted model.

The fitted pressure $(P_H\text{-}P_C)_{model}$ could reproduce the experimentally measured pressure $P_H\text{-}P_C$ with a root mean square error of smaller than 7.5 Pa, while using the values 0.18 and 19.9 μm for the fitted parameters f and D_L, respectively (Fig. 5.16a). Figure 5.16b shows the corresponding variation in the corrected temperatures at the hot end T_{Hcrr} and at the cold end T_{Ccrr} of the transpiration element. Experimentally measured variation in the temperatures at the hot (T_H) and at the cold (T_C) ends have also been shown. The model suggested that only 18% of the measured temperature drop across SSKP1 actually appears across the transpiration element PM1; remaining is lost in the non-idealities, such as, thermal contact resistances at various interfaces etc.

Apart from the various non-idealities in the systems, the fitted model could also capture measurement errors. The model suggested that the due to the compressible nature of the gas the time delay between the vacuum generated at the cold end of the transpiration element in SSKP1 and the vacuum pressure detected by the pressure sensor was of about 5 sec. High gas pumping speed (≈1 sccm) also contributed to the delay in propagation of vacuum in the cold chamber, which was essentially long and slender in

geometry with Knudsen pump at one end and pressure sensor at the other end. Further, the model could capture a zero error of 13 Pa in the experimentally measured P_H-P_C.

5.5 Summary

Nanoporous polymer based Knudsen pumps have been demonstrated to be one of the

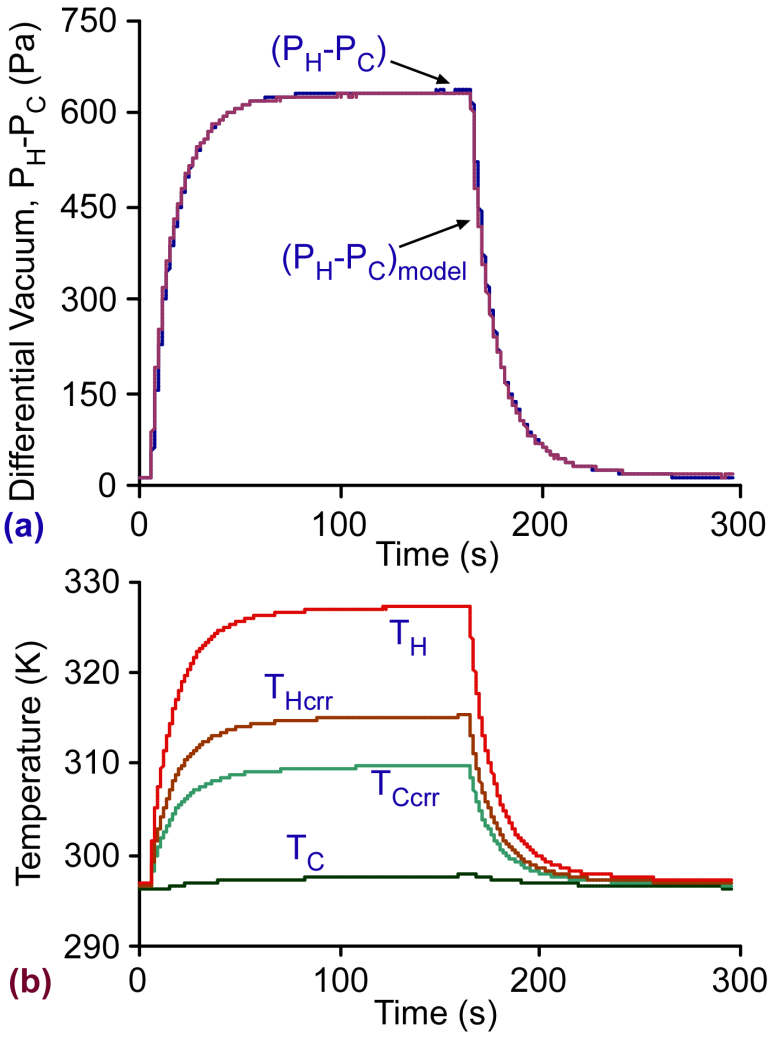

Fig. 5.16: Pressure Mode Testing: (a) The fitted pressure $(P_H-P_C)_{model}$ at the sealed inlet of SSKP1 could reproduce the corresponding experimentally measured pressure P_H-P_C with a root mean square error of <7.5 Pa. (b) T_H and T_C show the temperature recoded by the thermocouples at the hot and the cold ends of the transpiration element (PM1) used in SSKP1. T_{Hcrr} and T_{Ccrr} are the corrected temperatures at the hot end and at the cold end of the PM1 after accounting for thermal contact resistances – as estimated by the fitted model.

most promising options for generating thermal transpiration driven gas flow rates in excess of 1 sccm. Experimentally measured isothermal pressure driven gas flow characteristics for these polymer membranes are in close agreement with the ideal values. In particular, the nanoporous polymer membrane with pore size 25 nm and percent porosity 70% has been identified as the most favorable transpiration material for thermal transpiration driven Knudsen pumping. These polymer membranes are promising for high vacuum pressure generation. The pressure ratio generated by these membranes for a given temperature ratio increases with lower operating pressures. Finally, the two fitted paramaters: (i) fraction of experimentally measured temperature gradient that actually appears across the nanoporous ceramic, f; and (ii) leak aperture diameter in the transpiration element, D_L, have been identified to have values of 0.18 and ≈20 μm (respectively) for SSKP1. Although the leak aperture is significantly large, the high transpiration driven gas flow rate through the nanopores ensures that the loss in performance due to the leakage flow is proportionately small. The performance of the device (SSKP1) can potentially be improved to 5X the present values by optimizing the device structure such that the value of f is closer to 1.

The polymer pump SSKP1 has also been demonstrated to operate continuously for more than 600 hours without any observable deterioration in its performance.

CHAPTER 6

CONCLUSIONS AND FUTURE WORK

This research effort has evaluated several bulk nanoporous materials as candidate for the transpiration material in Knudsen pumps. The pumps are generally intended for microsystems used in gas sensing and micrototal analysis systems. As noted earlier, these bulk nanoporous materials have high density of interconnected narrow channels (10^{14} channels/cm^2) that pump gas in parallel. This high density of narrow channels is potentially adequate for generating gas flow rates that can be useful for the target microsystems.

Section 6.1 presents a brief overview of the strengths and the weaknesses of various Knudsen pumps and the transpiration materials used in those pumps. This discussion highlights key observations that were instrumental in determining the direction of research during the course of this study. Section 6.2 addresses how this work can be extended further targeting the long term goals of the project.

6.1 Conclusions

In Chapter 2, Sharipov's semi-analytical model for rarefied gas flow in narrow channels was identified as one of the most relevant for this work. The modeling results from the Sharipov's model are comparable to the DSMC technique and it is not as

computationally intense as the DSMC technique. This semi-analytical model is applicable to a wide range of gas flow regimes. A fitted model based on Sharipov's approach was developed and adapted to accommodate various non-idealities in the system. These non-idealities include thermal expansion/contraction of gas, leakage of air into/out of the device, thermal contact resistances at various interfaces, etc.

Table 6.1 summarizes the device parameters and performance metrics of different Knudsen pumps that were fabricated as a part of this effort. A Knudsen pump based on the naturally occurring zeolite, clinoptilolite (Chapter 3), demonstrated the feasibility of using a bulk nanoporous ceramic for thermal transpiration driven Knudsen pump. A

Table 6.1: Summary of performance characteristics of various devices discussed in this effort.

Sec.	**TT Matr'l**	**# of Stgs**	**Pump Size**	**TT Matr'l Size**	**Flow Rate**		**ΔP_{max}**	**Input Power**	**T_H**	**T_C**
	Matr'l (Pore Dia.)		**Area (thk.)**	**Dia. (thk.)**	**Best Measured**	**No load**				
	(nm)		mm^2 (mm)	mm (mm)	sccm	sccm	kPa	W	°C	°C
3.3	Zeolite (0.45)	1	55x55 (12)	48 (2.3)	0.12	0.13	1	5.35	75	42
4.4.3	Zeolite (0.45)	1	18x18 (6.5)	12.8 (2.2)	0.0005	0.0006	0.78	0.95	56	24
4.4.3	VYPG (0.47)	1	18x18 (6.5)	12.8 (3.2)	0.0036	0.0038	2.29	0.95	59	24
4.4.3	05PC (1.08)	1	18x18 (6.5)	12.8 (2.8)	0.013	0.017	0.91	0.93	60	25
4.4.3	15PC (1.23)	1	18x18 (6.5)	12.8 (2.7)	0.017	0.022	1.02	0.94	61	37
4.4.3	15PC (1.23)	9	25x25 (7.2)	5 (2.8)	0.0037	0.0037	12.09	3.38	77	30
5.4.2	MCE (100 nm)	1	14x14 (4.5)	11.5 (0.5)	-	-	0.61	0.94	58	25
5.4.2	MCE (100 nm)	1	14x14 (4.5)	11.5 (0.1)	-	-	0.31	0.98	42	25
5.4.2	MCE (50 nm)	1	14x14 (4.5)	11.5 (0.5)	-	-	0.85	0.98	59	25
5.4.2	MCE (50 nm)	1	14x14 (4.5)	11.5 (0.1)	-	-	0.31	1.00	46	25
5.4.2	MCE (25 nm)	1	14x14 (4.5)	11.5 (0.5)	-	-	1.04	0.94	56	24
5.4.2	MCE (25 nm)	1	14x14 (4.5)	11.5 (0.1)	0.4	0.93	0.62	1.35	54	25

single stage Knudsen pump with 48 mm diameter and 2.3 mm thick zeolite disc resulted in a gas flow rate of ≈0.12 sccm with a temperature bias of 33 K. The gas flow rate generated was higher than the gas flow rates reported in past from Knudsen pumps of comparable size operating at atmosphreric pressure. However, analysis suggested that the zeolite disc had an effective leak aperture of about 35 μm, which limited its pressure head generation capability. Subsequently, three synthetic nanoporous ceramics – 05PC, 15PC, and VYPG – were studied for their thermal transpiration driven gas flow characteristics (Chapter 4). The clay based ceramic 15PC was identified as the most preferred material for generating high pressure heads, while allowing reasonable gas flow rates. 15PC had the largest nanopore diameter, which allowed it to support highest thermal transpiration driven flow under a given operating condition. The fitted model suggested that in 15PC also had the largest leak aperture diameter. However, the increase in pumping due to large pore size dominates the increased leakage flow. This suggests that large nanopore diameters that provide higher transpiration flow may allow us to tolerate larger leak apertures.

Polymer membranes with varying pore sizes (25 nm, 50 nm, and 100 nm) and thickness were also evaluated for Knudsen pumps (Chapter 5). These membranes had larger pore sizes than the nanoporous ceramics, so they could support a higher gas flow rate. The polymer membrane with pore size 25 nm was identified as the preferred membrane for future efforts on Knudsen pumps targeting high flow rate and high pressure generation capabilities. Its isothermal pressure driven gas flow characteristics were almost identical to ideal defect free values, which suggested that the pore size and the percent porosity had minimal variation from the corresponding nominal values. The

membrane with 25 nm pore size allowed transitional gas flow at atmospheric pressure, which was favorable for generating high gas flow rates. A Knudsen pump using this membrane as the transpiration material resulted in a gas flow rate of 0.44 sccm against a pressure of 330Pa and a no (external) load gas flow rate was estimated to be 0.93 sccm. Moreover, since it had the smallest pore size amongst the three types of membranes, it resulted in highest pressure heads.

Lifetime performance evaluation tests are being done on some of the Kndusen pumps discussed in this effort. The 9-stage Knudsen pump has been demonstrated to run continuously for more than 7000 hours without any deterioration in its performance. A polymer based Knudsen pump SSKP1 has also been demonstrated to run continuously for 600 hours without any noticeable deterioration in its performance. Some minor variations in the flow rate were observed, primarily due to the variation in ambient operating temperature of the device.

In addition to the specific findings discussed above this work has made two major contributions that may have long term impact on the design and development of Knudsen pump:

1) Nanoporous ceramic and polymer membranes have been introduced for thermal transpiration driven Knudsen pumping. These membranes have well controlled pore sizes and have low thermal conductivity. Therefore, they are useful for generating reasonable gas flow rates while limiting the parasitic heat loss from the device. Further, these membranes have thickness on the order of 100 μm, which allow the integration and processing of these membranes using conventional microfabrication processes. A single stage Knudsen pump (footprint ≈14x14 mm^2) based on these membranes was

demonstrated to generate a no load gas flow rate of about 1 sccm for an input power of about 1.4 W. These pumps were also demonstrated to pump continuously in excess of 7000 hours without any significant loss in their pumping capability.

2) A semi-analytical system level model was introduced that can be used to identify and quantify various non-idealities in the Knudsen pumps. In addition, the model allows us to predict the performance of the pump, if the non-idealities can be partially/fully rectified. This model allows us to have a system level understanding of the function of the Knudsen pump and gives us an insight into how the design can be improved to achieve the desired performance metrics.

6.2 Future Work

Although the work described here resulted in unprecedented gas flow rates using bulk nanoporous materials, more work remains to be done to meet all the current needs of microsystem. The long term target remains a Knudsen pump that can deliver gas flow rates ≈25 sccm @ pressure head 20 kPa and ≈2 sccm @ pressure head 50 kPa, required for the micro gas chromatograph under development at The University of Michigan. The device designs/architectures documented in the chapters 3, 4, and 5 can be adapted easily to meet the gas pumping requirements of a wide range of microsystems.

As demonstrated in Chapter 4, high pressure head generation would require multiple stages cascaded in series. A low pressure head across each of the stages allows us to limit the leakage back flow across the transpiration elements.

It might be possible to reduce the overall size of the Knudsen pumps by using microfabrication processes; however, defect free integration of the bulk nanoporous

material to the microfabrication based fabrication process will be a challenge. Efforts will be required to explore the feasibility and methodology of integrating bulk nanoporous material into the microfabricated structure for multistage Knudsen pump.

Another avenue that remains to be explored is the possibility of improving the thermal efficiency of the Knudsen pumps, in general. Thermal efficiency can be improved by effective thermal isolation of the heater used in these Knudsen pump. Microfabrication techniques can potentially be useful in achieving high thermal isolations. Thermal isolations as high as 10^5 W/K have been demonstrated by McNamara, *et al.* [McN05].

In addition to the research directions proposed above, a study of the statistical variation in the performance of these devices will be useful. As mentioned in the section 5.4.2B, the performance of some of the Knudsen pumps deviates from the predicted trends because of the variation in the non-idealities from device to device. It would be useful to fabricate several pumps of each kind and study the statististical distribution in their performance. The average behavior of each kind of pump is expected to follow the predicted trends; and variation in their performance will be representative of the uncertainity introduced in the performance of these pumps due to various non-idealities.

One possible cause of device-to-device variation is the statistical distribution of porosity and pore sizes. A more accurate estimate of some of these non-idealities may require use of specilized metrology techniques.

APPENDICES

APPENDIX A

DETAILED EXPERIMENTAL SET-UP

This appendix presents a detailed overview of the experimental set-up used for estimating the thermal transpiration driven gas flow characteristics of a Knudsen pump. It presents a exhaustive list of various equipments used in the test set-up and illustrates how each of these equipments are connected.

Figures A.1 and A.2 show detailed schematics of the experimental test set-ups used to characterize the Knudsen pumps (KP), discussed in Chapters 3, 4 and 5, operating at and below atmospheric pressure. The bottom facet of the Knudsen pump is kept in thermal equilibrium with a heat sink (HS) – a metallic block with large thermal mass maintained at room temperature. A silver grease (SG) is used for effective thermal coupling of the Knudsen pump with the heat sink. The device is tested in both modes: pressure mode and flow mode. While operating in pressure mode, a pressure sensor (PS) is attached at the sealed outlet (O) and the inlet (I) is left open to the ambient. In order to test these devices at sub-atmospheric pressures, the KP is placed in a controlled vacuum chamber (CPC) (as shown in Fig. 5.7). The pressure inside CPC and hence the ambient operating pressure of the KP is regulated externally.

For flow mode testing – a clear flexible tubing (CT) with water plugs (WP), and a pressure sensor are connected to the outlet of the pump through a T-joint; and the inlet is kept open to ambient (Fig. A.2).

Thermocouples (TC1 and TC2), attached to the hot and the cold chamber of the Knudsen pump, are used to record the applied temperature gradient across the nanoporous ceramic. The voltage output from the two thermocouples and the pressure sensor are read into HP34401A multimeters. The multimeters are further connected to a PC running a Labview program through a National Instruments GPIB-USB-HS data transfer cable to record the temporal variation of the voltage outputs.

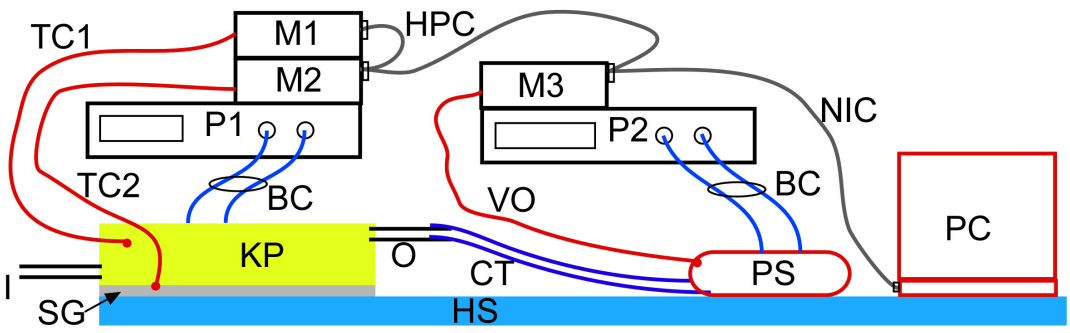

BC : Banana cables for connecting to power supply
CT : Clear tygon tubing
HPC: HP 10833B GPIB cables
HS : Heat Sink (Optic Table in EEC1000)
I : Inlet of KP
KP : Knudsen Pump
M1-3: Multimeters (HP 34401A)
NIC : National Instruments GPIB-USB-HS cable
O : Outlet of KP
PS : Pressure sensor (Part# MPXM2053D from Freescale Semicondictors)
PC : Laptop running labview program
P1-2: Power supplies (HP E3630A)
SG : Silver Grease
TC1 : K-type thermocouple in the hot chamber of KP (Part# 5SRTC-TT-K-40-36 from Omega Technologies)
TC2 : K-type Thermocouple in the cold chamber of KP (Part# 5SRTC-TT-K-40-36 from Omega Technologies)
VO : Output voltage from pressure sensor

Fig. A.1: Schematic of the pressure mode test set-up for Knudsen pump operating at and below atmospheric pressure. For sub-atmospheric pressure operation, the Knudsen pump is placed in a controlled pressure chamber.

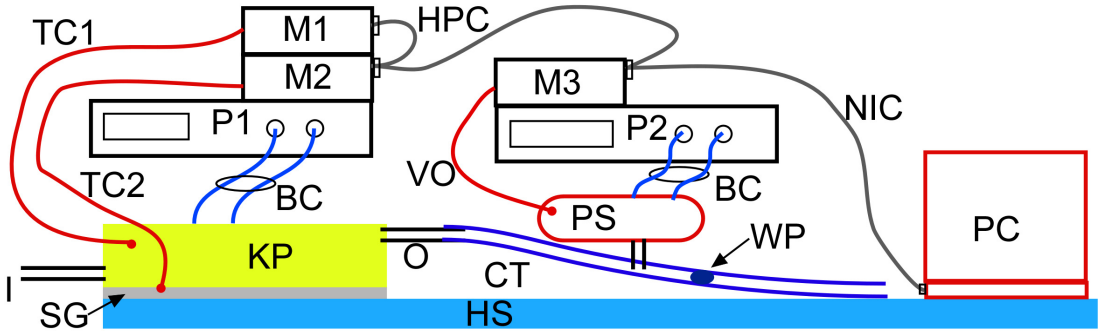

BC : Banana cables for connecting to power supply
CT : Clear tygon tubing
HPC: HP 10833B GPIB cables
HS : Heat Sink (Optic Table in EEC1000)
I : Inlet of KP
KP : Knudsen Pump
M1-3: Multimeters (HP 34401A)
NIC : National Instruments GPIB-USB-HS cable
O : Outlet of KP
PS : Pressure sensor (Part# MPXM2053D from Freescale Semicondictors)
PC : Laptop running labview program
P1-2: Power supplies (HP E3630A)
SG : Silver Grease
TC1 : K-type thermocouple in the hot chamber of KP (Part# 5SRTC-TT-K-40-36 from Omega Technologies)
TC2 : K-type Thermocouple in the cold chamber of KP (Part# 5SRTC-TT-K-40-36 from Omega Technologies)
VO : Output voltage from pressure sensor
WP : Water plug used to measure the gas flow generated at the outlet

Fig. A.2: Schematic of the flow mode test set-up for Knudsen pump operating at atmospheric pressure.

APPENDIX B

FITTED MODELS: MATLAB CODES

B.1 Fitted model for single stage Knudsen pump in Chapter 4

Main Program

```
clc
clear all

tic
% % IMPORTING EXP DATA
TPexp
len = length(TPdata);
dumm = min(TPdata(len,1),TPdata(len,3));
tmax = floor(min(dumm,TPdata(len,5)));
dumm = min(TPdata(1,1),TPdata(1,3));
tmin = floor(min(dumm,TPdata(1,5)));
tchg1 = 804.6;
tchg2 = 2868.4;


% % Importing QT and QP data
QTQPsha

NPdia = 1.23e-9; %% Diameter of the nanopores
a = NPdia/2;  %% radius of nanopores
por = 0.32; %% void fraction in the nanoporous ceramics

% % FITTED PARAMETERS
fThH = 5.5;
fThC = 8;

DleakH = 20e-6;
DleakC = 20.5e-6;

fDELTh = 0.51;

ftr = 0.2;
% % % NEXT GOOD CHOICE

HTRtauH = 61.81;
```

```
HTRtauC = 70.97;
delThH = 38.71;
delThC = 38.94;

AIRtauH = HTRtauH * fThH;
AIRtauC = HTRtauC * fThC;

DThH = fDELTh * delThH;
DThC = fDELTh * delThC;

% % % CONSTANTS
Dcoll = 3.7e-10;  %% Collision diameter of air
kB = 1.38e-23;  %% Boltzmann Constant
M_air = 2.87e-2;  %% Molecular mass of air
NA = 6.023e23;  %% Avagadro number
m_air = M_air/NA;  %% Mass of one molecule of air
Rg = kB*NA; %% Universal Gas Constant
R = Rg/M_air; %%Gas Constant

% % % CHOOSEN PARAMETERS
tstep1 = 0.2;
tlim = tstep1/2;

vol1 = 0.01*(7.8+13.5+44+10.5)*0.25*pi*(0.05*0.0254)^2; %% vol of
flexible tubing 0.05" ID
vol2 = 0.01*(3+3.5+5+10+4.5)*0.25*pi*(0.001615)^2; %% vol of steel
tubing 0.001615 m ID
vol3 = 17*17*(2.745-2)*1e-9 - 0.25*pi*15^2*(2.745-2)*1e-9; %% dead
volume between the nanoporous disc and top cap
vol = ftr*(vol1+vol2+vol3);   %%vol of hot chamber
Pamb = 98125;   %% Ambient pressure = 736 torr
Tamb = min(min(TPdata(:,4)), min(TPdata(:,6)));  %% Ambient temperature
CERdia = 12.75e-3; %% diameter of ceramic disc
CERthk = 2.745e-3; %% thickness of ceramic disc
Pc = Pamb;

t1 = tmin;
t2 = tmin;
t = tmin;

Ph1 = interp1(TPdata(:,1),TPdata(:,2),t1,'cubic') + Pamb;
Th1 = interp1(TPdata(:,3),TPdata(:,4),t1,'cubic');
Th1 = Tamb + fDELTh*(Th1-Tamb);
Tc1 = interp1(TPdata(:,5),TPdata(:,6),t1,'cubic');
N1 = Ph1*vol/(Rg*Th1);
Th1air = Th1;

Ph2 = Ph1;
Th2 = Th1;
Tc2 = Tc1;
N2 = N1;
Th2air = Th1air;

htr = 0;
Phfit = Ph1;
```

```
Thot = Th1;
Tcold = Tc1;
time = t1;
ThotAIR = Th1air;
Phexp = Ph1;
Thexp = Th1;

tinit = t1;
Tinit = Tc1;

% % % % test arrays
prn = [];
pl_data = [];

% % PROCESSING
while t < tmax%%tmin+10*tstep%%

    if (t/1000 - floor(t/1000)) < 1e-10
        t
    end

    t1 = t;
    t2 = t+tstep1;
    Ph1 = Ph2;
    Th1 = Th2;
    Tc1 = Tc2;
    N1 = N2;
    Th1air = Th2air;

    t = t2;
    tstep = t2-t1;

    if t <= tchg1+tlim   %%% somehow the program does not enter this
loop for t = tchg1... so add 0.1!!
        tinit = t2;
        htr = 0;
        Dleak = DleakC;
        AIRtau = AIRtauC;
%         CERtau = CERtauC;
        delTh = 0;
%         delTc = 0;
        Thinit = interp1(TPdata(:,3),TPdata(:,4),tinit,'cubic');
        Thinit = Tamb + fDELTh*(Thinit-Tamb);
%         Tcinit = interp1(TPdata(:,5),TPdata(:,6),tinit,'cubic');
        Th2air = Thinit + htr*delTh*(1-exp(-(t2-tinit)/AIRtau));
%         Tc2 = Tcinit + htr*delTc*(1-exp(-(t2-tinit)/CERtau));
        Thlast1 = Th2air;
%         Tclast1 = Tc2;
    elseif t>tchg1+tlim && t<=tchg2+tlim
        tinit = tchg1;
        %         Tinit =
interp1(TPdata(:,3),TPdata(:,4),tinit,'cubic');
        Thinit = Thlast1;
%         Tcinit = Tclast1;
        delTh = DThH;
```

```
%         delTc = DTcH;
        htr = 1;
        Dleak = DleakH;
        AIRtau = AIRtauH;
%         CERtau = CERtauH;
        Th2air = Thinit + htr*delTh*(1-exp(-(t2-tinit)/AIRtau));
%         Tc2 = Tcinit + htr*delTc*(1-exp(-(t2-tinit)/CERtau));
        Thlast2 = Th2air;
%         Tclast2 = Tc2;
    elseif t>tchg2+tlim
        tinit = tchg2;
        %         Tinit =
interp1(TPdata(:,3),TPdata(:,4),tinit,'cubic');
        Thinit = Thlast2;
%         Tcinit = Tclast2;
        delTh = DThC;
%         delTc = DTcC;
        htr = -1;
        Dleak = DleakC;
        AIRtau = AIRtauC;
%         CERtau = CERtauC;
        Th2air = Thinit + htr*delTh*(1-exp(-(t2-tinit)/AIRtau));
%         Tc2 = Tcinit + htr*delTc*(1-exp(-(t2-tinit)/CERtau));
    end

    Th2 = interp1(TPdata(:,3),TPdata(:,4),t2,'cubic');
    Thexp = [Thexp
        Th2];
    Thtmp = Th2;
    Th2 = Tamb + fDELTh*(Th2-Tamb);
    Tc2 = interp1(TPdata(:,5),TPdata(:,6),t2,'cubic');
    Phexp2 = interp1(TPdata(:,1),TPdata(:,2),t2,'cubic') + Pamb;
    Th = (Th1+Th2)/2;
    Tc = (Tc1+Tc2)/2;
    Tavg = (Th+Tc)/2;
    DTDx = (Th-Tc)/CERthk;
    DThDt = (Th2-Th1)/tstep;

    Phint2 = (Ph1/Th1air)*Th2air;
    Phavg2 = (Phint2+Ph1)/2;
    Ph = Phavg2;
    Pavg = (Ph+Pc)/2;
    delP = Phavg2-Pamb;  %% equals Ph-Pc
    DPDx = delP/CERthk;


    % %     mean free path
    mfp = mfpath(kB, Tavg, Dcoll, Pavg);

    % % average velocity
    u_bar = meanvel(R, Tavg);
% % % % % % %     function u_bar = meanvel(R, Tavg)
% % % % % % %     u_bar = (8*R*Tavg/pi)^0.5;

    % % Molecules per unit volume
    N = moldens(kB, Pavg, Tavg);
```

```
% % % % % % %     function N = moldens(kB, Pavg, Tavg)
% % % % % % %     N = Pavg/(kB*Tavg);

    % % Dynamic Viscosity
    mu = visc(N, m_air, u_bar, mfp);
% % % % % % %     function mu = visc(N, m_air, u_bar, mfp)
% % % % % % %     mu = 0.5 * N* m_air* u_bar* mfp;

    % % density
    rho = dens(N, m_air);
% % % % % % %     function rho = dens(N, m_air)
% % % % % % %     rho = N*m_air;

    % % DEL - ???
    del = rarpar(a, Dcoll, Pavg, kB, Tavg);
% % % % % % %     function del = rarpar(a, Dcoll, Pavg, kB, Tavg)
% % % % % % %     del = (0.5*pi^3)^0.5 * a* Dcoll^2 * Pavg/(kB* Tavg);

    % % Flow coefficients
    [QT QP] = QTQPcalc(del, QTQPdata);

    % % Mas flow through each pore
    Mdot1 = massflo(QT, QP, Th, Tc, Tavg, Ph, Pc, Pavg, a, CERthk,
m_air, kB);

    % % Number of pores
    Npores = CERdia^2 * por/NPdia^2;
    % % Total mass flow
    MdotTT = Mdot1*Npores;
    % % Flow rate in ccm
    QccmTT = (MdotTT/rho)*1e6*60;
    % % Rate of movement of gas molecules
    ndotTT = MdotTT/m_air;
    % % Rate of movement of number of moles/sec
    NdotTT = ndotTT/NA;

    % %     Poiseuille flow across leak aperture
    QL = posflo(Dleak, DPDx, mu);
% % % % % % %     function QL = posflo(Dleak, DPDx, mu)
% % % % % % %     QL = pi*Dleak^4*DPDx/(128*mu);

    % %     Mass of leaked gas
    MdotL = QL*rho;
    % %     Number of moles of leaked air
    NdotL = MdotL/M_air;

    delN = (NdotTT - NdotL)*tstep;

    N2 = N1 + delN;

    Ph2 = (Phint2/N1)*N2;

    Phfit = [Phfit
        Ph2];
```

```
    time = [time
        t2];
    Thot = [Thot
        Th2];
    Tcold = [Tcold
        Tc2];
    ThotAIR = [ThotAIR
        Th2air];
    Phexp = [Phexp
        Phexp2];
    % %

    pl_data = [pl_data
        [t2 Phexp2 Ph2 Thtmp Th2 Th2air Tc2]];
end

[RMSE stdDEV] = RMSEcalc(Phfit, Phexp)

obj_fn = ((RMSE-0)^2 + (stdDEV-0)^2)^0.5  %% target to reduce RMSE to 0
and stdDEV to 0

tEND = toc
Pemx = max(Phexp)
Prmx = max(Phfit)
tmx = tmax
stats = [RMSE tmx tEND Pemx/1000 Prmx/1000 NPdia*1e9 por*100]


figure(1)
plot(time, ThotAIR,'-r')
hold on
plot(time, Thot,'-k')
plot(TPdata(:,3),TPdata(:,4))
h = legend('ThotAIR','Thot','Thexp',1);
set(h,'Interpreter','none')
xlabel('Time (s)');
ylabel('Temperature (K)');
hold off

figure(2)
plot(time, Tcold,'-r')
hold on
plot(TPdata(:,5),TPdata(:,6))
h = legend('TcoldCER','Tcexp',1);
set(h,'Interpreter','none')
xlabel('Time (s)');
ylabel('Tcold (K)');
hold off

figure(3)
plot(time, Phfit,'-r')
hold on
plot(TPdata(:,1),TPdata(:,2)+Pamb)
h = legend('Phfit','Phexp',1);
set(h,'Interpreter','none')
```

```
xlabel('Time (s)');
ylabel('Phot (Pa)');
hold off
```

Subroutines

mfpath.m

```
function mfp = mfpath(kB, Tavg, Dcoll, Pavg)
mfp = kB*Tavg/(2^0.5 * pi * Dcoll^2 * Pavg);
```

meanvel.m

```
function u_bar = meanvel(R, Tavg)
u_bar = (8*R*Tavg/pi)^0.5;
```

moldens.m

```
function N = moldens(kB, Pavg, Tavg)
N = Pavg/(kB*Tavg);
```

visc.m

```
function mu = visc(N, m_air, u_bar, mfp)
mu = 0.5 * N* m_air* u_bar* mfp;
```

dens.m

```
function rho = dens(N, m_air)
rho = N*m_air;
```

rarpar.m

```
function del = rarpar(a, Dcoll, Pavg, kB, Tavg)
del = (0.5*pi^3)^0.5 * a* Dcoll^2 * Pavg/(kB* Tavg);
```

QTQPcalc.m

```
function [QT QP] = QTQPcalc(del, QTQPdata)
delta = QTQPdata(:,1);
QP0p6 = QTQPdata(:,2);
QT0p6 = QTQPdata(:,3);
QP0p8 = QTQPdata(:,4);
QT0p8 = QTQPdata(:,5);
QP1p0 = QTQPdata(:,6);
QT1p0 = QTQPdata(:,7);
QP = interp1(delta, QP0p8, del, 'cubic');
QT = interp1(delta, QT0p8, del, 'cubic');
```

Massflo.m

```
function Mdot1 = massflo(QT, QP, Th, Tc, Tavg, Ph, Pc, Pavg, a,
CERthk, m_air, kB)
Mdot11 = QT*(Th-Tc)/Tavg - QP*(Ph-Pc)/Pavg;
Mdot12 = pi * a^3 * Pavg / CERthk;
Mdot13 = (m_air/(2*kB*Tavg))^0.5;
Mdot1 = Mdot11* Mdot12* Mdot13; %%* test
```

Posflo.m

```
function QL = posflo(Dleak, DPDx, mu)
QL = pi*Dleak^4*DPDx/(128*mu);
```

RMSEcalc.m

```
function [RMSE stdDEV] = RMSEcalc(Phfit, Phexp)
```

```
SQsum = 0;
sum = 0;
leng = length(Phfit);
for i = 1:leng
    SQsum = SQsum + (Phfit(i) - Phexp(i))^2;
    sum = sum + abs(Phfit(i) - Phexp(i));
end
RMSE = (SQsum/leng)^0.5;
avg = sum/leng;
SD = 0;
for i = 1:leng
    SD = SD + (abs(Phfit(i) - Phexp(i)) - avg)^2;
end
stdDEV = (SD/leng)^0.5;
```

B.2 Fitted model for multi stage Knudsen pump in Chapter 4

Main Program

```
clc
clear all

% % format long
tic
% % IMPORTING EXP DATA
TPexp
len = length(TPdata);
dumm = min(TPdata(len,1),TPdata(len,3));
tmax = floor(min(dumm,TPdata(len,5)));
dumm = min(TPdata(1,1),TPdata(1,3));
tmin = floor(min(dumm,TPdata(1,5)));
tchg1 = 344.235;
tchg2 = 19732.63;
nstg = 9;

% % tmax = 20*tchg1;
% % tmax = 10000
% % Importing QT and QP data
QTQPsha
delta = QTQPdata(:,1);
QP0p6 = QTQPdata(:,2);
QT0p6 = QTQPdata(:,3);
QP0p8 = QTQPdata(:,4);
QT0p8 = QTQPdata(:,5);
QP1p0 = QTQPdata(:,6);
QT1p0 = QTQPdata(:,7);

NPdia = 1.23e-9; %% Diameter of the nanopores
por = 0.32; %% void fraction in the nanoporous ceramics

% % PARAMETERS
% % % % % time constants for heating and cooling air in hot chambers
dumm = 1.4;  %% factor time constt for air-heating
fThH = [dumm dumm dumm dumm dumm dumm dumm dumm  2.3];
% % %% factor time constant for air -cooling
```

```
dumm = 1.4;
fThC = [dumm dumm dumm dumm dumm dumm dumm dumm 2.3];
dumm = 14.7; %% leak dia - heating
DleakH = [dumm dumm dumm dumm dumm dumm dumm dumm 19.5]*1e-6;
% % %% leak dia -cooling
dumm =14.7;
DleakC = [dumm dumm dumm dumm dumm dumm dumm dumm 19.5]*1e-6;
dumm = 0.85; %% fraction of air that gets heated
ftr = [dumm dumm dumm dumm dumm dumm dumm dumm 0.17];
% % fraction of temp drop actoss ceramic
dumm =0.93;
fDELTh = dumm*[0.95 0.95 0.95 1 1 1 0.95 0.95 0.95];
% %  volume of the chambers
vol1 = 12e-9*1; %% interconnecting vol. between two stages
vol2 = 15e-7*1; %% vol encapsulated at outlet - press. sensor
vol = [vol1 vol1 vol1 vol1 vol1 vol1 vol1 vol1 vol2];
vol = vol.*ftr;

% % % % % % % % % % % % % % % % % % %     END Fitted parameters
HTRtauH = 89.97;
HTRtauC = 93.94;
delThH = 54.2237;
delThC = 53.899;
AIRtauH = HTRtauH * fThH;
AIRtauC = HTRtauC * fThC;
DThH = fDELTh * delThH;
DThC = fDELTh * delThC;

Dcoll = 3.7e-10;  %% Collision diameter of air
kB = 1.38e-23;  %% Boltzmann Constant
M_air = 2.87e-2;  %% Molecular mass of air
NA = 6.023e23;  %% Avagadro number
m_air = M_air/NA;  %% Mass of one molecule of air
Rg = kB*NA; %% Universal Gas Constant
R = Rg/M_air; %%Gas Constant
Pamb = 98125;   %% Ambient pressure = 736 torr
Tamb = min(min(TPdata(:,4)), min(TPdata(:,6)));  %% Ambient temperature
a = NPdia/2;  %% radius of nanopores
CERdia = 5e-3; %% diameter of ceramic disc
CERthk = 2.9e-3; %% thickness of ceramic disc

% % % CHOOSEN PARAMETERS

tstep = 0.2;
tlim = tstep/2;
time = (tmin:tstep:tmax)';
stps = length(time);
Phexp = interp1(TPdata(:,1),TPdata(:,2),time,'cubic')+Pamb;
Thexp = interp1(TPdata(:,3),TPdata(:,4),time,'cubic');
Tcexp = interp1(TPdata(:,5),TPdata(:,6),time,'cubic');
Thot = Tamb + (Thexp-Tamb)*fDELTh;  %%temperature at the top surface of
the ceramics
Tcold = zeros(stps,nstg);
pl_data = [];
dumm = ones(1,9);
Tcold = Tcexp*dumm;
```

```
Thair = Thot; %% intialization of Thair
Nmole = zeros(stps,nstg);
t = 0;
for i = 1:stps
    t = time(i);
    if t <= tchg1+tlim   %%% somehow the program does not enter this
loop for t = tchg1... so add 0.1!!
        tinit = t;
        htr = 0;
        AIRtau = AIRtauC;
        delTh(1,1:nstg) = 0;
        Thinit = Thot(i,:);
        Thair(i,:) = Thinit + htr.*delTh.*(1-exp(-(t-tinit)./AIRtau));
        Thlast1 = Thair(i,:);
    elseif t>tchg1+tlim && t<=tchg2+tlim
        tinit = tchg1;
        Thinit = Thlast1;
        delTh(1,1:nstg) = DThH;
        htr = 1;
        AIRtau = AIRtauH;
        Thair(i,:) = Thinit + htr.*delTh.*(1-exp(-(t-tinit)./AIRtau));
        Thlast2 = Thair(i,:);
    elseif t>tchg2+tlim
        tinit = tchg2;
        Thinit = Thlast2;
        delTh(1,1:nstg) = DThC;
        htr = -1;
        AIRtau = AIRtauC;
        Thair(i,:) = Thinit + htr.*delTh.*(1-exp(-(t-tinit)./AIRtau));
    end
end

Th = (Thot(2:stps,:) + Thot(1:stps-1,:))/2;
Tc = (Tcold(2:stps,:) + Tcold(1:stps-1,:))/2;
Tavg = (Th+Tc)/2;
DTDx = (Th-Tc)/CERthk;
DThDt = (Thot(2:stps,:) - Thot(1:stps-1,:))/tstep;

Pr = zeros(stps,nstg+1);
Pr2 = zeros(stps-1,nstg+1);
Pavg = zeros(stps-1,nstg);
delP = zeros(stps-1,nstg);
Pr(:,1) = Pamb;
Pr(1,:) = linspace(Pamb,Phexp(1,1),10);
Nmole(1,:) = Pr(1,2:nstg+1).* vol./(Rg.*Tavg(1,:));

Npores = CERdia^2*por/NPdia^2;
for i = 2:stps
    t = time(i);
    if (t/1000 - floor(t/1000)) < 1e-10
        time(i)
    end

    if t <= tchg1+tlim   %%% somehow the program does not enter this
loop for t = tchg1... so add 0.1!!
        Dleak = DleakC;
```

```
    elseif t>tchg1+tlim && t<=tchg2+tlim
        Dleak = DleakH;
    elseif t>tchg2+tlim
        Dleak = DleakC;
    end
    % %     store intermediate pressure in next row of Pr
    rat = ftr./(1-ftr);
    Nr = rat./Thair(i-1,1:nstg) + 1./Tcold(i-1,1:nstg);
    Dr = rat./Thair(i,1:nstg) + 1./Tcold(i,1:nstg);
    Nr(1,nstg) = rat(1,nstg)/Thair(i-1,nstg) + 1/Tamb;
    Dr(1,nstg) = rat(1,nstg)/Thair(i,nstg) + 1/Tamb;
    % %OLD % %     Pr(i,2:nstg+1) = Pr(i-1,2:nstg+1)./Thair(i-
1,1:nstg).*Thair(i,1:nstg);
    Pr(i,2:nstg+1) = Pr(i-1,2:nstg+1) .* Nr ./ Dr;
    % %     create a new matrix that averages the intial pressure an
    % intermediate pressure.  This is used as hot and cold pressure for
thermal
    % transpiration
    Pr2(i-1,:) = (Pr(i-1,:) + Pr(i,:))/2;
    % %     this is the average for thermal transpiration across each
individual disc.
    Pavg(i-1,:) = (Pr2(i-1,1:nstg) + Pr2(i-1,2:nstg+1))/2;
    % %     pressure drop across each disc
    delP(i-1,:) = (Pr2(i-1,2:nstg+1) - Pr2(i-1,1:nstg));
    DPDx = delP/CERthk;
    % %     mean free path
    mfp = (kB*Tavg(i-1,:))./(2^0.5 * pi * Dcoll^2 * Pavg(i-1,:));
    % % average velocity
    u_bar = (8*R*Tavg(i-1,:)/pi).^0.5;
    % % Molecules per unit volume
    N = Pavg(i-1,:)./(kB*Tavg(i-1,:));
    % % Dynamic Viscosity
    mu = 0.5 .* N.* m_air.* u_bar.* mfp;
    % % density
    rho = N.*m_air;
    % % DEL - rarefaction parameter
    del = (0.5*pi^3)^0.5 .* a.* Dcoll^2 .* Pavg(i-1,:)./(kB* Tavg(i-
1,:));
    % % Flow coefficients
    QP = interp1(delta, QP0p8, del, 'cubic');
    QT = interp1(delta, QT0p8, del, 'cubic');
    % % Mas flow through each pore
    dumm1 = (QT.*DTDx(i-1,:)./Tavg(i-1,:) - QP.*DPDx(i-1,:)./Pavg(i-
1,:)).* pi .* a^3 .* Pavg(i-1,:);
    dumm2 = (m_air./(2.*kB.*Tavg(i-1,:))).^0.5;
    Mdot1 = dumm1 .* dumm2; %%* test
    % % Total mass flow
    MdotTT = Mdot1*Npores;
% %     % % Flow rate in ccm
% %     QccmTT = (MdotTT./rho)*1e6*60;
% %     % % Rate of movement of gas molecules
% %     ndotTT = MdotTT/m_air;
% %     % % Rate of movement of number of moles/sec
    NdotTT = MdotTT./M_air;
    % %     Poiseuille flow across leak aperture
    QL = pi.*Dleak.^4.*DPDx(i-1,:)./(128.*mu);
```

```
    % %     Mass of leaked gas
    MdotL = QL.*rho;
    % %     Number of moles of leaked air
    NdotL = MdotL./M_air;

    delN(1,1:nstg-1) = (NdotTT(1,1:nstg-1) - NdotL(1,1:nstg-1)-
NdotTT(1,2:nstg) + NdotL(1,2:nstg))*tstep;
    delN(1,nstg) = (NdotTT(1,nstg) - NdotL(1,nstg))*tstep;

% %     ****correc this for gas moving out into the next stage???

    Nmole(i,:) = Nmole(i-1,:)+delN;
    Pr(i,2:nstg+1) = Pr(i,2:nstg+1) ./ Nmole(i-1,:) .* Nmole(i,:);

    if (t - floor(t)) < 1e-10
        pl_data = [pl_data
            [time(i) Phexp(i) Pr(i,nstg+1) Thexp(i) Thot(i,nstg)
Thair(i,nstg) Tcexp(i)]];
    end
end

Pemx = max(Phexp)
Prmx = max(Pr(:,nstg+1))
tmx = time(stps)
RMSE = (mean((Phexp-Pr(:,nstg+1)).^2))^0.5

figure(1)
plot(time,Phexp,'--r')
hold on
plot(time,Pr(:,nstg+1),'-k')
hold off

figure(2)
plot(time,Thexp,'--r')
hold on
plot(time,Thot(:,nstg),'-b')
plot(time,Thair(:,nstg),'-g')
hold off
tEND = toc
stats = [RMSE tmx tEND Pemx/1000 Prmx/1000 NPdia*1e9 por*100]
```

B.3 Fitted model for single stage Knudsen pump in Chapter 5

Main Program

```
clc
clear all
% % format long
tic
% % IMPORTING EXP DATA
TPexp
tdelay = 5; % (sec) propagation delay between the heater is turned On
and when the pressure sensor shows any response.
Pzerr = 13.5; %% zero error adjustmant of pressure sensor
```

```
len = length(TPdata);
dumm = min(TPdata(len,1),TPdata(len,3));
tmax = floor(min(dumm,TPdata(len,5))) - 5;
dumm = min(TPdata(1,1),TPdata(1,3));
tmin = floor(min(dumm,TPdata(1,5)));
% % Importing QT and QP data
QTQPsha

NPdia = 25e-9; %% Diameter of the nanopores
a = NPdia/2;  %% radius of nanopores
por = 0.7; %% void fraction in the nanoporous ceramics

% % FITTED PARAMETERS
Dleak = 19.9e-6;
fDELT = 0.1815;

% % % CONSTANTS
Dcoll = 3.7e-10;  %% Collision diameter of air
kB = 1.38e-23;  %% Boltzmann Constant
M_air = 2.87e-2;  %% Molecular mass of air
NA = 6.023e23;  %% Avagadro number
m_air = M_air/NA;  %% Mass of one molecule of air
Rg = kB*NA; %% Universal Gas Constant
R = Rg/M_air; %%Gas Constant

% % % CHOOSEN PARAMETERS
tstep1 = 0.05;
tlim = tstep1/2;

vol = 4.72e-7;   %%vol of hot chamber
Pamb = 99805.1;   %% Ambient pressure = 736 torr
Tamb = min(min(TPdata(:,4)), min(TPdata(:,6)));  %% Ambient temperature
CERdia = 11.5e-3; %% diameter of ceramic disc
CERthk = 0.105e-3; %% thickness of ceramic disc
Ph = Pamb;

t1 = tmin;
t2 = tmin;
t = tmin;

Pc1 = Pamb - interp1(TPdata(:,1),TPdata(:,2),t1+tdelay,'cubic')-Pzerr;
Th1 = interp1(TPdata(:,3),TPdata(:,4),t1,'cubic');
Thexp = Th1;
Tc1 = interp1(TPdata(:,5),TPdata(:,6),t1,'cubic');
Tcexp = Tc1;

Tavg1 = (Th1+Tc1)/2;
delT1 = (Th1-Tc1)*fDELT;

Th1 = Tavg1 + delT1/2;
Tc1 = Tavg1 - delT1/2;

N1 = Pc1*vol/(Rg*Tamb);

Pc2 = Pc1;
```

```
Th2 = Th1;
Tc2 = Tc1;
N2 = N1;

htr = 0;
Pcfit = Pc1;
Tcold = Tc1;
Thot = Th1;
time = t1;
Pcexp = Pc1;

tinit = t1;
Tinit = Tc1;

% % % % test arrays
prn = [];
pl_data = [];

% % PROCESSING
while t < tmax%%tmin+10*tstep%%

    if (t/100 - floor(t/100)) < 1e-4
        t
    end

    t1 = t;
    t2 = t+tstep1;
    Pc1 = Pc2;
    Th1 = Th2;
    Tc1 = Tc2;
    N1 = N2;

    t = t2;
    tstep = t2-t1;

    Th2 = interp1(TPdata(:,3),TPdata(:,4),t2,'cubic');
    Thexp = [Thexp
        Th2];
    Tc2 = interp1(TPdata(:,5),TPdata(:,6),t2,'cubic');
    Tcexp = [Tcexp
        Tc2];

    Tavg2 = (Th2+Tc2)/2;
    delT2 = (Th2-Tc2)*fDELT;

    Th2 = Tavg2 + delT2/2;
    Tc2 = Tavg2 - delT2/2;

    Pcexp2 = Pamb - interp1(TPdata(:,1),TPdata(:,2),t2+tdelay,'cubic')-
Pzerr;
    Th = (Th1+Th2)/2;
    Tc = (Tc1+Tc2)/2;
    Tavg = (Th+Tc)/2;
    DTDx = (Th-Tc)/CERthk;
```

```
    Ph = Pamb;
    Pc = Pc1;
    Pavg = (Ph+Pc)/2;
    delP = Ph-Pc;  %% equals Ph-Pc
    DPDx = delP/CERthk;

    % %     if t > 810
    % %         break;
    % %     end

    % %     mean free path
    mfp = mfpath(kB, Tavg, Dcoll, Pavg);
% % % % % % %     function mfp = mfpath(kB, Tavg, Dcoll, Pavg)
% % % % % % %     mfp = kB*Tavg/(2^0.5 * pi * Dcoll^2 * Pavg);

    % % average velocity
    u_bar = meanvel(R, Tavg);
% % % % % % %     function u_bar = meanvel(R, Tavg)
% % % % % % %     u_bar = (8*R*Tavg/pi)^0.5;

    % % Molecules per unit volume
    N = moldens(kB, Pavg, Tavg);
% % % % % % %     function N = moldens(kB, Pavg, Tavg)
% % % % % % %     N = Pavg/(kB*Tavg);

    % % Dynamic Viscosity
    mu = visc(N, m_air, u_bar, mfp);
% % % % % % %     function mu = visc(N, m_air, u_bar, mfp)
% % % % % % %     mu = 0.5 * N* m_air* u_bar* mfp;

    % % density
    rho = dens(N, m_air);
% % % % % % %     function rho = dens(N, m_air)
% % % % % % %     rho = N*m_air;

    % % DEL - ???
    del = rarpar(a, Dcoll, Pavg, kB, Tavg);
% % % % % % %     function del = rarpar(a, Dcoll, Pavg, kB, Tavg)
% % % % % % %     del = (0.5*pi^3)^0.5 * a* Dcoll^2 * Pavg/(kB* Tavg);

    % % Flow coefficients
    [QT QP] = QTQPcalc(del, QTQPdata);

    % % Mas flow through each pore
    Mdot1 = massflo(QT, QP, Th, Tc, Tavg, Ph, Pc, Pavg, a, CERthk,
m_air, kB);

    % % Number of pores
    Npores = CERdia^2 * por/NPdia^2;
    % % Total mass flow
    MdotTT = Mdot1*Npores;
    % % Flow rate in ccm
    QccmTT = (MdotTT/rho)*1e6*60;
    % % Rate of movement of gas molecules
```

```
    ndotTT = MdotTT/m_air;
    % % Rate of movement of number of moles/sec
    NdotTT = ndotTT/NA;

    % %     Poiseuille flow across leak aperture
    QL = posflo(Dleak, DPDx, mu);
% % % % % % %     function QL = posflo(Dleak, DPDx, mu)
% % % % % % %     QL = pi*Dleak^4*DPDx/(128*mu);

    % %     Mass of leaked gas
    MdotL = QL*rho;
    % %     Number of moles of leaked air
    NdotL = MdotL/M_air;

    delN = (NdotTT - NdotL)*tstep;

    N2 = N1 - delN;

    Pc2 = (Pc1/N1)*N2;

    Pcfit = [Pcfit
        Pc2];
    time = [time
        t2];
    Thot = [Thot
        Th2];
    Tcold = [Tcold
        Tc2];
    Pcexp = [Pcexp
        Pcexp2];
    % %
    % %     % % % % %     ARRAYS FOR TESTING THE COMPATIBILITY WITH
CALCULATION IN
    % %     % EXCEL SHEET
    % %
    % %     prn = [prn
    % %         t2 Th2 Tc2 Th2air Phint2 Phavg2 delP QL MdotL NdotL QT
QP MdotTT NdotTT delN N2 Ph2 DThDt];

    pl_data = [pl_data
        [t2 Pcexp2 Pc2 Th2 Tc2]];
end
fitDATA = [time Tcexp Tcold Thot Thexp Pcfit Pcexp];

[RMSE stdDEV] = RMSEcalc(Pcfit, Pcexp)

obj_fn = ((RMSE-0)^2 + (stdDEV-0)^2)^0.5;  %% target to reduce RMSE to
0 and stdDEV to 0

tEND = toc;
Pemn = min(Pcexp);
Prmn = min(Pcfit);
Prmn-Pemn
tmx = tmax;
stats = [RMSE tmx tEND Pemn/1000 Prmn/1000 NPdia*1e9 por*100];
```

```
% % tprn = {'t2' 'Th2' 'Tc2' 'Th2air' 'Phint2' 'Phavg2' 'delP' 'QL'
'MdotL' 'NdotL' 'QT' 'QP' 'MdotTT' 'NdotTT' 'delN' 'N2' 'Ph2' 'DThDt'};
% % xlswrite('test1', tprn);

figure(1)
plot(time, Thot,'-k')
hold on
% plot(TPdata(:,3),TPdata(:,4))
plot(time,Thexp);
% % h = legend('Thot','Thexp',1);
% % set(h,'Interpreter','none')
% % xlabel('Time (s)');
% % ylabel('Temperature (K)');
% % hold off
% %
% % figure(2)
plot(time, Tcold,'--r')
% % hold on
% % plot(TPdata(:,5),TPdata(:,6),'--g')
plot(time,Tcexp,'--g');
h = legend('TcoldCER','Tcexp',1);
set(h,'Interpreter','none')
xlabel('Time (s)');
ylabel('Temperature (K)');
hold off

figure(2)
plot(time, Pcfit,'-r')
hold on
plot(time,Pcexp)
% % plot(TPdata(:,1),Pamb - TPdata(:,2))
h = legend('Pcfit','Pcexp',1);
set(h,'Interpreter','none')
xlabel('Time (s)');
ylabel('Phot (Pa)');
hold off
```

Subroutines

mfpath.m

```
function mfp = mfpath(kB, Tavg, Dcoll, Pavg)
mfp = kB*Tavg/(2^0.5 * pi * Dcoll^2 * Pavg);
```

meanvel.m

```
function u_bar = meanvel(R, Tavg)
u_bar = (8*R*Tavg/pi)^0.5;
```

moldens.m

```
function N = moldens(kB, Pavg, Tavg)
N = Pavg/(kB*Tavg);
```

visc.m

```
function mu = visc(N, m_air, u_bar, mfp)
mu = 0.5 * N* m_air* u_bar* mfp;
```

dens.m

```
function rho = dens(N, m_air)
rho = N*m_air;
```

rarpar.m

```
function del = rarpar(a, Dcoll, Pavg, kB, Tavg)
del = (0.5*pi^3)^0.5 * a* Dcoll^2 * Pavg/(kB* Tavg);
```

QTQPcalc.m

```
function [QT QP] = QTQPcalc(del, QTQPdata)
delta = QTQPdata(:,1);
QP0p6 = QTQPdata(:,2);
QT0p6 = QTQPdata(:,3);
QP0p8 = QTQPdata(:,4);
QT0p8 = QTQPdata(:,5);
QP1p0 = QTQPdata(:,6);
QT1p0 = QTQPdata(:,7);
QP = interp1(delta, QP0p8, del, 'cubic');
QT = interp1(delta, QT0p8, del, 'cubic');
```

Massflo.m

```
function Mdot1 = massflo(QT, QP, Th, Tc, Tavg, Ph, Pc, Pavg, a,
CERthk, m_air, kB)
Mdot11 = QT*(Th-Tc)/Tavg - QP*(Ph-Pc)/Pavg;
Mdot12 = pi * a^3 * Pavg / CERthk;
Mdot13 = (m_air/(2*kB*Tavg))^0.5;
Mdot1 = Mdot11* Mdot12* Mdot13; %%* test
```

Posflo.m

```
function QL = posflo(Dleak, DPDx, mu)
QL = pi*Dleak^4*DPDx/(128*mu);
```

RMSEcalc.m

```
function [RMSE stdDEV] = RMSEcalc(Phfit, Phexp)
SQsum = 0;
sum = 0;
leng = length(Phfit);
for i = 1:leng
    SQsum = SQsum + (Phfit(i) - Phexp(i))^2;
    sum = sum + abs(Phfit(i) - Phexp(i));
end
RMSE = (SQsum/leng)^0.5;
avg = sum/leng;
SD = 0;
for i = 1:leng
    SD = SD + (abs(Phfit(i) - Phexp(i)) - avg)^2;
end
stdDEV = (SD/leng)^0.5;
```

Table B.1: Value of the temperature and pressure gas flow coefficients for different rarefaction parameters [Sha97].

δ	Q_P	Q_T	Q_P	Q_T	Q_P	Q_T
	α = 0.6	α = 0.6	α = 0.8	α = 0.8	α = 1.0	α = 1.0
0.0005	3.4875	1.7365	2.2484	1.1215	1.5023	0.7502
0.001	3.4751	1.7237	2.2437	1.1166	1.5008	0.7486
0.005	3.4001	1.6452	2.2131	1.0838	1.4904	0.7366
0.01	3.3374	1.5775	2.1853	1.053	1.48	0.7243
0.02	3.2488	1.4807	2.1442	1.007	1.4636	0.7042
0.03	3.1853	1.4093	2.1141	0.9719	1.4514	0.6884
0.04	3.1355	1.3512	2.0901	0.9432	1.4418	0.6752
0.05	3.0945	1.3036	2.0703	0.9186	1.4339	0.6637
0.06	3.0599	1.2617	2.0534	0.897	1.4273	0.6536
0.07	3.0299	1.2247	2.0388	0.8778	1.4217	0.6444
0.08	3.0037	1.1916	2.0259	0.8603	1.4168	0.6359
0.09	2.9805	1.1616	2.0145	0.8444	1.4127	0.6281
0.1	2.9597	1.1341	2.0043	0.8297	1.4101	0.621
0.2	2.8346	0.9435	1.9444	0.7244	1.3911	0.5675
0.3	2.771	0.8255	1.9169	0.6558	1.3876	0.5303
0.4	2.7367	0.7415	1.9056	0.605	1.392	0.5015
0.5	2.7184	0.6769	1.9033	0.5648	1.4011	0.4779
0.6	2.7101	0.625	1.9069	0.5315	1.413	0.4576
0.7	2.7085	0.582	1.9144	0.5031	1.427	0.4397
0.8	2.7117	0.5455	1.9248	0.4784	1.4425	0.4237
0.9	2.7183	0.514	1.9373	0.4567	1.4592	0.4092
1	2.7277	0.4865	1.9514	0.4372	1.4758	0.3959
1.2	2.7559	0.4402	1.9859	0.4035	1.5158	0.3721
1.4	2.7861	0.4029	2.0214	0.3754	1.555	0.3514
1.6	2.8201	0.3718	2.0593	0.3513	1.5956	0.333
1.8	2.8568	0.3456	2.0991	0.3303	1.6373	0.3165
2	2.8956	0.323	2.1402	0.3118	1.6799	0.3016
3	3.1074	0.2445	2.3585	0.2443	1.9014	0.2439
4	3.3342	0.1971	2.5881	0.2009	2.1315	0.2042
5	3.5677	0.1651	2.8233	0.1704	2.3666	0.1752
6	3.805	0.142	3.062	0.1479	2.6049	0.1531
7	4.0446	0.1245	3.303	0.1305	2.8455	0.1359
8	4.2858	0.1108	3.5455	0.1167	3.0878	0.122
9	4.5281	0.09979	3.7893	0.1055	3.3314	0.1106
10	4.7703	0.09079	4.0343	0.0962	3.5749	0.1014
20	7.2387	0.04746	6.5086	0.05104	6.0492	0.05426
30	9.7105	0.03187	8.9965	0.03452	8.5392	0.03685
40	12.185	0.02388	11.491	0.026	11.036	0.02785
50	14.656	0.01874	13.972	0.0208	13.495	0.02212

REFERENCES

[Abq07] P. Abgrall, and A.-M. Gue, "Lab-on-chip Technologies: Making a Microfluidic Network and Coupling it into a Complete Microsystem - A Review," *Journal of Micromechanics and Microengineering*, v. 17(5), pp. R15-R49, May 2007.

[Ahn95] C.H. Ahn, and M.G. Allen, "Fluid Micropumps based on Rotary Magnetic Actuators," *Proceedings of the 8th IEEE Micro Electro Mechanical Systems (MEMS'95)*, pp. 408-412, 1995.

[Ale05] A. A. Alexeenko, S. F. Gimelshein, E. P. Muntz, and A. D. Ketsdever, "Modeling of Thermal Transpiration Flows for Knudsen Compressor Optimization," *43rd AIAA Aerospace Sciences Meeting and Exhibit - Meeting Papers*, pp. 9419-9429, 2005.

[Ale06] A. A. Alexeenko, S. F. Gimelshein, E. P. Muntz, and A. D. Ketsdever, "Kinetic Modeling of Temperature Driven Flows in Short Microchannels," *International Journal of Thermal Sciences*, v 45(11), p 1045-51, Nov. 2006.

[Ark01] E. B. Arkilic, K. S. Breuer, M. A. Schmidt, "Mass flow and tangential momentum accommodation in silicon micromachined channels," *Journal of Fluid Mechanics*, v. 437, pp. 29-43, 2001.

[Ate03] J. Atencia, and D.J. Beebe, " An Oscillating Ferromagnetic Micropump Utilizing Centrifugal Force," *Proceedings of the 7th international Conference on Micro Total Analysis Systems (μTAS'03)*, pp. 883-886, 2003.

[Bes99] A. Beskok, and G. E. Karniadakis, "A model for flows in channels, pipes, and ducts at micro and nano scales," *Microscale Thermophysical Engineering*, v. 3(1), pp. 43-77, January/March 1999.

[Bha54] P. L. Bhatnagar, E. P. Gross, and M. Krook, "A Model for Collision Processes in Gasses," *Physical Reviews*, v. 94, pp. 511-524, 1954.

[Bir63] G. A. Bird, "Approach to Transitional Equilibrium in a Rigid Sphere Gas," Physics of Fluids, v. 6, pp.1518-1519, 1963.

[Bir78] G.A. Bird, "Monte Carlo Simulation of Gas flows," Annual Review of Fluid Mechanics, v. 10, pp. 11-31, 1978.

[Bir94] G. Bird, *Molecular Gas Dynamics and the Direct Simulation of Gas Flows,* Oxford, UK, 1994.

[Boh99] S. Bohm, W. Olthuis, and P. Bergveld, "A Plastic Micropump Constructed with Conventional Techniques and Materials," *Sensors and Actuators A*, v. 77, pp. 223-228, 1999.

[Cab01] C. Cabuz, W. R. Herb, E. I. Cabuz, and T. L. Son, " The Dual Diaphragm Pump," *Proceedings of the IEEE Micro Electro Mechanical Systems (MEMS)*, pp. 519-522, 2001.

[Cer75] C. Cercignani, *Theory and Application of the Boltzmann Equation*, Scottish Academic, Edinburgh and London, 1975.

[Cer06] C. Cercignani, *Slow rarefied Flows: Theory and Application to Micro-Electro-Mechanical Systems*, Birkhäuser Basel, 2006.

[Cha52] S. Chapman, and T. G. Cowling, *The mathematical Theory of Non-Uniform Gases*, Cambridge University Press, Cambridge., 1970.

[Cho09] T.V. Chokshi, A. Ben-Yakar, and N. Chronis, "CO2 and Compressive Immobilization of C. Elegans On-Chip," *Lab on a Chip*, v. 9, n. 1, pp. 151-157, 2009.

[Col04] S. Colin, P. Lalonde, and R. Caen, "Validation of Second-Order Slip Flow Model in Rectangular Microchannels," *Heat Transfer Engineering*, v. 25(3), pp. 23-30, 2004.

[Col05] S. Colin, "Rarefaction and Compressibility Effects on Steady and Transient gas Flows in Microchannels," *Microfluid Nanofluid*, vol. 1, no. 3, pp. 268-279, 2005.

[Dei64] R. G. Deissler, "An Analysis of Second Order Slip Flow and Temperature Jump Boundary Conditions for Rarefied Gases*," International Journal of Heat Mass Transfer*, v. 7, pp. 681-694, 1964.

[Dop97] J. Dopper, M. Clemens, W. Ehrfeld, K.P. Kamper, and H. Lehr, "Micro Gear Pumps for Dosing of Viscous Fluids," *Journal of Micromechanics and Microengineering*, v. 7, pp. 230-232, 1997.

[Ebe65] W. A. Ebert, and E. M. Sparrow, "Slip Flow in Annular and Rectangular Ducts," *Journal of Basic Engineering*, v. 87, pp. 1018-1024, 1965.

[Eli01] T. G. Elizavora, Y. V. Sheretov, "Theoretical and numerical investigation of Quasi-gasdynamic and Quasi-hydrodynamicEquations," *Computational Mathematical Physics*, v. 41(2), pp. 219-234, 2001.

[Fan99] J. Fan, and C. Shen, "Statistical Simulation of Low-Speed Unidirectional Flows in Transitional Regime," *R. Burn, R. Campargue, Rl Gatigno, J-C Lengrand (eds) Rarefied Gas Dynamics*, v. 2, Cepadues Editions, Toulouse, France, pp. 245-252, 1999.

[Fen05] N.-Q. Feng, and G.-F. Peng, "Applications of Natural Zeolite to Construction and Building Materials in China," *Construction and Building Materials*, v.19(8), pp. 579-84, October 2005.

[Fer72] J. H. Ferziger, and H. G. Kaper, *Mathematical Theory of Transport Processes in Gases*, North-Holland, Amsterdam, 1972.

[Gho99] H. Ghobarkar, O. Schaf, and U. Guth, "Zeolites - from Kitchen to Space," *Progress in Solid State Chemistry*, v. 27(2), pp. 29-73, 1999.

[Guo09] X. Guo, D. Singh, J. Murthy, and A.A. Alexeenko, "Numerical Simulation of Gas-Phonon Coupling in Thermal Transpiration Flows," *Physical Reviews E*, vol. 80, pp. (046310) 1-10, 2009.

[Gup06] N. K. Gupta, and Y. B. Gianchandani, "Modeling and Simulation of a Surface Micromachined Knudsen Pump," *ASME-IMECE*, pp. 1-7, 2006.

[Gup07] N. K. Gupta, and Y. B. Gianchandani, "Gas Flow in Nano-Channels: Thermal Transpiration Models with Application to a Si-Micromachined Knudsen Pump," *IEEE Transducers*, pp. 2329-2332, 2007.

[Gup08] N. K. Gupta, and Y. B. Gianchandani, "A Knudsen Pump Using Nanoporous Zeolite for Atmospheric Pressure Operation," *IEEE International Conference on Micro Electro Mechanical Systems (MEMS'08)*, Tuscon, USA, pp.38-41, 2008.

[Gup08] N.K. Gupta, and Y.B. Gianchandani, "Thermal Transpiration in Zeolites: A Mechanism for Motionless Gas Pumps," *Applied Physics Letters*, vol. 93, no. 19, p. 193511, 2008.

[Gup09] N.K. Gupta, and Y.B. Gianchandani, "A Planar Cascading Architecture for a Ceramic Knudsen Micropump,"*Proceedings of the 15th International Conference on Solid-State Sensors, Actuators and Microsystems (Transducers'09)*, pp. 2298-2301, 2009.

[Gup10] N.K. Gupta, and Y.B. Gianchandani, "A High-Flow Knudsen Pump Using a Polymer Membrane: Performance at and Below Atmospheric Pressures," *Proceedings of the 23rd IEEE International Conference on Micro Electro Mechanical Systems (MEMS'10)*, 2010.

[Han07] Y.-L. Han, and E. P. Muntz, "Experimental Investigation of Micro-Mesoscale Knudsen Compressor Performance at Low Pressures," *Journal of Vacuum Science & Technology B*, v. 25(3), pp. 703-714, May 2007.

[Has97] D. Hash, and H. Hassan, "Two Dimensional Coupling Issues of Hybrid DSMC/Navier Stokes-Solver," *American Institute of Aeronautics and Astronautics*, pp. 6333-6336, 1997.

[Hob00] J.P. Hobson, and D.B. Salzman, "Review of Pumping by Thermal Molecular Pressure," *Journal of Vacuum Science & Technology A: Vacuum, Surfaces, and Films*, v. 18, n. 4, part.1-2, pp. 1758-1765, 2000.

[Hob70] J.P. Hobson, "Accommodation Pumping – A New Principle for Low Pressures," *Journal of Vacuum Science and Technology*, v. 7, n. 2, pp. 351-357, 1970.

[Ive08] B.D. Iverson, S.V. Garimella, "Recent Advances in Microscale Pumping Technologies: A Review and Evaluation," *Microfluidics and Nanofluidics*, v. 5, n. 2, pp. 145-174, 2008.

[Jia04] W. Jia, and S. Murad, "Molecular Dynamics Simulations of Gas Separations using Faujasite – type Zeolite Membranes," *Journal of Chemical Physics*, v. 120(10), pp. 4877-85, March 2004.

[Jie00] D. Jie, X. Diao, K. B. Cheong, L. K. Yong, "Navier-Stokes Simulations for Gas Flow in Microdevices," *Journal of Micromechanics and Microengineering*, v. 10(3), pp. 372-379, 2000.

[Jud91] J.W. Judy, T. Tamagawa, and D.L. Polla, "Surface-Machined Micromechanical Membrane Pump," *Proceeding of the 4th IEEE International Conference on Micro Electro Mechanical Systems*, pp. 182-186, 1991.

[Kar05] G. E. Karniadakis, A. Beskok, and N. Aluru, *Microflows and Nanoflows: Fundamentals and Simulation*, Springer, New York, 2005.

[Ken38] E. Kennard, *Kinetic Theory of Gases*, McGraw Hill, pp. 327-332, 1938.

[Kes94] S. Kesraoui-Ouki, C. R. Cheeseman, and R. Perry, "Natural Zeolite Utilization in Pollution Control: A Review of Applications to Metals' Effluents," Journal of Chemical Technology and Biotechnology, v. 59(2), pp. 121-26, February 1994.

[Kim06] H. Kim, "An Integrated Electrostatic Peristalic Gas Micropump with Active Microvalves," *PhD. Thesis, University of Michigan*, 2006.

[Kim07] H. Kim, A. A. Astle, K.Najafi, L. P. Bernal, and P. D. Washabaugh, "A Fully Integrated High-Efficiency Peristaltic 18-Stage Gas Micropump with Active Microvalves," *IEEE International Conference on Micro Electro Mechanical Systems (MEMS'07), Japan*, pp. 127-30, 2007.

[Kim08] Y.-J. Kim, J. Chung, H.-K. Lee, E. Yoon, "Microfluidic Array Chip for Single-Cell Isolation Using Two-Way Pneumatic Actuation," *IEEE International Conference on Micro Electro Mechanical Systems (MEMS'08)*, Tuscon, USA, pp.14-17, 2008.

[Knu09] M. Knudsen, "Eine Revision der Gleichgewichtsbedingung der Gase. Thermische Molekularstromung," *Annalen der Physik,* Leipzig, vol. 336, no. 1, pp. 205-229, 1909. (in German)

[Kos08] S. Kosuge, and S. Takata, " Database for Flows of Binary Gas Mixtures Through a Plane Microchannel," *European Journal of Mechanics B/Fluids*, v. 27, pp. 444-465, 2008.

[Kow06] P. Kowalczyk, M. Sprynskyy, A. P. Terzyk, M. Lebedynets, J. Namiesnik, and B. Buszewski, "Porous Structure of Natural and Modified Clinoptilolites," *Journal of Colloidal Interface Science*, v. 297, pp. 77-85, 2006.

[Las04] D.J. Laser, and J.G. Santiago, "A Review of Micropumps," *Journal of Micromechanics and Microengineering*, v. 14(6), pp. R35-R64, 2004.

[Lea03] A.M. Leach, A.R. Wheeler, R.N. Zare, "Flow Injection Analysis in a Microfluidic Format," *Analytical Chemistry*, v. 75, n. 4, pp. 967-972, 2003.

[Li05] F. Li, Y. Jiang, L. Yu, T. Hou, and S. Sun, "Surface Effect of Natural Zeolite (Clinoptilolite) on the Photocatalytic Activity of TiO_2," *Applied Surface Science*, v. 252(5), p 1410-16, 2005.

[Lif81] E. M. Lifshitz and L. P. Pitaevskii, *Physical Kinetics*, Pergamon, Oxford, Ch. 1, 1981.

[Loe34] L. Loeb, *The Kinetic Theory of Gases*, McGraw Hill, 1934, pp. 355-359, 1934.

[Mar99] R. Marsili, "Lab-on-a-chip Poised to Revolutionize Sample Preparation," *R&D: Research and Development Kobe Steel Engineering Reports*, v 41(2), pp. 34-40, Feb 1999.

[Mas06] N. Masters, "Efficient Numerical Techniques for Multiscale Modeling of Thermally Driven Gas Flows with Application to Thermal Sensing Atomic Force Microscopy," *Ph.D. Thesis, Georgia Institute Technology*, June 2006.

[Mau03] J. Maurer, P. Tabeling, P. Joseph, H. Willaime, "Second-Order Slip Laws in Microchannels for Helium and Nitrogen," Physics of Fluids, v. 15(9), pp. 2613-2621, 2003.

[Max79] J. C. Maxwell, "On Stresses in Rarefied Gases Arising from Inequalities of Temperature," *Philosophical Transactions of Royal Society London,* v. 170, pp. 231-256, 1879.

[McN05] S. McNamara, and Y. B. Gianchandani, "On-Chip Vacuum Generated by a Micromachined Knudsen Pump," *Journal of Microelectromechanical Systems*, v. 14(4), pp. 741-746, 2005.

[Mor98] G. L. Morini, M. Spiga, "Slip Flow in Rectangular Microtubes," *Microscale Thermal Engineering*, v. 2(4), pp. 273-282, 1998.

[Mun02] E.P. Muntz, Y. Sone, K. Aoki, S. Vargo, and M. Young, "Performance Analysis and Optimization Considerations for a Knudsen Compressor in Transitional Flow," *Journal of Vacuum Science & Technology A*, vol. 20, no. 1, pp. 214-224, 2002.

[Mye05] M. Myers, H. Cave, S. Krumdieck, "Surface Tension Effects on Liquid Flow in Small Plastic Tubes When Gas Bubbles are Present," *Journal of Mechanical Engineering Science*, v. 219(8), pp. 853-857, 2005.

[Nag98] H.T. nagel, S.S. Schiffman, and R. Gutierrez-Osuna, "How and why of electronic noses," *IEEE Spectrum*, v. 35(9), pp. 22-34, Sep 1998.

[Ngu02] N.T. Nguyen , X. Huang, and T.K. Chuan, "MEMS-Micropumps: A review," *ASME J. Fluid Eng.*, 124(22), pp. 384-392, 2002.

[Ora98] E. Oran, C. Oh, and B. Cybyk, "Direct Simulation Monte Carlo: Recent Advances and Applications," Annu. Rev. Fluid Mech., 30, pp. 403-441, 1998.

[Oza06] S. Ozaydin, G. Kocar, and A. Hepbasli, "Natural Zeolites in Energy Applications," *Energy Source*, v.28(13-16), pp. 1425-31, 2006.

[Pan01] L. S. Pan, T. Y. Ng, D. Xu, and K. Y. Lam, "Molecular Block Model Direct Simulation Monte Carlo Method for Low Velocity Micro gas Flows," *Journal of Micromechanics and Microengineering*, v. 11(3), pp. 181-188, 2001.

[Pha95] G. Pham-Van-Diep, P. Keeley, E.P. Muntz, D.P. Weaver, "A micromechanical Knudsen Compressor," *Proceedings of the 19th International Symposium on Rarefied Gas Dynamics*, Oxford University Press, London, v. 1, 1995.

[Pie96] E. S. Piekos, and K. S. Breuer, "Numerical Modelling of Micromechanical Devices Uning the Direct Simulation Monte Carlo Method," *Journal of Fluid Engineering*, v. 118, pp. 464-469, 1996.

[Rey79] O. Reynolds, "On Certain Dimensional Properties of Matter in the Gaseous State," *Philosophical Transactions of Royal Society London,* v. 170, pp. 727-845, 1879.

[Ric98] M. Richter, R. Linnemann, and P. Woias, "Robust Design Gas and Liquid Micropump," *Sensors Actuators A*, v. 68, pp. 480-486, 1998.

[Rif00] J. L. Rife, M. I. Bell, J. S.Horwitz, M. N. Kabler, R. C. Y. Auyeung, and W. J. Kim, "Miniature Valveless Ultrasonic Pumps and Mixers," *Sensors and Actuators A (Physical)*, v. A86(1-2), pp. 135-40, Oct. 2000.

[Rov98] R. Roveda, D. Goldstein, and P. Varghese, "Hybrid Euler/Particle Approach for Continuum/Rarefied Flows," *Journal of Spacecraft and Rockets*, v. 35(3), pp. 258-265, 1998.

[Sak05] K. Sakaguchi, M. Matsui, and F. Mizukami, "Applications of Zeolite Inorganic Composites in Biotechnology: Current State and Perspectives," *Applied Microbiology and Biotechnology*, v. 67(3), pp. 306-11, May 2005.

[Sch02] C.G.J. Schabmueller, M. Koch, M.E. Mokhtari, A.G.R. Evans, A. Brunnschweiler, and H. Sehr, "Self-Aligning Gas/Liquid Micropump," *Journal of Micromechanics and Microengineering*, vol. 12, no. 4, pp. 420-424, 2002.

[Sch94] W.K. Schomburg, J. Vollmer, B. Bustgens, J. Fahrenberg, H. Hein, and W. Menz, "Microfluidic Components in LIGA Technique," *Journal of Micromechanics and Microengineering*, vol. 4, no. 4, pp. 186-191, 1994.

[Sha74] E. M. Shakov, *Method of Investigation of Rarefied Gas Flows*, Nauka, Moscow, 1974 (in Russian).

[Sha97] F. Sharipov, "Rarefied gas flow through a long tube at arbitrary pressure and temperature drop," *Journal of Vacuum Science and Technology A*, 15(4), pp. 2434-2436, 1997.

[Sha98] F. Sharipov, and V. Seleznev, "Data on Internal Rarefied Gas Flows," *Journal of Physical and Chemical Reference Data*, v. 27(3), pp. 657-706, 1998.

[Sha99] F. Sharipov, "Non-isothermal gas flow through rectangular microchannels," *Journal of Micromechanics and Microengineering*, v.9, pp. 394-401, 1999.

[Sia03] S.K. Sia, and G.M. Whitesides, "Microfluidic Devices Fabricated in Poly(dimethylsiloxane) for biological studies," *Electrophoresis*, vol. 24, no. 21, pp. 3563-3576, 2003.

[Smi90] J.G. Smits, "Piezoelectric Micropump With Three Valves Working Peristaltically," *Sensors and Sctuatore, A Physical*, v. 21, n. 1-3, pp. 203-206, 1990.

[Smi99] P. G. Smirniotis, L. Davydov, and E. Ruckenstein, "Composite Zeolite-Based Catalysts and Sorbents," Catalysis Reviews – Science and Engineering, v. 41(1), pp. 43-113, February 1999.

[Son00] Y. Sone "Flow Induced by Temperature Fields in Rarefied Gas and their Ghost Effect on the Behavior of a Gas in Continuum Limit," *Annual Review of Fluid Mechanics*, v. 32, pp. 779-811, 2000.

[Sre69] A. K. Sreekanth, "Slip Flows Through Long Circular Tubes," *L. Trilling, H. Y. Wachman (eds)., Proceedings of the 6th International Symposium on rarefied Gas Dynamics*, Academic Press, New York, pp. 667-680, 1969.

[Ste93] E. Stemme and G Stemme, "A Valveless Diffuser/Nozzle-Based Fluid Pump," *Sensors and Actuators A*, vol. 39, pp. 159-167, 1993.

[Ter79] S. Terry, J.H. Jerman, and J.B. Angell, "A Gas Chromatographic Air Analyzer Fabricated on a Silicon Wafer," *IEEE Transactions on Electron Devices*, v. 26, pp. 1880-86, 1979.

[thinXXS08]
http://www.thinxxs.com/fileadmin/website/pdf/MicroPump_mdp1304_v2.1.pdf

[Tra74] D.H. Tracey, "Thermomolecular Pumping Effect," *Journal of Physics E: Scientific Instruments*, v. 7, n. 7, pp. 533-536, 1974.

[Tsa07] N.-C. Tsai, and C.-Y. Sue, "Review of MEMS Based Drug Delivery and Dosing Systems," *Sensors and Actuators A: Physical*, vol. 134, no. 2, pp.555-564, 2007.

[Ung00] M.A. Unger, H.P. Chou, T. Thorsen, A. Scherer, and S.R. Quake, "Monolithic Microfabricated Valves and Pumps by Multilayer Soft Lithography," *Science*, v. 288, n. 5463, pp. 113–116, 2000.

[Var01] S.E. Vargo, and E.P. Muntz, "Initial Results from the First MEMS Fabricated Thermal Transpiration-Driven Vacuum Pump," *AIP Conference Proceedings*, no. 585, pp. 502-509, 2001.

[Var96] S. E. Vargo, and E. P. Muntz, "A Simple Micromechanical Compressor and Vacuum Pump for Flow Control and other Distributed Applications," 34th Aerospace Sciences Meeting and Exhibit, Reno, NV, January 1996.

[Wan05] C.H. Wang, and G.-B. Lee, "Automatic Bio-Sampling Chips Integrated With Micro-Pumps and Micro-Valves for Disease Detection," *Biosensors and Bioelectronics*, v. 21, n. 3, pp. 419-425, 2005.

[Wan06] C.-H. Wang, and G.-B. Lee, "Pneumatic Driven Peristaltic Micropumps Utilizing Serpentine-Shape Channels," v. 16, n. 2, pp. 341-348, 2006.

[Wei00] J. Weitkamp, "Zeolites and Catalysis," *Solid State Ionics, Diffusion and Reaction*, v. 131(1-2), pp. 175-88, June 2000.

[Wij00] W. van der Wijngaart, H. Andersson, P. Enoksson, K. Noren, and G. Stemme, "The Self-Priming and Bi-Directional Valveless Diffuser Micropump for both Liquid and Gas," *Proceedings of the 13th IEEE International Conference on Microelectro Mechanical Systems*, pp. 674-679, 2000.

[Wil70] J. Williams III, "Thermal Transpiration – A Continuum Gasdynamics View," *Journal of Vacuum Science and Technology*, v.8, pp. 446-450, 1970.

[Wis04] K.D. Wise, K. Najafi, R.D. Sacks, and E.T. Zellers, "A Wireless Integrated Microsystem for Environmental Monitoring," *IEEE International Solid State Circuits*

Conference, v. 1, pp. 434-537, 2004.

[Wu08] M.-H. Wu, S.-B. Huang, Z. Cui, Z. Cui, and G.-B. Lee, "Development of Perfusion –Based Micro 3-D Cell Culture Platform and its Application for High Throughput Drug Testing," *Sensors and Actuators B: Chemical*, v. 129, n.1, pp. 231-240, 2008.

[Xue00] H. Xue, and Q. Fan, "A New Analysis Solution of the Navier-Stokes Equations for Microchannel Flow," *Microscale Thermal Engineering*, v. 4(2), pp. 125-143, 2000.

[Yan06] X. Yang, Z. Zhou, X. Ye, M. Xiao, "Simulation and Experimental Studies on a Piezoelectrically Actuated Microdiaphragm Air Pump, *Journal of Micro/Nanolithography, MEMS, and MOEMS*, v. 5, n. 2, pp. 021106, 2006.

[You01] M. Young, G. Shiflett, E. P. Muntz, S. Vargo, and A. Green, "The Knudsen Compressor as an Energy Efficient Micro-Scale Vacuum Pump," *American Society of Mechanical Engineers, Micro-Electromechanical Systems Division Publication (MEMS)*, v. 3, pp. 433-441, 2001.

[You03] M. Young, Y. L. Han, E. P. Muntz, G. Shiflett, A. Ketsdever, A. Green, " Thermal Transpiration in Microsphere Membranes," 23rd *International Symposium on Rarefied Gas Dynamics,* v. 663,pp. 743-751, 2003.

[You05] M. Young, Y.L. Han, E.P. Muntz, and G. Shiflett, "Characterization and Optimization of a Radiantly Driven Multi-Stage Knudsen Compressor," *AIP Conference Proceedings*, no. 762, pp. 174-179, 2005.

[Zel04] E.T. Zellers, W.H. Steinecker, G.R. Lambertus, M. Agah, C.-J. Lu, H.K.L. Chan, J.A. Potkay, M.C. Oborny, J.M. Nichols, A. Astle, H.S. Kim, M.P. Rowe, J. Kim, L.W. da Silva, J. Zheng, J.J. Whiting, R.D. Sacks, S.W. Pang, M. Kaviany, P.L. Bergstrom, A.J. Matzger, Ç. Kurdak, L.P. Bernal, K. Najafi, and K.D. Wise, "A Versatile MEMS Gas Chromatograph for Determination of Environmental Vapor Mixture," ***Invited Paper and Talk***, *Technical Digest, Solid State Sensor, Actuator and Microsystems Workshop (Hilton Head 2004)*, pp. 61-66, 2004.